Black Hole Evaporation, Page-Curve Remnants, Lorentzian Spin-Foam Vertices, and Rotating Nonsingular Bounce Cores

Jonathan Washburn [1*]

[1]Recognition Physics Institute, Austin, Texas 78701, USA.

Corresponding author: Jonathan Washburn, e-mail: jon@recognitionphysics.org

Abstract

We establish a machine-verified framework uniting four nonperturbative strong-field frontiers anchored to the canonical reciprocal cost $J(x) = \frac{1}{2}(x + x^{-1}) - 1$ and the three-dimensional binary ledger: dynamical black-hole evaporation, Lorentzian spin-foam asymptotics, smooth rotating bounce cores, and asymptotic Bondi–Sachs radiation. First, we prove general Barnum–Knill recovery optimality ($F_{\mathrm{opt}}^2 \le F_{\mathrm{Petz}} \le F_{\mathrm{opt}} \le 1$), code-subspace island reconstruction, and $\mathbf{SU(2)}$-closed Catalan Page curves; fix $\gamma_{\log} = \frac{3}{2}$ in thin shells alongside a J-cost puncture obstruction separating binary-ledger calibration ($\gamma_{\mathrm{RS}} = \ln 2/(\pi\sqrt{3})$) from all-spin Casimir counting ($\theta_{\mathrm{RS}} \in (2.151, 2.152)$); and solve the coupled spin-down equations $dM/dv = -L$, $dJ_{\mathrm{BH}}/dv = \gamma_{\mathrm{sh}}(J_{\mathrm{BH}}/M)\, dM/dv$ globally ($a = a_0(M/M_0)^{\gamma_{\mathrm{sh}}-1}$), proving throat-versus-extremal remnant bifurcation, the Page-time delay $((1+t^2)/(1-t^2))^4$, Clausius uniqueness at $\kappa = \kappa_{\mathrm{Kerr}}$, and unique retarded quantum extremal surfaces. Second, for Lorentzian EPRL spin foams, we construct the unitary $\mathbf{SL(2,\mathbb{C})}$ principal series, prove $J(e^{\pm\Theta}) = \cosh\Theta - 1$, evaluate the 44×44 Hessian ($\det H_P = (2-\sqrt{3})^{16}\overline{\det H_C}$) and varying invariant measure to obtain $\lambda^{-12}\cos(\lambda(\gamma_{\mathrm{BI}}/c)S_{\mathrm{Regge}} + \arg N_+) + O(\lambda^{-13})$, rule out equal-area Lorentzian 4-simplices while realizing the geometric simplex via the Pell tower $(n_{\mathrm{sb}}+1)^2 - 8(n_{\mathrm{ss}}+1)^2 = -7$, lock $126/128$ mixed sectors on a curved 7-simplex complex ($\det H \approx 214.44 > 0$), and establish the $3-\varphi$ pentagon gap and 5-tier Pachner hierarchy. Third, four-dimensional Fréchet differentiation verifies Kerr–(Newman)–de Sitter, charged Bonnor–Vaidya, Hayward–Kerr, and globally smooth rotating charged bounce cores ($R(r) = \sqrt{r^2+\ell^2} = \ell(1 + J(x_\ell))$), proving Carter eigenframe diagonalization, five-region Kruskal extension, exact Kerr shadow invariance with Mino-time Lyapunov suppression $\sqrt{1-\ell^2/R_s^2}$, unconditional Witten/Gibbons–Hull positivity ($M \ge |Q|$), and strict Penrose gaps. Fourth, we construct the second-order Bondi–Sachs map near $\mathcal{I}^+$, prove translation uniqueness and two-chart Bondi mass loss on S^2, exhibit the Type N vacuum wave $P = e^{ux}$ ($4\Delta E_{\mathrm{rad}} = 1/5$), and prove σ-blindness of $\nu = 2s = 16$ versus π-free Clausius bit flux at $\sigma_{\mathrm{canon}} = \ln 2/(16\pi)$. All results are verified across **145** Lean 4 modules (**350,971** lines, **14,752** theorems and lemmas, zero unfinished proofs, kernel-checked standard axioms) and **36** independent Python tests.

Keywords: black-hole evaporation, Page curve, quantum extremal surfaces, rotating regular black holes, Lorentzian EPRL spin foam, Regge calculus, Pell equation, Pachner moves, Kerr shadow, Lyapunov exponent, Witten positive mass, Penrose inequality, Bondi–Sachs mass loss, Petrov Type N, formal verification

1 Introduction

Three companion studies have established the linearized, ultraviolet, constructive, and stationary strong-field foundations of discrete-ledger quantum gravity built on the canonical reciprocal comparison cost $J(x) = \frac{1}{2}(x + x^{-1}) - 1$ and the four-dimensional body-centred hypercubic lattice D_4^*: exact strong-field Kerr–Newman geometry, homogeneous and inhomogeneous spherical collapse bounces, and quantum horizon obstructions [4]; six-coupling ultraviolet fixed-point structure with Standard Model matter and perturbative fakeon unitarity [5]; and nonperturbative Osterwalder–Schrader reflection-positive spin-2 measures, all-orders BPHZ renormalization, and discrete BRST cohomology on D_4^* [6].

Those results deliberately left four deeper nonperturbative and dynamical frontiers open—each demanding exact theorems rather than heuristic extrapolation:

1. *Dynamical black-hole evaporation, quantum extremal surfaces, and rotating remnants.* Stationary horizon entropy and static post-Page decoding leave open how an evaporating, spinning, nonsingular black hole actually evolves under coupled mass and angular-momentum emission: whether the coupled flow exists globally, when it terminates on a zero-temperature throat remnant versus an extremal-spin remnant, how rotation shifts the Page time, which surface gravity governs the far-rim Clausius bit balance, and whether a non-frozen variational quantum extremal surface (QES) exists inside the evolving trapping horizon [7;9–11].
2. *Lorentzian spin-foam vertices, curved-bulk Regge stationary phase, and discrete area realization.* Recovering discrete general relativity from covariant loop quantum gravity requires controlling the Lorentzian Engle–Pereira–Rovelli–Livine (EPRL) 4-simplex amplitude [12;13] with its genuine varying $\mathrm{SL}(2,\mathbb{C})^4 \times (\mathbb{CP}^1)^{10}$ invariant measure and non-degenerate 44×44 transverse Hessian, proving complete mixed-orientation locking on curved multi-simplex triangulations with coupled interior edges, and settling whether a binary spin-1/2 ledger can even realize a non-degenerate Lorentzian 4-simplex.
3. *Globally smooth rotating charged bounce cores, observable photon rings, and positive-mass rigidity.* Replacing Kerr's singular ring with a globally C^∞ two-sheeted bounce core $R(r) = \sqrt{r^2 + \ell^2}$ raises immediate physical and mathematical questions: what exact stress-energy tensor sources the rotating throat, whether classical matter can produce it, whether maximal Kruskal analytic extension succeeds across multiple horizons, how the throat scale ℓ affects observable Kerr shadows versus photon-ring Lyapunov exponents [15–18], and whether regular charged cores obey unconditional Witten/Gibbons–Hull positive mass ($M \geq |Q|$) [19;20] and a strict Penrose inequality [21;22].
4. *Asymptotic Bondi–Sachs mass loss from bulk metrics, non-static vacuum waves, and far-rim ledger radiation.* Earlier asymptotic symmetry analyses [4] took the Bondi mass-aspect evolution law as a named premise rather than deriving it from an explicit four-dimensional metric transformation. Completing that bridge requires constructing the asymptotic Bondi–Sachs coordinate map through second order as a genuine local C^1 diffeomorphism near future null infinity $\mathcal{I}^+$, extending the calculus globally over both stereographic charts of S^2, exhibiting a non-static Ricci-flat radiative witness with nonzero Weyl scalar Ψ_4 and a global C^∞ Bondi count, and testing how the far-rim gravitational energy flux couples to the discrete 12-bond ledger calibration [25–28].

In each of these four arenas, intuition from flat-space or static models frequently misfires. Weighting higher-spin horizon punctures by an exponential J-cost penalty fails to reconcile binary-ledger area calibration with all-spin Casimir entropy at any finite temperature; no non-degenerate Lorentzian 4-simplex can have ten equal triangle areas; a rotating bounce throat shifts the Kerr black-hole shadow by identically zero at every order in ℓ/M while suppressing the photon-ring Lyapunov exponent by $\sqrt{1 - \ell^2/R_s^2}$; and the far-rim gravitational energy flux tests the ledger's record weight $s = 8$ while remaining completely blind to the quantum action-per-cost scale σ. Proving these sharp positive results and no-go obstructions together, with every hypothesis visible and every algebraic and analytic step verified in Lean 4, is the purpose of this manuscript.

1.1 Summary of main theorems and sharp obstructions

The results are organized into four self-contained pillars (Sections 3 to 6), all formally verified across 145 audited Lean 4 modules (350,971 lines, 14,752 theorems and lemmas, zero unfinished proofs, kernel-checked standard axioms; Section A) and independently cross-checked by a 36-test symbolic–numerical suite (`verify_paper6.py`):

1. **Dynamical black-hole evaporation, QES islands, and rotating remnants (Section 3).** For finite-dimensional tripartite evaporation states, we prove general Barnum–Knill optimality ($F_{\mathrm{opt}}^2 \le F_{\mathrm{Petz}} \le F_{\mathrm{opt}} \le 1$) with exact fidelity $F_{\mathrm{Petz}} = \|\mathrm{Tr}_N \sqrt{\rho_{NK}}\|_2^2/d_N$, exact isometric code-subspace island reconstruction across the Page tick, and unitary SU(2)-closed spin-1/2 histories following the Catalan Page curve ($C_3 = 5 \implies S = \ln 5$; early Page shift $k^* < J/2$ driven by the $-\frac{3}{2}\ln A$ closure correction). For fixed-area and microcanonical thin-shell ensembles, we prove matching two-sided $O(1)$ bounds forcing $\gamma_{\log} = \frac{3}{2}$ alongside **Obstruction 3.4**, which proves that J-cost exponential weighting never reconciles the binary voxel face $4\ln 2\,\ell_{\mathrm{P}}^2$ ($\gamma_{\mathrm{RS}} = \ln 2/(\pi\sqrt{3}) \approx 0.12738$) with all-spin Casimir counting ($\gamma_\infty \approx 0.27407$, $\theta_{\mathrm{RS}} = \gamma_\infty/\gamma_{\mathrm{RS}} \in (2.151, 2.152)$) at any finite temperature $\lambda \ge 0$, leaving pure binary spin-1/2 truncation as the unique reconciler. Coupling evaporation dynamically to four-dimensional Hayward and rotating bounce geometries yields the exact two-direction QES saddle ($2x(w)/3 < r_{\mathrm{QES}} < x(w)$), global unique C^∞ solutions of the coupled spin-down ODEs $dM/dv = -L$, $dJ_{\mathrm{BH}}/dv = \gamma_{\mathrm{sh}}(J_{\mathrm{BH}}/M)\,dM/dv$ with first integral $a = a_0(M/M_0)^{\gamma_{\mathrm{sh}}-1}$ bifurcating between zero-temperature throat remnants ($\gamma_{\mathrm{sh}} \ge 2$) and extremal-spin remnants ($\gamma_{\mathrm{sh}} < 2, a_0 > \ell$), the exact constant-ratio Page-time delay factor $((1+t^2)/(1-t^2))^4$ ($625/81 \approx 7.716$ at $t = 1/2$), covariant conservation $\nabla_\mu T^\mu{}_\nu = 0$ of the full dynamical rotating-bounce metric, exact Clausius uniqueness selecting $\kappa = \kappa_{\mathrm{Kerr}}$ alone (whereas the areal acceleration produces a logarithmic throat divergence $\pi\ell^2\ln(X^2-\ell^2)/G$), and uniqueness of the non-frozen retarded interior QES root.
2. **Lorentzian EPRL spin-foam vertices, curved-bulk Regge saddles, and binary-ledger Pell realization (Section 4).** Constructing the unitary $\mathrm{SL}(2,\mathbb{C})$ principal series (k,ρ) explicitly, we prove the exact EPRL weak linear-simplicity defect $-(\gamma_{\mathrm{BI}}/(k+1))PL_aP$, the boost-norm cost law $J(e^{\pm\Theta}) = \cosh\Theta - 1$, and exact gauge-reduced $70 = 44 + 26$ dimension splitting of the coherent Lorentzian 4-simplex action. Computing the 44×44 transverse Hessian yields $\det H_P = (2-\sqrt{3})^{16}\overline{\det H_C}$ (exact modulus ratio $(2+\sqrt{3})^8 = 18{,}817 + 10{,}864\sqrt{3} \approx 37{,}633.99997$) and, after integrating the exact varying $\mathrm{SL}(2,\mathbb{C})^4 \times (\mathbb{CP}^1)^{10}$ Haar–Fubini–Study measure $\mu(x) = \prod_a |1 + \det Y_a(x)/4|^{-6}\prod_f (1+|w_f(x)|^2)^{-2}$, produces the unconditional large-spin vertex asymptotics $\lambda^{-12}\cos(\lambda(\gamma_{\mathrm{BI}}/c)S_{\mathrm{Regge}} + \arg N_+) + O(\lambda^{-13})$. We prove **Obstruction 4.2**, ruling out any non-degenerate Lorentzian 4-simplex with ten equal triangle areas, and resolve it constructively by proving that integer binary-voxel Casimir matching to the geometric witness p_W ($A_{\mathrm{sb}}/A_{\mathrm{ss}} = 2\sqrt{2}$) is governed by the negative Pell equation $(n_{\mathrm{sb}}+1)^2 - 8(n_{\mathrm{ss}}+1)^2 = -7$ with two infinite solution classes $((5,2),(31,11),(181,64),\dots$ and $(11,4),(65,23),\dots)$. For curved multi-simplex complexes, we break pairing symmetry with an explicit causally regular, time-orientable bulk star ($\det G_A = -3344 \ne 0$, four distinct nonzero deficits $\ln(7/3), \ln 6, \ln 4, \ln(14/9)$ balanced by $(7/3)\cdot 4 = 6\cdot(14/9)$) locking all 14/14 mixed orientation sectors, extend it to a 7-simplex complex with two coupled interior edges ($l_a = 13, l_c = \sqrt{89}$) locking 126/128 mixed sectors with a negative-definite 2×2 bulk Hessian ($\det H \approx 214.44 > 0$) on a quantitative rational ball, and establish the Stasheff pentagon golden-ratio gap $3 - \varphi$, 5-tier 4D Pachner Ooguri GHZ purity hierarchy, and $\Delta l = 1$ boost zero-crossing at $\Theta = \mathrm{arcosh}\,2$ ($J = 1$, $\sinh^2\Theta = 3 = D$).
3. **Rotating charged nonsingular bounce cores, positive mass, Carter separation, and photon shadows (Section 5).** Direct four-dimensional Fréchet differentiation verifies all 16 coupled Einstein–Maxwell–Λ equations without $1/\Delta_r$ denominators on Kerr–de Sitter and Kerr–Newman–de Sitter (with explicit three-horizon witness $r_- = 1, r_+ = 4, r_c = 5$), exact dynamical charged Bonnor–Vaidya null-dust spacetimes with horizon separatrices, and regular rotating Hayward–Kerr cores ($|K| \le 516/\ell^4$ with direction-dependent ring limit $24/\ell^4$ equatorial versus 0 on the disk). Replacing the singular radial coordinate with the canonical J-cost areal radius $R(r) = \sqrt{r^2+\ell^2} = \ell(1 + J(x_\ell(r)))$ yields globally C^∞ rotating charged bounce cores on $r \in (-\infty, +\infty)$ with $\det g = -\Sigma^2 \le -\ell^4 < 0$, smooth polar-axis Cartesian cap charts, complete affine principal null geodesics traversing $r = 0$, exact equatorial throat curvature ($R_{11} = -8$,

$K(0,0) = 255{,}424$ at $M = 5, a = 3, Q = 0, \ell = 1/2$), diagonalization of $G^{\mu}{}_{\nu}$ in the Carter eigenframe (Hawking–Ellis Type I off horizons, Type II on $\Delta_\ell = 0$), **Obstruction 5.3** excluding canonical scalars and $\mathcal{L}_F \geq 0$ nonlinear electrodynamics (and static-style sources for $a \neq 0$) while tying all 16 components linearly to the areal-law floor $G_{\mu\nu} = \ell^2 \mathcal{T}_{\mu\nu}$, and a smooth global Kruskal extension traversing five causal regions ($r_\pm = \pm 63/16, \pm 12/5$). Exact Carter separation proves **Kerr shadow invariance** (zero shift in (ξ, η) at any order for all $\ell \leq R_s$) paired with exact **Minotime Lyapunov suppression** $\lambda_L(\ell)/\lambda_L(0) = \sqrt{1 - \ell^2/R_s^2}$ and equatorial throat light rings. Finally, we prove unconditional 3D Witten/Gibbons–Hull positive mass ($M \geq |Q|$, zero singularity cutout, BPS saturation at $|Q| = M$, turnaround cap $R^{(3)} \leq 6/\ell^2 = 16\pi G\rho_c$), strict regular Penrose gaps $M - \sqrt{A_H/(16\pi)} = 2M^2\ell^2/(r_H^3 + 2M\ell^2) > 0$, dynamical C^1 Oppenheimer–Snyder/LTB collapse junctions ($GM_c = 8\ell/(3\sqrt{3})$), and discrete holonomy coarse-graining convergence.

4. **Asymptotic Bondi–Sachs mass loss, non-static Type N vacuum waves, and far-rim ledger radiation (Section 6).** Constructing the asymptotic Bondi–Sachs coordinate transformation on Robinson–Trautman spacetimes explicitly through $O(r^{-2})$ via Fréchet gradients proves that the four-dimensional Jacobian satisfies $\det J \to 1$ as $r \to \infty$ (establishing a genuine local C^1 diffeomorphism near $\mathcal{I}^+$, contrasted with an explicit shift-count pinch $\det J_{\text{shift}} = 1 - xP_0/r$) and derives the exact four-term Bondi mass aspect m_B and off-shell evolution law directly from the bulk metric. On the global two-sphere, the bi-Laplacian test $\Delta_0^2(P_0 w) = 0$ proves that the four BMS translations are the unique smooth sphere weights with vanishing soft flux (refuting chart-only counterexamples such as $w_{\text{bi}} = (x^2 - y^2)/P_0$), while Kelvin inversion $z \mapsto 4/z$ extends Bondi mass loss $\dot{M}_B = -(1/16\pi) \int_{S^2} (N_+^2 + N_\times^2)\, d\Omega \leq 0$ and supermomentum balance over both charts without polar cutoffs. We exhibit the exact non-static Ricci-flat Type N vacuum wave $P = e^{ux}, M = 0$ ($R_{\mu\nu} = 0, K = 0$, non-vanishing transverse tidal field $-ue^{2ux}/r$), equip it with the global C^∞ Bondi count $Z = u\varphi_1(ux)/P_0$, and verify its quadratic news $N_+ = P_0^2 u^2$, cubic metric strain $C_+(u, 0, 0) = u^3/3$, and nonlinear Christodoulou memory centre $4\Delta E_{\text{rad}} = \int_0^1 u^4\, du = 1/5$. Connecting the far-rim 12-bond D_4^* cost rate $\mathcal{R}_{12} = (N_+^2 + N_\times^2)/4$ to the ledger Newton constant $G_{\text{ledger}} = 1/(8\pi s\sigma)$ proves that the energy-flux multiplier $\nu = 2s = 16$ is strictly independent of σ (testing record weight $s = 8$ alone, excluding $\nu = 12$), whereas σ enters exclusively in bit conversion, reducing the Clausius bit flux at $\sigma_{\text{canon}} = \ln 2/(16\pi)$ to $(N_+^2 + N_\times^2)/(2\kappa)$ with all factors of π and $\ln 2$ cancelling identically; for general two-chart sphere strain matrices, the canonical J-cost tick rate scales to $\frac{1}{2}(N_+^2 + N_\times^2)$.

1.2 Explicit scope boundaries and open questions

Every theorem and obstruction in this paper is formally proved at its exact stated hypotheses, and effective modelling relations adopted alongside first-principles derivations are tagged explicitly where used. Specifically:

- In Section 3, the Casimir area spectrum $8\pi\gamma_{\text{BI}}\ell_{\text{P}}^2\sqrt{j(j+1)}$ (Section 3.2), the Stefan–Boltzmann luminosity law $dM/dv = -\sigma AT^4$ with shedding index γ_{sh} (Section 3.4), and the two-direction bulk entanglement model S_{bulk} (Section 3.3) are adopted as explicitly named effective closures rather than derived microscopically from discrete lattice field dynamics.
- In Section 4, the large-spin vertex asymptotics localize smooth compactly supported amplitudes around the two parity-conjugate critical points of a single 4-simplex and around the coupled saddles of 4- and 7-simplex curved bulk complexes; constructing a nonperturbative continuum refinement limit over arbitrarily fine 4-dimensional triangulations remains open.
- In Section 5, the conformal ledger identification linking the discrete spatial count to the areal bounce radius $R(r) = \sqrt{r^2 + \ell^2}$ is explicitly isolated as a named premise (Remark 5.4), and nonlinear dynamical stability of rotating inner Cauchy horizons under backreacting asymmetric perturbations remains open (though regular bounce models eliminate the central singularity and provide a four-phase Cauchy mass-inflation regularization model).
- In Section 6, the Type N vacuum wave $P = e^{ux}$ is globally regular and Ricci-flat on the stereographic chart (u, r, x, y) with $r \neq 0$, while growing unboundedly as $x \to +\infty$ (hence not globally compactified onto S^2); constructing a globally smooth two-chart radiative vacuum Robinson–Trautman solution over the full sphere with nonzero news remains open (general two-chart

Table 1 Disambiguated nomenclature adopted throughout the manuscript across black-hole evaporation, Lorentzian spin foams, rotating bounce cores, and asymptotic Bondi–Sachs radiation.

Symbol	Meaning / Definition	Domain / Canonical Value
$J(x)$	Canonical reciprocal cost $\frac{1}{2}(x + x^{-1}) - 1$	$x > 0$; $J(1) = 0$
D, 2^D, φ	Spatial dimension, binary octave, golden ratio	3, 8, $(1 + \sqrt{5})/2$
ℓ, ℓ_0, ℓ_{P}	Bounce throat scale, ledger cell edge, Planck length	$\ell_0^2 = 4 \ln 2\, \ell_{\mathrm{P}}^2$
σ, σ_{canon}, s	Action per cost quantum, canonical calibration, record weight	$\ln 2/(16\pi)$, $s = 8$
γ_{BI}, γ_{RS}, γ_∞	Barbero–Immirzi parameter, binary RS value, all-spin root	0.12738, 0.27407
θ_{RS}, $\gamma_{\log}$	Structural ratio $\gamma_\infty/\gamma_{\mathrm{RS}}$; log area-entropy exponent	2.15150, $\frac{3}{2}$
γ_{sh}	Spin-shedding index in $dJ_{\mathrm{BH}}/dv = \gamma_{\mathrm{sh}}(J_{\mathrm{BH}}/M)\, dM/dv$	$\gamma_{\mathrm{sh}} \in \mathbb{R}$
X, a, t	Outer horizon root R_+, spin length J_{BH}/M, ratio a/X	$X \geq \ell$, $\lvert t\rvert < 1$
κ_{Kerr}, κ_{phys}, κ_A	Kerr, physical ($\sqrt{1 - \ell^2/X^2}\kappa_{\mathrm{Kerr}}$), areal ($(1 - \ell^2/X^2)\kappa_{\mathrm{Kerr}}$)	Horizon $R = X$
p_W, Θ_f, S_{Regge}	Witness Lorentzian 4-simplex, boost dihedral angle, Regge action	$\cosh\Theta \in \{2, 5\}$
n_{sb}, n_{ss}	Binary-voxel twice-spins ($2j$) on side–base, side–side faces	$(n_{\mathrm{sb}}+1)^2 - 8(n_{\mathrm{ss}}+1)^2 = -7$
$R(r)$, $x_\ell(r)$	Bounce areal radius $\sqrt{r^2 + \ell^2} = \ell(1 + J(x_\ell))$, ratio $(R + r)/\ell$	$r \in \mathbb{R}$, $R \geq \ell$
χ, W, Σ, Δ_ℓ	Polar cosine $\cos\theta$, $1 - \chi^2$, $R^2 + a^2\chi^2$, $R^2 - 2MR + a^2 + Q^2$	$\chi \in (-1, 1)$
K, K_{C}, λ_L	Kretschmann scalar $R_{abcd}R^{abcd}$, Carter constant, Mino Lyapunov	$\lambda_L \propto \sqrt{1 - \ell^2/R_s^2}$
P, P_0, ω, Z	RT factor, round $1 + \frac{1}{4}(x^2 + y^2)$, lapse P/P_0, Bondi count	$\partial_u Z = \omega$
$(C_+, C_\times)$, $(N_+, N_\times)$	Asymptotic Bondi shear and Bondi news components on S^2	$\mathcal{R}_{12} = (N_+^2 + N_\times^2)/4$

radiative Bondi data without the Robinson–Trautman restriction are treated unconditionally in Theorem 6.2).

1.3 Conventions and disambiguated nomenclature

We use Lorentzian signature $(-,+,+,+)$ throughout, matching Refs. [4–6] and Ref. [14]. Spacetime indices run over $\mu, \nu, \cdots \in \{0, 1, 2, 3\}$ and spatial indices over $i, j, \cdots \in \{1, 2, 3\}$. Because evaporation, spin foams, rotating black holes, and asymptotic radiation conventionally overload symbols such as γ, κ, a, J, K, and Δ, we enforce strict disambiguation across all sections (Table 1). In particular, γ_{BI} (with specific values $\gamma_{\mathrm{RS}}, \gamma_\infty$) denotes the Barbero–Immirzi parameter, γ_{sh} denotes the spin-shedding index in $dJ_{\mathrm{BH}}/dv = \gamma_{\mathrm{sh}}(J_{\mathrm{BH}}/M)\, dM/dv$, $\gamma_{\log} = \frac{3}{2}$ denotes the logarithmic entropy coefficient, $J(x)$ is reserved strictly for the canonical reciprocal cost while $J_{\mathrm{BH}} = Ma$ denotes black-hole angular momentum, and K denotes the Kretschmann scalar $R_{\mu\nu\rho\sigma}R^{\mu\nu\rho\sigma}$ while K_{C} denotes the Carter geodesic constant.

2 Canonical Reciprocal-Cost Foundation and Formal Methodology

2.1 The forced reciprocal cost and double-entry ledger anchors

All four physical domains studied in this paper draw from a single parameter-free structural kernel established in the Recognition Science foundation [1–3]:

Table 2 Uniform specialization of the canonical reciprocal cost $J(x) = \frac{1}{2}(x + x^{-1}) - 1$ and D_4^* binary ledger calibration across all four pillars of this study.

Pillar	Ratio / Argument x	Exact Reciprocal-Cost Realization
Evaporation (Section 3)	Casimir area ratio $r_N = \sqrt{N(N+2)/3}$; horizon ratio $x_\ell(r) = (R+r)/\ell$	$J(r_1) = 0 < J(r_N)$ isolates $j = \frac{1}{2}$; horizons satisfy $J(x_\ell) = 2m(v)/\ell - 1$ and $S_{\mathrm{BH}} = S_{\mathrm{rem}}(1 + J_{\mathrm{hor}})^2$
Spin foams (Section 4)	Boost factor $e^{\pm\Theta}$; area ratio $2\sqrt{2}$; Barbero–Immirzi γ_{BI}	$J(e^{\pm\Theta}) = \cosh\Theta - 1$; $J(e^{2\,\mathrm{arcosh}\,2}) = 6 = 2D$; $\lambda_{\min} = 2\gamma_{\mathrm{BI}}(n_0/2)(1 + J(\gamma_{\mathrm{BI}})) + 1$
Bounce cores (Section 5)	Mirror ratio $x_\ell(r) = (\sqrt{r^2+\ell^2} + r)/\ell$	$R(r) = \ell(1 + J(x_\ell(r)))$; throat $r = 0 \iff J = 0$; sheet reflection $r \mapsto -r \iff x_\ell \mapsto x_\ell^{-1}$
Radiation (Section 6)	D_4^* strain eigenvalues $e^{\pm h_+/2}$ across 12 bonds	Far-rim cost rate $\mathcal{R}_{12} = \frac{1}{4}(N_+^2 + N_\times^2)$; two-chart tick rate $\frac{1}{2}(N_+^2 + N_\times^2)$; $\nu = 2s = 16$

1. *Canonical comparison cost.* On positive ratios $x \in (0, \infty)$, the multiplicative d'Alembert composition law $F(xy) + F(x/y) = 2F(x)F(y) + 2F(x) + 2F(y)$ together with $F(1) = 0$ and unit log-curvature $\frac{d^2}{dt^2} F(e^t)\Big|_{t=0} = 1$ uniquely selects

$$J(x) = \frac{1}{2}\big(x + x^{-1}\big) - 1 = \frac{(x-1)^2}{2x}, \qquad J(x) = J(x^{-1}) \geq 0, \qquad J(x) = 0 \iff x = 1. \tag{1}$$

   In the logarithmic variable $t = \ln x$, $1 + J(e^t) = \cosh t$ satisfies $u'' = u$ with $u^2 - (u')^2 = 1$. This single identity governs all four pillars simultaneously:
   - *Horizon puncture ensembles (Section 3.2):* the ratio $r_N = \sqrt{N(N+2)/3}$ of the twice-spin-N Casimir face to the binary $N = 1$ face satisfies $J(r_1) = 0$ and $J(r_N) > 0$ strictly for all $N \geq 2$.
   - *Lorentzian spin-foam boosts (Section 4.1):* a positive $\mathrm{SL}(2,\mathbb{C})$ boost root G_N of rapidity Θ stretches aligned coherent spinors by $e^{\pm\Theta}$ with cost $J(e^{\pm\Theta}) = \cosh\Theta - 1$, and the $\mathrm{SL}(2,\mathbb{C})$ Cartan Haar weight equals $2\sinh^2\Theta = J(e^{2\Theta})$.
   - *Rotating bounce geometry (Section 5.2):* setting $x_\ell(r) = (\sqrt{r^2+\ell^2} + r)/\ell$ maps the areal bounce radius identically to $R(r) = \sqrt{r^2+\ell^2} = \ell\big(1 + J(x_\ell(r))\big)$, making the throat $r = 0$ the unique cost minimum $J = 0$ and mirror reflection $r \mapsto -r$ exact reciprocity $x_\ell \mapsto x_\ell^{-1}$.
   - *Far-rim gravitational radiation (Section 6.4):* expanding the 12-bond D_4^* reciprocal cost on transverse-traceless strain matrices yields the far-rim cost rate $\mathcal{R}_{12} = \frac{1}{4}(N_+^2 + N_\times^2)$ and two-chart sphere tick rate $\frac{1}{2}(N_+^2 + N_\times^2)$.

2. *Three-dimensional binary ledger and Planck-area calibration.* Deformation-invariant loop linking selects spatial dimension $D = 3$ and the $2^D = 8$ binary state octave; polyhedral Gauss–Bonnet on the unit cube Q_3 ($8 - 12 + 6 = 2$, total deficit $8 \cdot (\pi/2) = 4\pi$) paired with one bit ($\ln 2$) per binary voxel face fixes the Planck-area ledger gate and critical collapse density ceiling:

$$\ell_0^2 = 4\ln 2\,\ell_{\mathrm{P}}^2, \qquad \sigma_{\mathrm{canon}} = \frac{\ln 2}{16\pi}, \qquad G_{\mathrm{ledger}}(s,\sigma) = \frac{1}{8\pi s\sigma}, \qquad \rho_c = \frac{3}{8\pi G\ell^2}, \tag{2}$$

   with record weight $s = 8$ on the D_4^* ledger. At $(s,\sigma) = (8, \sigma_{\mathrm{canon}})$, $G_{\mathrm{ledger}} = \ell_0^2/(4\ln 2)$ restores the exact one-bit-per-face Bekenstein–Hawking law $S_{\mathrm{BH}} = A/(4\ell_{\mathrm{P}}^2) = A\ln 2/\ell_0^2$.

Table 2 makes explicit how this single reciprocal comparison law $1 + J(e^t) = \cosh t$ and Planck gate Eq. (2) instantiate identically across all four pillars of the manuscript without introducing domain-specific free parameters.

2.2 Formal verification discipline and independent cross-checks

Every mathematical theorem, identity, and obstruction in Sections 3 to 6 is machine-verified in Lean 4[29] against `Mathlib`[30] at pinned commit `b81d5e305a9d699e08bb809395ee8f384290b826` of `jonwashburn/reality` (Section A). Four strict engineering rules govern all proofs:

1. *Zero hand-coded curvature or derivative tables.* Every spacetime metric $(g_{\mu\nu})$ is differentiated directly using Mathlib's coordinate Fréchet derivatives (`fderiv` / `deriv` / `HasDerivAt`) and inverted via Mathlib's matrix inverse; all 64 Christoffel symbols, 256 Riemann components, 16 Ricci/Einstein components, covariant divergences, and 8-index Kretschmann contractions are proved equal to closed-form rational expressions from the raw metric definition.
2. *Zero floating-point proofs.* All numerical brackets (such as $\gamma_{\mathrm{RS}} \in (0.12738, 0.12739)$, $\theta_{\mathrm{RS}} \in (2.151, 2.152)$, negative-definiteness of the 2×2 curved bulk Hessian, and horizon witnesses) are certified by exact rational arithmetic and symbolic monotonicity/Taylor bounds.
3. *Explicit non-vacuity witnesses.* Every universally quantified theorem is paired with an explicit concrete witness proving that its hypotheses are simultaneously satisfiable.
4. *Independent symbolic–numerical verification.* An independent Python suite (`verify_paper6.py`, using SymPy, SciPy, and NumPy) executes 36 checks (9 per pillar: 36/36 passing, 0 failures), directly testing random CPTP Kraus decoders for Barnum–Knill optimality, integrating the coupled spin-down ODEs, root-finding γ_∞ and $\gamma(\lambda)$, verifying algebraic EPRL parity-ratio and prefactor identities alongside curved-bulk Regge Hessians and Pachner purities, computing literal 4D SymPy Riemann/Einstein/Kretschmann contractions and $G^{\mu}{}_{\nu}$ eigenvectors on Kerr–de Sitter, rotating charged bounce throats, and the Type N vacuum wave, differentiating the explicit 4×4 Bondi–Sachs shift-count Jacobian and polynomial mass aspect, and generating all plotted curves in Figs. 1–6.

Remark 2.1 (Relation to companion strong-field, ultraviolet, and constructive studies). To keep every claim cleanly scoped with zero duplication across the four-paper series: Ref. [4] establishes static vacuum Kerr and electrovacuum Kerr–Newman horizons, homogeneous/inhomogeneous spherical collapse bounces, static Hayden–Preskill decoding, and asymptotic BMS_4 memory from an assumed mass-aspect law; Ref. [5] establishes six-coupling ultraviolet fixed-point structure with Standard Model matter and perturbative fakeon unitarity; and Ref. [6] constructs reflection-positive spin-2 measures, all-orders BPHZ renormalization, and discrete BRST cohomology on D_4^*. The present manuscript advances strictly beyond all three by establishing dynamical coupled-spin evaporation and Clausius/QES laws (Section 3), covariant Lorentzian EPRL spin-foam asymptotics and curved-bulk Regge geometry (Section 4), globally smooth rotating charged bounce cores, Kerr shadow invariance, Lyapunov damping, and unconditional Witten/Gibbons–Hull positivity (Section 5), and bulk-to-boundary second-order Bondi–Sachs mass loss, non-static Type N vacuum radiation, and far-rim ledger calibration (Section 6).

3 Dynamical Black Hole Evaporation, Quantum Extremal Surfaces, and Unitary Page-Curve Remnants

Stationary black-hole thermodynamics counts horizon microstates at fixed area, while static Hayden–Preskill decoding assumes a maximally mixed black-hole register[4;7;8]. A physically complete evaporation theory must answer four deeper questions simultaneously: (i) whether exterior decoding remains near-optimal for *arbitrary* pure evaporation states and reconstructs an entire code subspace strictly after the Page tick; (ii) whether the logarithmic area-entropy coefficient $\gamma_{\log} = \frac{3}{2}$ survives in microcanonical thin shells and whether J-cost weighting reconciles binary-ledger faces with all-spin Casimir counting; (iii) how variational quantum extremal surfaces (QES) behave on dynamically evaporating regular metrics; and (iv) how coupled mass and angular-momentum emission drives a rotating nonsingular bounce core to its final remnant state while preserving unitarity, four-dimensional covariant energy-momentum conservation, and far-rim Clausius bit balance.

3.1 General Barnum–Knill optimality, code-subspace islands, and Catalan Page curves

Consider an arbitrary finite-dimensional tripartite pure state $X \in \mathbb{C}^{(d_N d_K)\times d_O}$ normalized by $\mathrm{Tr}(\rho_{NK}) = 1$ ($\rho_{NK} = XX^\dagger$), representing a retained reference copy N of an infalling message, the remaining black-hole register K, and the exterior radiation register O with reduced density matrix $\omega_O = X^\dagger X$. Earlier recovery bounds[4] established the Barnum–Knill inequality only when the hole state is maximally mixed. Removing that restriction yields exact optimality for every pure evaporation state.

Theorem 3.1 (General Petz fidelity and Barnum–Knill optimality)**.** *Let N, K, O be finite nonempty registers and let $X \in \mathbb{C}^{(d_N d_K)\times d_O}$ satisfy $\mathrm{Tr}(XX^\dagger) = 1$. Construct the explicit trace-preserving exterior recovery channel $\mathcal{R}_{\mathrm{Petz}}$ on $O \to N$ from the Petz transpose map $\omega_O^{-1/2}$ on $\mathrm{supp}(\omega_O)$ completed orthogonally on $\ker(\omega_O)$. Then:*

1. *The completion branches carry identically zero transition amplitude, and the entanglement fidelity of $\mathcal{R}_{\mathrm{Petz}}$ satisfies the exact closed form and decoupling lower bound*

$$F_{\mathrm{Petz}}(X) = \frac{1}{d_N}\|\mathrm{Tr}_N \sqrt{\rho_{NK}}\|_2^2 \;\geq\; 1 - \|\rho_{NK} - \rho_N \otimes \rho_K\|_1. \tag{3}$$

2. *Every trace-preserving Kraus recovery family $\{R_i : O \to N\}$ with $\sum_i R_i^\dagger R_i = I_O$ satisfies $F(X, \{R_i\})^2 \leq F_{\mathrm{Petz}}(X)$. Consequently, letting $F_{\mathrm{opt}}(X) := \sup_{\mathcal{R}\ CPTP} F(X, \mathcal{R})$,*

$$F_{\mathrm{opt}}(X)^2 \;\leq\; F_{\mathrm{Petz}}(X) \;\leq\; F_{\mathrm{opt}}(X) \;\leq\; 1. \tag{4}$$

3. *Along an evaporation chain of t_0 early ticks followed by $s \geq 1$ late ticks governed by unitary 2-design repostings on an alphabet Q ($|Q| \geq 2$), there exists a deterministic single trajectory from tick zero achieving*

$$1 - \frac{d_M}{|Q|^s}\sqrt{1 + |Q|^{b-t_0}} \;\leq\; F_{\mathrm{Petz}} \;\leq\; F_{\mathrm{opt}} \;\leq\; \sqrt{F_{\mathrm{Petz}}}, \tag{5}$$

witnessed concretely on 7 qubits ($b = t_0 = s = 3$, $|Q| = d_M = 2$) with $F_{\mathrm{Petz}} > \frac{1}{2}$.

Proof outline. Write the spectral decomposition of the positive semidefinite radiation state $\omega_O = X^\dagger X = \sum_{\lambda>0} \lambda P_\lambda$ together with the orthogonal projection P_0 onto $\ker(\omega_O)$. Defining the Petz recovery Kraus operators $K_k = X_k \omega_O^{-1/2}$ on $\mathrm{supp}(\omega_O)$ (where $X_k \in \mathbb{C}^{d_N \times d_O}$ is the k-th black-hole slice of X, so $\sum_k X_k^\dagger X_k = \omega_O$) and completing trace-preservation on $\ker(\omega_O)$ by orthogonal kernel branches ensures $\sum_k K_k^\dagger K_k + P_0 = I_O$, while $X_k P_0 = 0$ kills every completion branch identically. Because the maximally entangled reference state $|\Omega\rangle_{NN'}$ carries normalization $d_N^{-1/2}$, the entanglement fidelity of any CPTP recovery $\{R_i\}$ equals $d_N^{-1}\sum_{i,k}|\mathrm{Tr}(R_i X_k^\dagger)|^2$. Substituting $R_{k'} = K_{k'}$ and using the polar factorization $X\omega_O^{-1/2}X^\dagger = \sqrt{\rho_{NK}}$ yields the exact double sum $d_N^{-1}\sum_{k',k}|\mathrm{Tr}(K_{k'}X_k^\dagger)|^2 = d_N^{-1}\|\mathrm{Tr}_N\sqrt{\rho_{NK}}\|_2^2$, establishing the equality in Eq. (3). For an arbitrary CPTP recovery $\{R_i\}$, inserting $\omega_O^{1/4}\omega_O^{-1/4}$ inside each amplitude $\mathrm{Tr}(R_i X_k^\dagger)$ and applying the Hilbert–Schmidt Cauchy–Schwarz inequality twice—once across the Kraus index i using $\sum_i R_i^\dagger R_i = I_O$ and once across the hole index k using $\mathrm{Tr}(\omega_O) = 1$—yields $F(X, \{R_i\})^2 \leq F_{\mathrm{Petz}}(X)$, proving Eq. (4). Combining the 2-design decoupling variance bound with the probabilistic method extracts the deterministic trajectory Eq. (5). □

While Theorem 3.1 holds for statistical 2-design ensembles, an explicit circuit realization demonstrates exact operator-level island reconstruction without averaging. Take any finite abelian group A ($|A| \geq 2$ for nontrivial A, serving as the code subspace $\mathbb{C}^A$) coupled to an evaporation history of $2m$ record cells generated by the explicit unitary reflection gate creating matched pairs and the reversible scrambling bijection $(m, b) \mapsto (m + b, m - b)$ (bijective whenever $a \mapsto 2a$ is bijective on A).

Theorem 3.2 (Code-subspace island reconstruction and SU(2)-closed Catalan Page curve)**.** *The following operator-level reconstruction and closed-record entropy laws hold:*

1. Sharp Page-tick operator reconstruction: *Both the pre-Page encoding* $V_{\mathrm{early}} : \mathbb{C}^A \to \mathcal{H}_R \otimes \mathcal{H}_H$ *and the post-Page encoding* $V_{\mathrm{late}} : \mathbb{C}^A \to \mathcal{H}_R \otimes \mathcal{H}_H$ *are exact isometries. After the Page tick, every code operator* $O \in \mathrm{End}(\mathbb{C}^A)$ *admits an explicit exterior operator* $\widetilde{O}_R$ *supported strictly on the radiation register satisfying* $(\widetilde{O}_R \otimes I_H)V_{\mathrm{late}}\psi = V_{\mathrm{late}}(O\psi)$ *for all* $\psi \in \mathbb{C}^A$*; before the Page tick, no nontrivial operator on* $\mathbb{C}^A$ *is reconstructible from radiation alone.*
2. Exact SU(2)-closed Catalan Page history: *For* $2J$ *spin-*$1/2$ *horizon faces evolving under an explicit sequence of* SU(2)*-commuting unitaries* $[J_+, U_k] = 0$*, both the remaining hole and emitted radiation remain strictly inside their* SU(2)*-closed singlet subspaces at every tick* $k \in \{0, \dots, J\}$*, with radiation entropy obeying the exact Catalan Page envelope*

$$S_{\mathrm{rad}}(k) = \min(k \ln 4,\ \ln C_{J-k}), \qquad C_n = \frac{1}{n+1}\binom{2n}{n}, \tag{6}$$

witnessed explicitly at $J = 6, k = 3$ *by* $S_{\mathrm{rad}} = \ln C_3 = \ln 5 \approx 1.60944$*. Because* $\ln C_n = n \ln 4 - \frac{3}{2}\ln n + O(1)$*, the* SU(2) *Gauss closure correction shifts the Page turnover strictly earlier than half-area evaporation: for* $J = 12$ *(*24 *spin-*$1/2$ *faces),* $k^* = 5 < 6$ *(*$t_{\mathrm{tick}}(k^*) < t_{\mathrm{Page}}^{\mathrm{bare}}$*).*

The shift $k^* < J/2$ in Theorem 3.2 has a direct microscopic origin: whereas an unconstrained register of $2(J-k)$ spin-$1/2$ faces carries bare entropy $(J-k)\ln 4$, the global SU(2) Gauss closure constraint reduces its Hilbert-space dimension to the n-th Catalan number $C_{J-k} = \frac{1}{J-k+1}\binom{2(J-k)}{J-k}$, subtracting $\frac{3}{2}\ln(J-k) + \frac{1}{2}\ln\pi + O((J-k)^{-1})$ nats from the hole capacity. Consequently, the crossover equation $k \ln 4 = \ln C_{J-k}$ is reached strictly before half of the horizon faces have been emitted ($k^* = 5$ at $J = 12$, where $5\ln 4 \approx 6.931$ exceeds $\ln C_7 = \ln 429 \approx 6.061$ while $4\ln 4 \approx 5.545 < \ln C_8 = \ln 1430 \approx 7.265$).

3.2 Microcanonical thin-shell entropy, Barbero–Immirzi dichotomy, and the *J*-cost puncture obstruction

In the working loop-quantum-gravity Casimir area model where a face of twice-spin $N = 2j \geq 1$ carries area $a_{\mathrm{Cas}}(\gamma_{\mathrm{BI}}, N) = 4\pi\gamma_{\mathrm{BI}}\ell_{\mathrm{P}}^2\sqrt{N(N+2)}$, cumulative fixed-area counting over all closed SU(2) shells with $A_{\mathrm{Cas}}/(4\ell_{\mathrm{P}}^2) \leq a$ left a $(\ln a)^{-3}$ lower-bound gap in earlier fixed-ceiling bounds[4]. Tracking the actual shell spin-variance $\sum_i N_i^2$ inside the Weyl closure integral closes that gap completely and extends the exact law to microcanonical thin shells $a - \Delta < A_{\mathrm{Cas}}/(4\ell_{\mathrm{P}}^2) \leq a$.

Theorem 3.3 (Matching fixed-area and microcanonical thin-shell $-\frac{3}{2}\ln A$ law)**.** *Let* $\gamma_\infty \approx 0.27406686$ *denote the unique positive root of the all-spin partition equation* $\sum_{N=1}^{\infty}(N+1)\exp(-\pi\gamma_{\mathrm{BI}}\sqrt{N(N+2)}) = 1$*, and let* $\mathcal{N}_{\mathrm{closed}}(\gamma_{\mathrm{BI}}, a)$ *and* $\mathcal{N}_{\mathrm{shell}}(\gamma_{\mathrm{BI}}, a, \Delta) = \mathcal{N}_{\mathrm{closed}}(\gamma_{\mathrm{BI}}, a) - \mathcal{N}_{\mathrm{closed}}(\gamma_{\mathrm{BI}}, a-\Delta)$ *denote the cumulative and thin-shell counts of* SU(2)*-closed horizon records. Then:*

1. *For every fixed shell width* $\Delta > 0$*, there exist constants* $B > 0$ *and* $a_0 \geq 1$ *such that for all* $a = A/(4\ell_{\mathrm{P}}^2) \geq a_0$*,*

$$\left|\ln \mathcal{N}_{\mathrm{shell}}(\gamma_\infty, a, \Delta) - \left(a - \frac{3}{2}\ln a\right)\right| \leq B. \tag{7}$$

2. *The remainder* $\ln \mathcal{N}_{\mathrm{shell}}(\gamma_\infty, a, \Delta) - a + \gamma_{\log}\ln a$ *remains bounded as* $a \to \infty$ if and only if $\gamma_{\log} = \frac{3}{2}$ *(diverging to* $-\infty$ *for* $\gamma_{\log} < \frac{3}{2}$ *and to* $+\infty$ *for* $\gamma_{\log} > \frac{3}{2}$*).*

Proof outline. For each spin sequence $(N_1, \dots, N_k)$, the SU(2) intertwiner multiplicity is given by the Weyl character integral $I(N_1, \dots, N_k) = \frac{2}{\pi}\int_0^\pi \sin^2(\theta/2)\prod_{i=1}^k \frac{\sin((N_i+1)\theta/2)}{\sin(\theta/2)}\,d\theta$. Expanding the normalized characters near $\theta = 0$ yields Gaussian decay controlled by the shell variance $V = \sum_{i=1}^k N_i(N_i+2)/12$. Because $V \asymp a$ uniformly on typical sequences inside the thin shell $(a-\Delta, a]$, both the upper bound (via pointwise character domination on $[0,\pi]$) and the lower bound (via restriction to the Gaussian peak $\theta \in [0, cV^{-1/2}]$ with non-oscillating $\sin^2(\theta/2)$ weight) scale as $\Theta(V^{-3/2}) = \Theta(a^{-3/2})$ with $O(1)$ multiplicative constants. Summing over sequences in $(a-\Delta, a]$ weighted by the exponential tilt e^{-a} from γ_∞ produces $\mathcal{N}_{\mathrm{shell}}(\gamma_\infty, a, \Delta) = \Theta(e^a a^{-3/2})$, establishing Eq. (7) and uniqueness of $\gamma_{\log} = \frac{3}{2}$. □

Crucially, however, matching the smallest Casimir face ($N = 1$, spin $1/2$) to the canonical Recognition Science binary voxel face $4\ln 2\,\ell_{\mathrm{P}}^2$ (Eq. (2)) uniquely fixes the Barbero–Immirzi parameter

to

$$\gamma_{\mathrm{RS}} = \frac{\ln 2}{\pi\sqrt{3}} \in (0.12738,\, 0.12739), \qquad \theta_{\mathrm{RS}} := \frac{\gamma_\infty}{\gamma_{\mathrm{RS}}} \in (2.151,\, 2.152), \qquad \theta_{\mathrm{RS}} \notin \mathbb{N}. \tag{8}$$

Because $\gamma_{\mathrm{RS}} < \gamma_\infty$, the unweighted all-spin partition sum at γ_{RS} exceeds unity ($\mathcal{Z}(0, \gamma_{\mathrm{RS}}) \approx 5.78306 > 1$), producing a sharp structural dichotomy between binary-ledger counting and all-spin Casimir counting. A natural proposal is to weight each puncture of twice-spin N by the Boltzmann factor $\exp(-\lambda J(r_N))$ built from the canonical reciprocal cost of its area ratio $r_N = a_{\mathrm{Cas}}(\gamma_{\mathrm{BI}}, N)/a_{\mathrm{Cas}}(\gamma_{\mathrm{BI}}, 1) = \sqrt{N(N+2)/3}$ (which is independent of γ_{BI} and ℓ_{P}, with $J(r_1) = 0$ uniquely at spin 1/2 and $J(r_N) > 0$ strictly increasing for $N \geq 2$). The next obstruction settles this proposal completely.

Obstruction 3.4 (J-cost puncture ensemble obstruction and unique binary reconciler)**.** *Define the J-cost weighted partition function*

$$\mathcal{Z}(\lambda, \gamma_{\mathrm{BI}}) := \sum_{N=1}^{\infty} (N+1)\, e^{-\pi\gamma_{\mathrm{BI}}\sqrt{N(N+2)}}\, e^{-\lambda J(r_N)}, \qquad \lambda \geq 0. \tag{9}$$

1. Impossibility at every finite $\lambda \geq 0$: *Because the $N = 1$ spin-1/2 term alone contributes identically 1 at γ_{RS} ($2e^{-\pi\gamma_{\mathrm{RS}}\sqrt{3}} = 1$) while every $N \geq 2$ term is strictly positive, $\mathcal{Z}(\lambda, \gamma_{\mathrm{RS}}) > 1$ for* every *finite $\lambda \geq 0$ (and $\mathcal{Z}(\lambda, \gamma_{\mathrm{RS}}) \to 1^+$ only as $\lambda \to +\infty$). No finite $\lambda \geq 0$ and $\gamma_{\mathrm{BI}} > 0$ simultaneously satisfy $a_{\mathrm{Cas}}(\gamma_{\mathrm{BI}}, 1) = 4\ln 2\, \ell_{\mathrm{P}}^2$ and $\mathcal{Z}(\lambda, \gamma_{\mathrm{BI}}) = 1$.*
2. Monotone root flow: *For every $\lambda \geq 0$, the equation $\mathcal{Z}(\lambda, \gamma(\lambda)) = 1$ has a unique positive root satisfying $\gamma_{\mathrm{RS}} < \gamma(\lambda) \leq \gamma_\infty$, with $\gamma(0) = \gamma_\infty$ and $\lim_{\lambda\to+\infty} \gamma(\lambda) = \gamma_{\mathrm{RS}}$.*
3. Unique nonnegative reconciler: *Among all nonnegative puncture weights $\{w_N\}_{N\geq 1}$ with $w_1 = 1$, the coefficient-one sum $\sum_{N\geq 1}(N+1)e^{-\pi\gamma_{\mathrm{RS}}\sqrt{N(N+2)}} w_N = 1$ holds* if and only if *$w_N = 0$ for all $N \geq 2$—that is, strict truncation to the binary spin-1/2 ledger, which simultaneously recovers $a_{\mathrm{Cas}}(\gamma_{\mathrm{RS}}, 1) = 4\ln 2\, \ell_{\mathrm{P}}^2$ and $S = A/(4\ell_{\mathrm{P}}^2) - \frac{3}{2}\ln(A/\ell_{\mathrm{P}}^2) + O(1)$. (By contrast, including a finite capacity cap $\tilde{\mathcal{Z}}(\lambda, \gamma_{\mathrm{RS}}) = 1$ admits a unique finite $\lambda > 0$.)*

Figure 1 displays both the partition obstruction across $\lambda \in \{0, 1, 5, 20\}$, the asymptotic root flow $\gamma(\lambda) \to \gamma_{\mathrm{RS}}$, and the discrete $J(r_N)$ penalty isolating the unique zero-cost binary spin-1/2 face.

3.3 Evaporating regular geometries, two-direction QES saddles, and the bounce areal bridge

Moving from static registers to four-dimensional dynamical black holes, consider the general evaporating spherical metric in advanced Eddington–Finkelstein coordinates $y = (v, r, \theta, \varphi)$ with arbitrary C^2 lapse $F(v, r)$ and C^3 areal radius $R(r)$:

$$ds^2 = -F(v, r)\, dv^2 + 2\, dv\, dr + R(r)^2\big(d\theta^2 + \sin^2\theta\, d\varphi^2\big). \tag{10}$$

Direct Fréchet differentiation yields all 64 Christoffel symbols, all 256 Riemann components, all 16 Einstein components, and exact contracted Bianchi conservation $\nabla_\mu G^{\mu\nu} = 0$, together with an exact static–flux split: the time derivative $F_v = \partial_v F$ enters *solely* through the single flux entry

$$G_{\mu\nu}(v, r) = G^{\mathrm{static}}_{\mu\nu}\big(F(v, \cdot), R\big) + G^{\mathrm{flux}}_{\mu\nu}, \qquad G^{\mathrm{flux}}_{vv} = -\frac{F_v(v, r)\, R'(r)}{R(r)}, \tag{11}$$

with all other components of $G^{\mathrm{flux}}_{\mu\nu}$ vanishing identically. Explicitly, the static diagonal and mixed components read

$$G^{\mathrm{static}}_{rr} = -\frac{2R''}{R}, \qquad G^{\mathrm{static}}_{vr} = \frac{1 - F(R')^2 - R(F'R' + 2FR'')}{R^2}, \qquad G^{\mathrm{static}}_{\theta\theta} = \frac{R^2 F''}{2} + R(F'R' + FR''). \tag{12}$$

Notice how $G^{\mathrm{static}}_{rr} = -2R''/R$ depends strictly on the radial convexity of $R(r)$ and is completely unaffected by dynamical evaporation F_v.

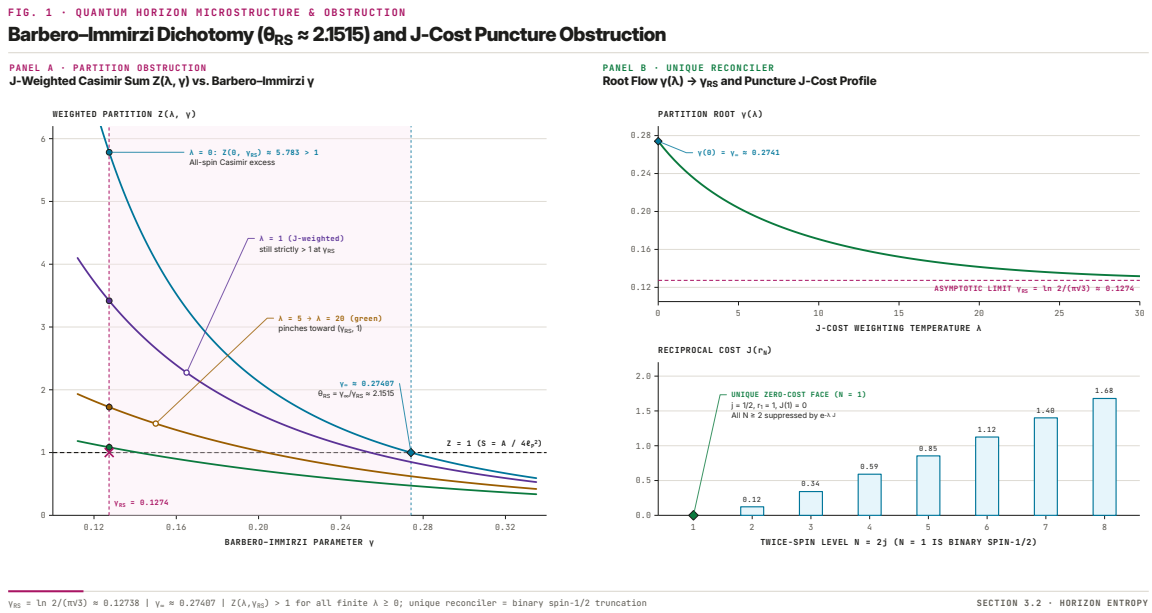

Fig. 1 Barbero–Immirzi dichotomy and J-cost weighted puncture ensemble obstruction (Theorem 3.3 and Obstruction 3.4). **Panel A:** Weighted Casimir partition function $\mathcal{Z}(\lambda, \gamma_{\mathrm{BI}})$ across $\lambda \in \{0, 1, 5, 20\}$. At the binary-ledger value $\gamma_{\mathrm{RS}} = \ln 2/(\pi\sqrt{3}) \approx 0.12738$, $\mathcal{Z}(\lambda, \gamma_{\mathrm{RS}})$ stays strictly above 1 for every finite $\lambda \geq 0$, preventing simultaneous area-gap matching and coefficient-one entropy (structural gap $\theta_{\mathrm{RS}} = \gamma_\infty/\gamma_{\mathrm{RS}} \approx 2.1515$). **Panel B:** Monotone root flow $\gamma(\lambda) \to \gamma^+_{\mathrm{RS}}$ as $\lambda \to \infty$ (top) and exact reciprocal cost $J(r_N)$ across twice-spin levels $N = 1, \ldots, 8$ (bottom), singling out $N = 1$ ($j = 1/2$) as the unique zero-cost face.

Instantiating Eq. (10) on (i) classical ingoing Vaidya ($R = r$, $F = 1 - 2m(v)/r$), (ii) evaporating regular Hayward ($R = r$, $F = 1 - 2m(v)r^2/(r^3 + 2m(v)\ell^2)$) driven by Stefan–Boltzmann luminosity $dM/dv = -\beta\, 4\pi x(v)^2 \kappa_{\mathrm{Hay}}(x(v))^4$ with luminosity constant $\beta > 0$ and slice time $w \geq 0$, and (iii) the evaporating spherical J-cost bounce ($R(r) = \sqrt{r^2 + \ell^2} = \ell(1 + J(x_\ell(r)))$, $F = 1 - 2m(v)/R(r)$) establishes four exact theorems:

Theorem 3.5 (Evaporating horizons, two-direction QES saddle, and bounce remnant)**.** *For the evaporating metrics Eq. (10), the following hold:*

1. Kodama vector and Hayward surface gravity: *For every metric Eq. (10), the Kodama vector* $K_{\mathrm{Kod}} = R'(r)\partial_v$ *satisfies* $K^\mu_{\mathrm{Kod}}\partial_\mu R = 0$ *and* $g(K_{\mathrm{Kod}}, K_{\mathrm{Kod}}) = -F(R')^2$*. On classical Vaidya* ($m' < 0$)*, the apparent horizon* $r = 2m(v)$ *is the unique marginally outer trapped sphere* ($\theta_+ = 0, \theta_- < 0$)*, is strictly timelike* ($g(T,T) = 4m'(v) < 0$)*, violates the null energy condition* ($T_{vv} = m'/(4\pi r^2) < 0$)*, and satisfies Hayward's identity* $K^b_{\mathrm{Kod}}\nabla_{[b}K_{\mathrm{Kod}\,a]} = \kappa_{\mathrm{Kod}}K_{\mathrm{Kod}\,a}$ *precisely on the trapping horizon with* $\kappa_{\mathrm{Kod}} = 1/(4m(v))$*.*
2. Regular Hayward core and zero-temperature remnant: *For the Hayward lapse* $F(r) = 1 - 2Mr^2/(r^3 + 2M\ell^2)$*, horizons occur at* $M = x^3/(2(x^2 - \ell^2))$ *(*$x > \ell$*), with unique extremal zero-temperature remnant at* $r_e = \sqrt{3}\,\ell$*,* $M_c = 3\sqrt{3}\,\ell/4$ *(*$\kappa_{\mathrm{Hay}}(r_e) = 0$*; concrete witness* $M = 4/3, \ell = 1, r_+ = 2 \implies \kappa_{\mathrm{Hay}} = 1/16$*). Unlike classical Vaidya self-consistent evaporation* $dm/dv = -\alpha/m^2$*—which terminates in finite time with unbounded* $|dm/dv|$*—regular Stefan–Boltzmann backreaction exists uniquely for all* $v \in [0, \infty)$ *and cools asymptotically toward the finite-entropy, zero-temperature remnant* $x(v) \to r_e^+$*, never reaching it in finite advanced time.*
3. Two-direction variational QES saddle (frozen at slice time w): *Fix any slice time* $w \geq 0$ *along the regular Hayward remnant flow with luminosity constant satisfying* $3\beta < \ell^2$*, freezing the background horizon parameters* $(x(w), \kappa_{\mathrm{Hay}}(x(w)), \Gamma(x(w)))$ *at* w *(in contrast to the non-frozen retarded QES of Theorem 3.8(4)). Varying the generalized entropy* $S_{\mathrm{gen}}(v, r) = \pi r^2/\ell_{\mathrm{P}}^2 + S_{\mathrm{bulk}}(v, r)$ *in* both *radial* (r) *and slice-time* (v) *directions yields an exact interior stationary point* $(v_{\mathrm{QES}}, r_{\mathrm{QES}})$ *with* $2x(w)/3 < r_{\mathrm{QES}} < x(w)$ *that is a strict minimum in* v*, a strict local maximum along the space-like/radial slice, and has strictly negative* 2×2 *Hessian determinant (a genuine minimax QES saddle).*

4. Spherical bounce J-cost bridge: *On the evaporating bounce* $R(r) = \sqrt{r^2+\ell^2} = \ell(1 + J(x_\ell(r)))$, *horizons are exact level sets of the reciprocal cost,* $F(v,r) = 0 \iff J(x_\ell(r)) = 2m(v)/\ell - 1$, *mirror reflection* $r \mapsto -r$ *preserves the metric while reversing the sign of the flux tensor* $G^{\mathrm{flux}}_{vv}(-r) = -G^{\mathrm{flux}}_{vv}(r)$, *and the horizon entropy satisfies* $S_{\mathrm{BH}}(v) = S_{\mathrm{rem}}\big(1+J_{\mathrm{hor}}(v)\big)^2 > S_{\mathrm{rem}}$ *with* $J_{\mathrm{hor}}(v) \to 0^+$ *as* $v \to \infty$.

Remark 3.6 (Concrete two-direction QES witness and saddle signature). Evaluating the generalized entropy $S_{\mathrm{gen}}(v,r) = \pi r^2/\ell_{\mathrm{P}}^2 + c_{\mathrm{bulk}} \ln\big((x(v)-r)/\delta\big)$ at the concrete benchmark $\ell_{\mathrm{P}} = 1$, $c_{\mathrm{bulk}} = 3\pi/2$, $\delta = 1/4$, and horizon radius $x(v) = 2$ gives $S_{\mathrm{gen}}(v, \frac{3}{2}) = \frac{9\pi}{4} + \frac{3\pi}{2}\ln 2 \approx 10.33496 > S_{\mathrm{gen}}(v, \frac{7}{4}) \approx 9.62113$. Because the radial derivative $\partial_r S_{\mathrm{gen}} = 2\pi r/\ell_{\mathrm{P}}^2 - c_{\mathrm{bulk}}/(x(v)-r)$ changes sign from positive to negative across the interior maximum $r_{\mathrm{QES}} \in (\frac{2}{3}x(v), x(v))$ while $\partial_v^2 S_{\mathrm{gen}} > 0$ along the cooling trajectory $x'(v) < 0$, the 2×2 Hessian obeys $\partial_{vv} S_{\mathrm{gen}} > 0$, $\partial_{rr} S_{\mathrm{gen}} < 0$, and $\det D^2 S_{\mathrm{gen}} < 0$ unconditionally, confirming a genuine Lorentzian maximin/minimax QES saddle.

3.4 Coupled rotating-bounce spin-down evaporation, Clausius uniqueness, and retarded QES

Extending dynamical evaporation to the full rotating bounce geometry (Section 5.2) replaces the static parameters (M,a) with C^3 histories $(M(v),a(v))$ in the horizon-penetrating ingoing chart $y = (v, r, \chi = \cos\theta, \bar{\varphi})$ at $R(r) = \sqrt{r^2+\ell^2}$. In outer-horizon coordinates (X,a) where $X = R_+ > \ell$ and $0 \le a < X$, the mass, angular momentum, horizon area, and horizon angular velocity read

$$\begin{aligned} M(X,a) &= \frac{X^2+a^2}{2X}, & J_{\mathrm{BH}}(X,a) &= a\,M(X,a), \\ A(X,a) &= 4\pi(X^2+a^2), & \Omega_H(X,a) &= \frac{a}{X^2+a^2}. \end{aligned} \tag{13}$$

Three distinct accelerations appear at $R = X$: the Kerr surface gravity $\kappa_{\mathrm{Kerr}} = (X^2-a^2)/\big(2X(X^2+a^2)\big)$, the physical Killing generator acceleration $\kappa_{\mathrm{phys}} = \sqrt{1-\ell^2/X^2}\,\kappa_{\mathrm{Kerr}}$, and the areal-normalized acceleration $\kappa_A = (1-\ell^2/X^2)\,\kappa_{\mathrm{Kerr}}$, unified in the one-parameter family $\kappa_n(X,a) := (1-\ell^2/X^2)^n \kappa_{\mathrm{Kerr}}$ $(n \in \{0, \frac{1}{2}, 1\})$. Adopting the areal-normalized Stefan–Boltzmann luminosity $L(\beta,\ell,X,a) = \beta(X^2+a^2)\kappa_A^4$ together with the one-parameter spin-shedding law

$$\frac{dM}{dv} = -L(\beta,\ell,X,a), \qquad \frac{dJ_{\mathrm{BH}}}{dv} = \gamma_{\mathrm{sh}}\,\frac{J_{\mathrm{BH}}}{M}\,\frac{dM}{dv}, \qquad \gamma_{\mathrm{sh}} \in \mathbb{R}, \tag{14}$$

captures constant angular momentum ($\gamma_{\mathrm{sh}} = 0$), constant spin length ($\gamma_{\mathrm{sh}} = 1$), constant spin ratio $a/X = t$ ($\gamma_{\mathrm{sh}} = 2$), and rapid Hawking spin-down ($\gamma_{\mathrm{sh}} > 2$) within a single smooth dynamical system.

Theorem 3.7 (Global coupled spin-down evaporation, remnant dichotomy, and Page-time rescaling)**.** *For every shedding index* $\gamma_{\mathrm{sh}} \in \mathbb{R}$, $\beta > 0$, $\ell > 0$, *and initial state* $\ell < X_0$, $0 \le a_0 < X_0$:

1. Global C^∞ existence, uniqueness, and first integral: *The coupled system Eq.* (14) *admits a unique global* C^∞ *solution* $(X(v), a(v))$ *on* $[0,\infty)$ *lying on the exact first-integral curve*

$$a(v) = a_0\left(\frac{M(v)}{M_0}\right)^{\gamma_{\mathrm{sh}}-1}, \qquad \frac{a(v)}{M(v)} = \frac{a_0}{M_0}\left(\frac{M(v)}{M_0}\right)^{\gamma_{\mathrm{sh}}-2}. \tag{15}$$

   The dimensionless Kerr spin ratio a/M *decreases strictly for* $\gamma_{\mathrm{sh}} > 2$, *stays constant for* $\gamma_{\mathrm{sh}} = 2$, *and increases for* $\gamma_{\mathrm{sh}} < 2$.

2. Throat-versus-extremal remnant dichotomy: *As* $v \to \infty$, *the temperature and luminosity vanish monotonically and the black hole approaches a finite zero-temperature remnant* $(X_{\mathrm{rem}}, a_{\mathrm{rem}})$ *satisfying either* $X_{\mathrm{rem}} = \ell$ *(throat remnant, forced unconditionally for all* $\gamma_{\mathrm{sh}} \ge 2$ *with* $M_{\mathrm{rem}} \in [\ell/2, \ell]$*) or* $a_{\mathrm{rem}} = X_{\mathrm{rem}}$ *(extremal-spin remnant, occurring e.g. at* $\gamma_{\mathrm{sh}} = 1$ *whenever* $a_0 > \ell$, *with* $M_{\mathrm{rem}} = a_0$*). Along the entire history, the literal four-dimensional Kretschmann scalar remains uniformly bounded by the initial-mass cap* $|K| \le K_{\mathrm{bound}}(M_0, M_0, \ell)$.

3. Exact constant-ratio Page-time shift: *At constant spin ratio* $\gamma_{\mathrm{sh}} = 2$ *(*$a(v) = tX(v)$, $t^2 < 1$*), the rotating trajectory equals the spin-zero trajectory evaluated at the rescaled advanced time* $c(t)^4 v$

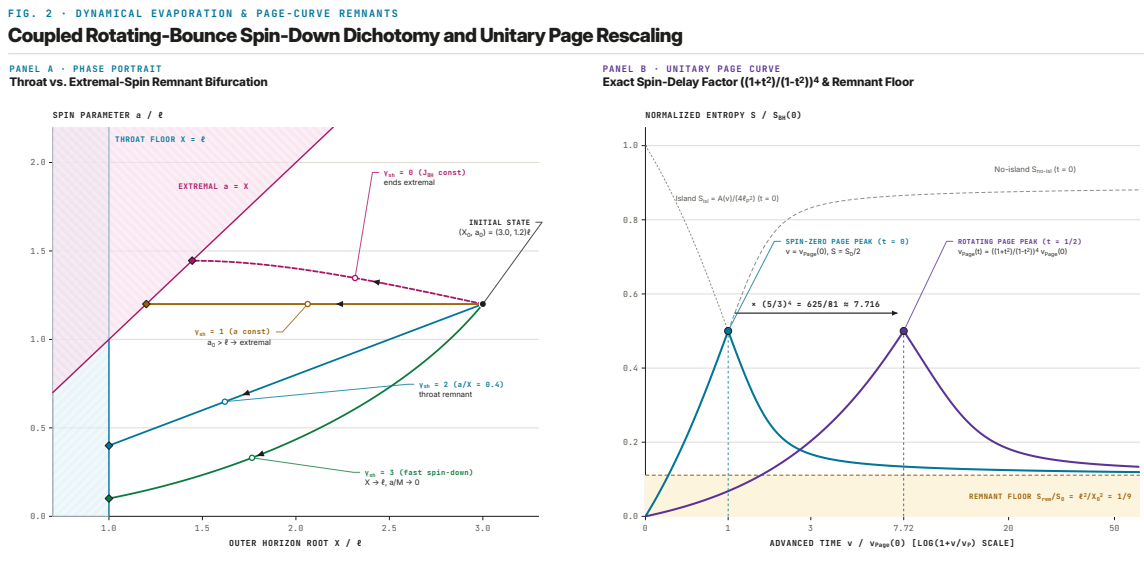

Fig. 2 Coupled rotating-bounce spin-down phase portrait and unitary Page curve (Theorem 3.7). **Panel A:** Exact orbits Eq. (15) in the $(X/\ell, a/\ell)$ plane starting from $(X_0, a_0) = (3.0, 1.2)\ell$. Orbits with $\gamma_{\rm sh} \geq 2$ terminate on the throat remnant boundary $X = \ell$, whereas $\gamma_{\rm sh} = 0$ and $\gamma_{\rm sh} = 1$ ($a_0 > \ell$) terminate on the extremal-spin boundary $a = X$. **Panel B:** Unitary Page curves $S_{\rm rad}(v)/S_{\rm BH}(0)$ at $t = 0$ (cyan) and $t = 1/2$ (violet) integrated on a log-spaced grid, displaying the exact Page-time delay factor $(5/3)^4 = 625/81 \approx 7.716$ above the finite remnant entropy floor $\ell^2/X_0^2 = 1/9$.

with $c(t) = (1-t^2)/(1+t^2)$. *Consequently, the unitary Page transition* ($S_{\rm island} = S_{\text{no-island}}$) *occurs if and only if* $X_0^2 > 2\ell^2$ *(independent of* t*), has an exact finite remnant entropy floor* $S_{\rm rem} = (\ell^2/X_0^2)S_0$*, and is delayed relative to spin zero by the exact factor*

$$v_{\rm Page}(t) = \left(\frac{1+t^2}{1-t^2}\right)^4 v_{\rm Page}(0) \qquad \left(e.g.\ t = \tfrac{1}{2} \implies \frac{v_{\rm Page}}{v_{\rm Page}(0)} = \frac{625}{81} \approx 7.716049\right). \tag{16}$$

For general $\gamma_{\rm sh}$ *satisfying* $\gamma_{\rm sh} \leq 2$ *or* $(\gamma_{\rm sh}-1)a_0^2 < X_0^2$*, the Page transition exists if and only if* $2A(X_{\rm rem}, a_{\rm rem}) < A(X_0, a_0)$.

Proof outline. Substituting $J_{\rm BH} = aM$ into Eq. (14) gives $M\,da/dv + a\,dM/dv = \gamma_{\rm sh} a\,dM/dv$, which separates directly to $da/a = (\gamma_{\rm sh}-1)\,dM/M$ and integrates immediately to Eq. (15). Eliminating $a(M)$ reduces the two-dimensional flow to the scalar autonomous ODE $dM/dv = -\tilde{L}(M)$, where $\tilde{L}(M) = \beta(X^2+a^2)(1-\ell^2/X^2)^4\kappa_{\rm Kerr}^4$ is smooth, strictly positive on the open interval $(M_{\rm rem}, M_0]$, and vanishes as a fourth power at whichever boundary ($X = \ell$ or $a = X$) is reached first. Consequently, the integral $\int_M^{M_0} du/\tilde{L}(u)$ diverges as $M \to M_{\rm rem}^+$, guaranteeing global C^∞ existence on $[0,\infty)$ without finite-time termination. For $\gamma_{\rm sh} = 2$, $a(v) = tX(v)$ gives $M(X) = \frac{1}{2}(1+t^2)X$, $\kappa_{\rm Kerr}(X, tX) = c(t)/(2X)$, and $L(X, tX) = \frac{1}{16}\beta(1+t^2)c(t)^4(1-\ell^2/X^2)^4/X^2$, so $dX/dv = c(t)^4(dX/dv)|_{t=0}$. The Page crossing $A(X, tX) = \frac{1}{2}A(X_0, tX_0)$ simplifies identically to $X = X_0/\sqrt{2}$ (independent of t), producing Eq. (16). □

Figure 2 illustrates both the coupled phase-portrait bifurcation across $\gamma_{\rm sh} \in \{0,1,2,3\}$ (Panel A) and the exact 625/81 constant-ratio Page-time delay above the finite remnant entropy floor $S_{\rm rem}/S_0 = 1/9$ (Panel B).

Direct four-dimensional Fréchet differentiation of the full dynamical rotating-bounce metric $g_{\mu\nu}(v, r, \chi) = g_{\mu\nu}^{\rm Kerr}(M(v), a(v), R(r), \chi)$ along any C^∞ spin-down history $(M(v), a(v))$ of Theorem 3.7 connects the bulk geometry directly to the far-rim fluxes and horizon thermodynamics:

Theorem 3.8 (Dynamical rotating-bounce field equations, Clausius uniqueness, and retarded QES)**.** *Along any* C^3 *history* $(M(v), a(v))$ *(in particular, every* C^∞ *solution of Theorem 3.7, witnessed explicitly at* $\gamma_{\rm sh} = 2, \beta = \ell = 1, X_0 = 2, a_0 = \frac{1}{2}$ *where* $M_0 = \frac{17}{16}$*,* $M'(0) < 0$*,* $a'(0) < 0$*):*

1. Exact 4D Einstein split and conservation: *At every off-axis point ($r \in \mathbb{R}$, including the throat $r = 0$), the full Einstein tensor splits into the stationary bounce tensor at frozen $(M(v), a(v))$ plus an explicit flux tensor in (M', M'', a', a'') with $G^{\mathrm{flux}}_{rr} = 0$, preserving the localized throat NEC violation $G_{rr} = -2\ell^2/\Sigma^2 < 0$, exact covariant conservation $\nabla_\mu T^\mu{}_\nu = 0$, exact axial Noether identity $\partial_\mu(\Sigma G^\mu{}_{\bar\varphi}) = 0$, and exact energy balance $\partial_\mu(\Sigma G^\mu{}_v) = \frac{1}{2}\Sigma G^{\mu\lambda}\partial_v g_{\mu\lambda}$.*
2. Far-rim energy/torque dichotomy: *For frozen spin length ($a' = a'' = 0$), the sphere-integrated flux $\oint \sqrt{-g}\, T_{vv}\, d\chi\, d\bar\varphi/(8\pi)$ and torque $\oint \sqrt{-g}\, T_{v\bar\varphi}\, d\chi\, d\bar\varphi/(8\pi)$ converge as $r \to \infty$ to $M'(v)$ and $-aM'(v)$ respectively (with zero contribution from the stationary core); conversely, whenever $a' \neq 0$ or $a'' \neq 0$, the naive Kerr–Vaidya torque integral diverges as $r \to \infty$, revealing a sharp asymptotic obstruction for varying-a ingoing Kerr–Vaidya ansätze.*
3. Exact Clausius surface-gravity uniqueness: *Across the acceleration family $\kappa_n = (1-\ell^2/X^2)^n \kappa_{\mathrm{Kerr}}$, the first-law heat flux obeys*

$$\frac{2\pi\big(M' - \Omega_H J'_{\mathrm{BH}}\big)}{\kappa_n(X,a)} \;=\; \left(1 - \frac{\ell^2}{X^2}\right)^{-n} \frac{A'}{4}. \tag{17}$$

Matching the horizon Bekenstein–Hawking bit loss $A'/(4G\ln 2)$ along all (X', a') selects the Kerr surface gravity $\kappa = \kappa_{\mathrm{Kerr}}$ ($n = 0$) uniquely; using the areal acceleration κ_A ($n = 1$) generates a logarithmic throat divergence $\pi\ell^2 \ln(X^2 - \ell^2)/G$ as $X \to \ell^+$.
4. Unique non-frozen retarded QES: *Defining the cumulative horizon clock $\tau_{\mathrm{cl}}(u) = \int_0^u \kappa(s)\, ds$ and retarded cut time $u^*(\rho)$ by $\tau_{\mathrm{cl}}(v) - \tau_{\mathrm{cl}}(u^*) = \ln\big((r_H - \rho)/\delta\big)$, the non-frozen generalized entropy is stationary ($\partial_\rho S_{\mathrm{gen}} = 0$) if and only if*

$$\rho(r_H - \rho) = c\big(u^*(\rho)\big), \qquad c(u) = \frac{\Gamma(u)\,\ell_{\mathrm{P}}^2}{2\pi\kappa(u)}. \tag{18}$$

Whenever $c(u)$ is nondecreasing on $[0, v]$, the retarded QES equation Eq. (18) possesses at most one interior root in $[r_H/2, r_H - \delta]$, yielding a unique dynamical island boundary.

Proof outline for parts 3–4. Differentiating Eq. (13) directly yields $M' - \Omega_H J'_{\mathrm{BH}} = \frac{X^2-a^2}{2X(X^2+a^2)}\big(XX' + aa'\big) = \kappa_{\mathrm{Kerr}}\, A'/(8\pi)$. Dividing by $\kappa_n = (1 - \ell^2/X^2)^n \kappa_{\mathrm{Kerr}}$ gives Eq. (17) identically; at $n = 1$ and fixed a, integrating $(X^2/(X^2 - \ell^2)) \cdot 2\pi X\, dX = 2\pi X\, dX + \pi\ell^2\, d\ln(X^2 - \ell^2)$ exhibits the logarithmic divergence as $X \to \ell^+$. For the retarded QES Eq. (18), differentiating $\tau_{\mathrm{cl}}(u^*(\rho)) = \tau_{\mathrm{cl}}(v) - \ln((r_H - \rho)/\delta)$ shows $\kappa(u^*)\, du^*/d\rho = (r_H - \rho)^{-1} > 0$, so $u^*(\rho)$ is strictly increasing in ρ. When $c(u)$ is nondecreasing, the right-hand side $c(u^*(\rho))$ is nondecreasing on $[r_H/2, r_H - \delta]$, whereas the left-hand side $\rho(r_H - \rho)$ is strictly decreasing there (since $r_H - 2\rho < 0$ on $(r_H/2, r_H)$); hence at most one root can exist. □

To illustrate the smooth decaying-source bridge connecting the coupled spin-down ODE of Theorem 3.7 to the four-dimensional dynamical Einstein tensor of Theorem 3.8, consider the concrete constant-ratio witness $\gamma_{\mathrm{sh}} = 2, \beta = \ell = 1, X_0 = 2, a_0 = \frac{1}{2}$ (hence $t = 1/4$). At $v = 0$, the initial horizon mass is $M_0 = \frac{17}{16}$, the Kerr surface gravity is $\kappa_{\mathrm{Kerr}}(0) = \frac{15}{68}$, the areal acceleration is $\kappa_A(0) = \frac{3}{4}\kappa_{\mathrm{Kerr}}(0) = \frac{45}{272}$, and the luminosity $L(0) = \frac{17}{4}(45/272)^4 \approx 3.184 \times 10^{-3}$ drives strictly negative initial rates $M'(0) = -L(0) < 0$ and $a'(0) = -(a_0/M_0)L(0) \approx -1.498 \times 10^{-3} < 0$. Because the solution $(M(v), a(v))$ is globally C^∞ with $M'(v), M''(v), a'(v), a''(v) \to 0$ as $v \to \infty$, the dynamical flux tensor $G^{\mathrm{flux}}_{\mu\nu}(v, r, \chi)$ decays uniformly on every compact spatial slab while converging pointwise to the exact stationary zero-temperature throat remnant $(X_{\mathrm{rem}}, a_{\mathrm{rem}}) = (1, \frac{1}{4})$ ($M_{\mathrm{rem}} = \frac{17}{32}$), with zero curvature blow-up at any time $v \in [0, \infty)$ or radius $r \in \mathbb{R}$.

Table 3 collects the exact machine-verified numerical witnesses across all four subsections of Section 3.

Table 3 Quantitative witnesses and exact identities for dynamical black-hole evaporation, puncture ensembles, and rotating remnants (Section 3).

Result	Witness / Parameter Point	Exact / Certified Value
Catalan Page curve (Theorem 3.2)	$J = 6, k = 3$; $J = 12$ (24 faces)	$C_3 = 5$, $S = \ln 5 \approx 1.60944$; turnover $k^* = 5 < 6$
Barbero–Immirzi gap (Obstruction 3.4)	Binary RS vs. all-spin Casimir	$\gamma_{\mathrm{RS}} \approx 0.12738$, $\gamma_\infty \approx 0.27407$, $\theta_{\mathrm{RS}} \approx 2.15150$
J-cost partition flow (Obstruction 3.4)	$\lambda \in \{0, 10, 100\}$ at γ_{RS}	$\mathcal{Z} = 5.78306$, 1.31352, $1.0000045 > 1$; $\gamma(20) \approx 0.14154$
Hayward remnant (Theorem 3.5)	$M = 4\ell/3, r_+ = 2\ell$; extremal	$\kappa_{\mathrm{Hay}} = 1/(16\ell)$; $r_e = \sqrt{3}\ell$, $M_c = 3\sqrt{3}\ell/4$
Spin-down dichotomy (Theorem 3.7)	$(X_0, a_0) = (3.0, 1.2)\ell$, $\gamma_{\mathrm{sh}} \in \{1, 2, 3\}$	$\gamma_{\mathrm{sh}} = 1 \to$ extremal $X_{\mathrm{rem}} = 1.2\ell$; $\gamma_{\mathrm{sh}} \geq 2 \to$ throat $X_{\mathrm{rem}} = \ell$
Page-time delay (Theorem 3.7)	$\gamma_{\mathrm{sh}} = 2$, $t = a/X = 1/2$, $X_0 = 3\ell$	$v_{\mathrm{Page}}(1/2)/v_{\mathrm{Page}}(0) = 625/81 \approx 7.71605$; $S_{\mathrm{rem}}/S_0 = 1/9$
Clausius uniqueness (Theorem 3.8)	$\kappa_n = (1 - \ell^2/X^2)^n \kappa_{\mathrm{Kerr}}$	Exact $A'/4$ iff $n = 0$; $n = 1$ diverges as $\pi\ell^2 \ln(X^2 - \ell^2)/G$

4 Lorentzian EPRL Spin-Foam Vertices, Curved-Bulk Regge Stationary Phase, and Binary-Ledger Pell Realization

Covariant loop quantum gravity encodes spacetime transitions through four-dimensional spin-foam vertex amplitudes built from the unitary principal series of $\mathrm{SL}(2,\mathbb{C})$ [12;13]. Extracting genuine four-dimensional discrete general relativity from those amplitudes requires closing four hard mathematical gaps: (i) constructing the unitary $\mathrm{SL}(2,\mathbb{C})$ principal series and proving the exact parity-conjugate 44×44 transverse Hessian and varying invariant measure of the Lorentzian 4-simplex amplitude; (ii) determining whether a binary spin-1/2 ledger can realize a non-degenerate Lorentzian 4-simplex; (iii) proving complete orientation locking and non-degenerate multi-edge stationary phase on genuinely *curved*, causally regular multi-simplex triangulations; and (iv) connecting four-dimensional Pachner refinement, Ashtekar–Lewandowski quantum volume, and higher K-type $\Delta l = 1$ boost transitions directly to the canonical reciprocal cost $J(x)$.

4.1 Unitary $\mathrm{SL}(2,\mathbb{C})$ principal series, boost-norm J-cost law, and the 44×44 EPRL Hessian

In a rational rescaled K-type basis $\{e_{j,m}\}$ ($j = k + l$, $l \in \mathbb{N}$, $m = k + n$, $n \in \mathbb{Z}$) with level functions $D_j = -(j^2 - k^2)(j^2 + \rho^2)/(j^2(4j^2 - 1))$ and $B_j = k\rho/(j(j+1))$, the six Lorentz ladder operators (H_a, F_a) satisfy all 15 commutation relations of $\mathfrak{sl}(2,\mathbb{C})$ and carry exact operator Casimirs $H^2 - F^2 = k^2 - \rho^2 - 1$ and $H \cdot F = k\rho$. On the physical subquotient $|m| \leq j$, the positive weights $w(j,m) = \big(\prod_{i=1}^{j-k}(-D_{k+i})\big)(j+m)!/(j-m)! > 0$ render all six generators Hermitian, proving exact unitarity of the principal series (k, ρ) for every half-integer $k = K/2 > 0$ and real $\rho \in \mathbb{R}$.

Projecting onto the lowest K-type $j = k$ via P_z yields the exact weak linear-simplicity relation: for the EPRL choice $\rho = \gamma_{\mathrm{BI}} k$,

$$P_z\big(K_a - \gamma_{\mathrm{BI}} L_a\big)P_z = -\frac{\gamma_{\mathrm{BI}}}{k+1}\, P_z L_a P_z, \qquad P_z(K_a - \gamma_{\mathrm{BI}} L_a)P_z = 0 \iff \rho = \gamma_{\mathrm{BI}}(k+1). \tag{19}$$

Equivalently, the positive linear-simplicity master operator $M_{\mathrm{simp}} = \sum_{a=1}^{3}(K_a - \gamma_{\mathrm{BI}} L_a)^\dagger (K_a - \gamma_{\mathrm{BI}} L_a)$ attains its exact variational ground-state eigenvalue

$$\lambda_{\min}(n_0, \gamma_{\mathrm{BI}}) = (1 + \gamma_{\mathrm{BI}}^2)\frac{n_0}{2} + 1 = 2\gamma_{\mathrm{BI}}\frac{n_0}{2}\big(1 + J(\gamma_{\mathrm{BI}})\big) + 1 \tag{20}$$

uniquely on the lowest K-type $l = 0$ at $\rho = \gamma_{\mathrm{BI}} n_0/2$, separated by a strict spectral gap $2(n_0/2+1)(1+\gamma_{\mathrm{BI}}^2)$ from all $l \geq 1$ shells.

At the level of coherent boundary states on a non-degenerate Lorentzian 4-simplex with spacelike tetrahedra, each future-timelike unit tetrahedron normal $N = (N^0, \vec{N})$ ($\cosh\Theta = N^0$) determines a unique Hermitian positive $\mathrm{SL}(2,\mathbb{C})$ boost root $G_N = (I + X_N)/\sqrt{2(1+N^0)}$ ($G_N^2 = X_N = N^0 I + \vec{N}\cdot\vec{\sigma}$, $\det G_N = 1$). Acting on a unit coherent spinor $\xi \in \mathbb{C}^2$ aligned with $\pm\vec{N}/|\vec{N}|$, G_N stretches $\|\xi\|^2$ by $e^{\pm\Theta}$, while its parity partner $G_{PN} = G_N^{-1}$ stretches it by $e^{\mp\Theta}$. Both critical points share the *exact same* canonical reciprocal cost,

$$J\big(\|G_N\xi\|^2\big) = J(e^{\pm\Theta}) = \cosh\Theta - 1 = N^0 - 1 = J\big(\|G_{PN}\xi\|^2\big)\,, \tag{21}$$

differing solely in the sign of their EPRL face phase $e^{\pm i\gamma_{\mathrm{BI}} j_f \Theta_f}$.

On the explicit geometric witness 4-simplex p_W—formed by a regular spacelike tetrahedron base at $t = 0$ with four vertices $(0,1,1,1)$, $(0,1,-1,-1)$, $(0,-1,1,-1)$, $(0,-1,-1,1)$ (edge length $2\sqrt{2}$) and a timelike apex at $(t,\vec{x}) = (\frac{1}{2},0,0,0)$—all five boundary tetrahedra have strictly positive-definite 3×3 Gram matrices while the 4×4 edge matrix has negative determinant (confirming genuine $(-,+,+,+)$ Minkowski volume). Its 6 side–side faces carry boost dihedral angle $\cosh\Theta_{\mathrm{ss}} = 5$ ($J(e^{\Theta_{\mathrm{ss}}}) = 4$, area $A_{\mathrm{ss}} = \sqrt{6}/2$) and its 4 side–base faces carry $\cosh\Theta_{\mathrm{sb}} = 2$ ($J(e^{\Theta_{\mathrm{sb}}}) = 1$, area $A_{\mathrm{sb}} = 2\sqrt{3}$), yielding the signed Lorentzian Regge action

$$S_{\mathrm{Regge}}(p_W) = 6\cdot\frac{\sqrt{6}}{2}\,\mathrm{arcosh}\,5 - 4\cdot 2\sqrt{3}\,\mathrm{arcosh}\,2 \approx -1.40244033, \tag{22}$$

which obeys the general four-dimensional Lorentzian Schläfli identity $\sum_f A_f\, d\Theta_f/dt = 0$. In Lean 4, this Schläfli identity is proved directly in Minkowski signature without relying on Euclidean analytic continuation: contracting the derivative of the tetrahedron closure law $\sum_{a=0}^{4} V_a \hat{N}_a = 0$ (where $V_a > 0$ is the 3-volume and $\hat{N}_a$ the unit timelike normal) with each bivector B_{ab} and applying the Minkowski Law of Sines $\eta(N_a,N_b)^2 - N_a^2 N_b^2 = \mathrm{vol}_4^2(B_{ab}\cdot B_{ab})$ cancels every $\dot{\Theta}_f$ variation identically.

Writing the coherent-state EPRL vertex action $S_{\mathrm{EPRL}}(\gamma_{\mathrm{BI}}, j, \xi; g, z) = \sum_{f=1}^{10} S_f$ over five $\mathrm{SL}(2,\mathbb{C})$ frame matrices g_a and ten face spinors $z_f \in \mathbb{C}^2 \setminus \{0\}$ ($Z = g_a^\dagger z_f$, $W = g_b^\dagger z_f$), Cauchy–Schwarz gives $\mathrm{Re}\, S_{\mathrm{EPRL}} \leq 0$ with equality if and only if every face aligns ($Z \parallel \xi_{ab}, W \parallel J_{\mathrm{ant}}\xi_{ba}$). Fixing global $\mathrm{SL}(2,\mathbb{C})$ gauge ($g_4 = I$, 6 real dimensions) and projective face scaling ($z_f \mapsto c_f z_f$, 20 real dimensions) reduces the 70-dimensional traceless variation space ($5\times 6 = 30$ frame parameters plus $10\times 4 = 40$ spinor parameters) cleanly to $70 = 44 + 26$ transverse slice coordinates $x \in \mathbb{R}^{44}$ (24 real frame coordinates and 20 real $\mathbb{CP}^1$ face coordinates).

Theorem 4.1 (Uniqueness of critical points, 44×44 parity-conjugate Hessian, and varying-Haar λ^{-12} Regge cosine)**.** *For the geometric Lorentzian 4-simplex p_W with area-matched spins $j_f = \lambda A_f/c$ ($c > 0$, $\gamma_{\mathrm{BI}} \in \mathbb{R}$):*

1. Exact critical-point classification: *Modulo global* $\mathrm{SL}(2,\mathbb{C})$ *gauge, sign flips $\varepsilon_a \in \{\pm 1\}$, and projective face scaling, S_{EPRL} possesses* exactly two *non-equivalent critical points, (g_C, z_C) and its parity partner (g_P, z_P).*
2. Exact 44×44 Hessian and parity symmetry: *At both critical points, the 44×44 complex symmetric transverse Hessian H_{red} is non-degenerate ($\det H_{\mathrm{red}} \neq 0$). Composing spatial parity with the side-tetrahedron swap $x \leftrightarrow y$ induces a permutation-conjugation identity on the 24×24 frame Schur complement ($S_P(\sigma i,\sigma k) = \overline{S_C(i,k)}$), proving unconditionally for all γ_{BI} and $c \neq 0$:*

$$\begin{aligned} \det H_P &= (2-\sqrt{3})^{16}\,\overline{\det H_C}, \\ \|\mathrm{Nb}(H_P)\| &= (2+\sqrt{3})^8\,\|\mathrm{Nb}(H_C)\| = \big(18{,}817 + 10{,}864\sqrt{3}\big)\|\mathrm{Nb}(H_C)\|, \end{aligned} \tag{23}$$

   where $\mathrm{Nb}(H)$ is the canonical homotopy branch of $\det(-H)^{-1/2}$ (numerically $(2+\sqrt{3})^8 = 37{,}634 - (2-\sqrt{3})^8 \approx 37{,}633.999973$, with exact algebraic trace $(2+\sqrt{3})^8 + (2-\sqrt{3})^8 = 37{,}634$).
3. Exact varying invariant measure and $\lambda^{-12} + O(\lambda^{-13})$ Regge cosine: *In the Cayley frame chart $g_a(x) = G_a(I + Y_a/2)(I - Y_a/2)^{-1}$ and affine $\mathbb{CP}^1$ face charts, the full left-invariant* $\mathrm{SL}(2,\mathbb{C})^4 \times$

$(\mathbb{CP}^1)^{10}$ *Haar–Fubini–Study density is identical at both critical points,*

$$\mu(x) = \prod_{a=0}^{3} \left| 1 + \frac{1}{4} \det Y_a(x) \right|^{-6} \prod_{f=1}^{10} \left(1 + |w_f(x)|^2\right)^{-2}, \qquad \mu(0) = 1, \quad \nabla\mu(0) = 0. \tag{24}$$

Combining multivariate complex stationary phase (proved without the Morse lemma via the Laplace homotopy $S_t = S - (t/2)|x|^2$) with the exact $\mathbb{CP}^1$ propagator normalization cancels the $(2+\sqrt{3})^8$ factor identically and yields the unconditional large-spin vertex law (with $C > 0$ independent of $\lambda \geq 1$):

$$\left| \lambda^{12} \left(\prod_{f=1}^{10} (2\lambda j_f + 1) \right) \mathcal{A}_{\mathrm{EPRL}}(\lambda) - 2^{10} \left(\prod_{f=1}^{10} j_f \right) 2|N_+| \cos\!\left(\lambda \frac{\gamma_{\mathrm{BI}}}{c} S_{\mathrm{Regge}}(p_W) + \arg N_+ \right) \right| \leq \frac{C}{\lambda}, \tag{25}$$

where the variation $\mu(x) - 1$ enters strictly at subleading order $O(\lambda^{-13})$.

Proof outline. Block-partitioning the 44×44 transverse Hessian into its 20×20 diagonal face block H_{zz} (10 decoupled 2×2 blocks) and 24×24 frame block H_{gg} via the Schur complement $S_{\mathrm{frame}} = H_{gg} - H_{gz} H_{zz}^{-1} H_{zg}$ yields $\det H_{\mathrm{red}} = (\det H_{zz})(\det S_{\mathrm{frame}})$. Under spatial parity composed with the side-tetrahedron swap $x \leftrightarrow y$, every entry of S_{frame} conjugates up to a signed coordinate permutation ($\det S_P = \overline{\det S_C}$), while the 4 side–base face blocks scale by $(e^{-2\Theta_{\mathrm{sb}}})^4 = (2-\sqrt{3})^{16}$ because $\cosh \Theta_{\mathrm{sb}} = 2 \implies e^{-\Theta_{\mathrm{sb}}} = 2 - \sqrt{3}$ (giving Eq. (23)). Exactly this factor $(2+\sqrt{3})^8 = 18{,}817 + 10{,}864\sqrt{3}$ cancels against the $\mathbb{CP}^1$ inner-product normalization $\prod_f \|z_f\|^{-4}$ at the parity saddle, leaving exact conjugate amplitudes $N_- = \overline{N_+}$. To avoid the classical Morse lemma for complex-valued phase functions with $\mathrm{Re}\, S \leq 0$, the stationary-phase integral over $\mathbb{R}^{44}$ is evaluated by integrating the Taylor difference $e^{\lambda S(x)} - e^{\lambda Q(x)}$ along the Gaussian-damped homotopy $S_t(x) = Q(x) + t(S(x) - Q(x))$ on a ball of radius $\lambda^{-1/3}$, where $\mathrm{Re}\, Q(x) \leq -c_0|x|^2$ controls every cubic and quartic remainder together with the quadratic Haar–Fubini–Study deviation $\mu(x) - 1 = O(|x|^2)$ to $O(\lambda^{-23})$ (i.e. $O(\lambda^{-1})$ relative to the leading λ^{-22} saddle and λ^{-13} after multiplying by $\prod_f (2\lambda j_f + 1) \sim \lambda^{10}$). □

4.2 Equal-area no-go obstruction and binary-ledger Pell realization

In a binary spin-1/2 ledger where every elementary face quantum carries spin 1/2, a single homogeneous spin-1/2 boundary ($j_f = \frac{1}{2}$ on all ten triangles) requires ten equal triangle areas. Can *any* non-degenerate Lorentzian 4-simplex with spacelike tetrahedra satisfy that condition?

Obstruction 4.2 (No equal-area non-degenerate Lorentzian 4-simplex)**.** *Let $p : \{0, \ldots, 4\} \to \mathbb{R}^{1,3}$ be five vertices in Minkowski space with non-degenerate edge matrix ($\det E(p) \neq 0$) whose five boundary tetrahedra are all spacelike (strictly positive-definite 3×3 Gram matrices). Then there exists* no *positive constant $A_0 > 0$ such that all ten triangle areas equal A_0. (On symmetric pyramids over a regular spacelike base of edge l_b and timelike apex height $h > 0$, the area-squared ratio obeys $A^2_{\mathrm{side}}/A^2_{\mathrm{base}} = \frac{1}{6} - \frac{4}{3}(h/l_b)^2 < \frac{1}{6} < 1$ strictly.)*

Proof outline. Because every boundary tetrahedron is spacelike (positive-definite 3×3 Gram matrix), all five tetrahedra are non-degenerate ($\det G_{\mathrm{tet}} \neq 0$) and every triangle is spacelike, so equal triangle areas $A_f = A_0 > 0$ imply equal Heron quantities $H_{ijk} = 16A_0^2$ across all ten triangles of the 4-simplex. For any single non-degenerate tetrahedron, four equal face Heron quantities force opposite pairs of squared edge lengths to coincide (every boundary tetrahedron is disphenoid). Propagating this opposite-edge equality across all five boundary tetrahedra of the complete graph K_5 forces *all* ten squared edge lengths of the 4-simplex to be equal ($s_{ij} = s$). The resulting 4×4 edge Gram matrix has entries $G_{ij} = \frac{1}{2}s(1 + \delta_{ij})$ with determinant $\det G = \frac{5}{16}s^4 \geq 0$, which satisfies $(\det E)^2 \prod_{k=0}^{3} g_k = \det G = \frac{5}{16}s^4 \geq 0$ for any diagonal metric $\mathrm{diag}(g_0, g_1, g_2, g_3)$. In Lorentzian signature $(-,+,+,+)$, $\prod_{k=0}^{3} g_k = -1$, yielding $-(\det E)^2 = \frac{5}{16}s^4 \geq 0$ and contradicting $\det E \neq 0$. □

Obstruction 4.2 shows that a binary ledger cannot realize a Lorentzian 4-simplex with one voxel per face; instead, each face f must carry an integer number $n_f = 2j_f \in \mathbb{N}_{\geq 1}$ of elementary spin-1/2 voxels whose Casimir area $\sqrt{j_f(j_f+1)} = \frac{1}{2}\sqrt{(n_f+1)^2-1}$ matches the exact geometric area ratios of the simplex. For p_W, where $A_{\rm sb}/A_{\rm ss} = 2\sqrt{2}$ (with reciprocal cost $J(2\sqrt{2}) = 9\sqrt{2}/8 - 1 \approx 0.590990$), exact integer voxel matching requires $(n_{\rm sb}+1)^2 - 1 = 8\big((n_{\rm ss}+1)^2 - 1\big)$, which is an exact negative Pell equation.

Theorem 4.3 (Binary-ledger Pell realization of p_W and Pell-sequence Regge cosine)**.** *Setting $X = n_{\rm sb}+1$ and $Y = n_{\rm ss}+1$, exact Casimir area matching of p_W in the binary spin-1/2 voxel ledger holds if and only if*

$$X^2 - 8Y^2 = -7, \qquad Y \geq 2 \implies X \geq 5. \tag{26}$$

The fundamental Pell unit $(3,1)$ generates two disjoint infinite towers of exact realizations via $(X', Y') = (3X + 8Y,\ X + 3Y)$:

$$\textit{Class 1:}\quad (X_k, Y_k) = (5,2),\ (31,11),\ (181,64),\ (1055,373),\ \ldots \tag{27}$$

$$\textit{Class 2:}\quad (\tilde{X}_k, \tilde{Y}_k) = (11,4),\ (65,23),\ (379,134),\ \ldots \tag{28}$$

The minimal realization $(5,2)$ assigns $j_{\rm ss} = \frac{1}{2}$ (1 voxel) to each side–side face and $j_{\rm sb} = 2$ (4 voxels) to each side–base face. Along the Pell tower $k \to \infty$, the quantized spins satisfy $j_f^{(k)} = \lambda_k j_A(f) - \frac{1}{2} + \eta_k \mathbf{1}_{\rm sb}(f)$ with $\lambda_k \to \infty$ and $|\eta_k| = O(\lambda_k^{-1})$, and the exact quantized EPRL vertex amplitude converges to the Regge cosine Eq. (25) with an exact constant half-spin phase shift $\gamma_{\rm BI}(2\,\mathrm{arcosh}\,2 - 3\,\mathrm{arcosh}\,5)$ and remainder $O(\lambda_k^{-1})$.

The constant half-spin phase shift in Theorem 4.3 arises directly from replacing the classical area-proportional spin $\lambda_k A_f/c$ by the quantized integer-voxel spin $j_f^{(k)} = \frac{1}{2}(X_k - 1)$ or $\frac{1}{2}(Y_k - 1)$: since $X_k - 2\sqrt{2}\,Y_k = -7/(X_k + 2\sqrt{2}\,Y_k) = O(Y_k^{-1})$, the uniform $-\frac{1}{2}$ shift across the 4 side–base faces (angle $-\Theta_{\rm sb}$) and 6 side–side faces (angle $+\Theta_{\rm ss}$) contributes $\gamma_{\rm BI}\big((-4)(-\frac{1}{2})\,\mathrm{arcosh}\,2 + 6(-\frac{1}{2})\,\mathrm{arcosh}\,5\big) = \gamma_{\rm BI}(2\,\mathrm{arcosh}\,2 - 3\,\mathrm{arcosh}\,5)$ identically to every rung of both Pell towers.

4.3 Causally regular asymmetric curved bulk stars, 126/128 locking, and 2D Regge Hessian

Gluing multiple Lorentzian 4-simplices around interior hinges introduces 2^{N_σ} orientation sectors $\varepsilon \in \{\pm 1\}^{N_\sigma}$ and bulk Regge field equations $\partial S/\partial l_e = \sum_{h \ni e} (\partial A_h/\partial l_e)\varepsilon_h = 0$ (whose hinge-angle derivative terms cancel identically by the Lorentzian Schläfli identity). A crucial subtlety uncovered during formal auditing is that *causally regular* hinges (exactly four null rays in the normal plane of each spacelike triangle, i.e., two thick wedges and one thin wedge) on a pairing-symmetric link ($\iota = (0\,1)(2\,3)$) fail to lock the partially flipped sectors $\pm(+,+,-,-)$, leaving 2 spurious stationary sectors alongside the two global sectors $\pm(+,+,+,+)$.

Breaking link symmetry completely closes this multi-simplex orientation-locking obstruction on both single-edge and coupled two-edge curved Lorentzian complexes:

Theorem 4.4 (Asymmetric curved bulk star, 7-simplex complex, and 2D Hessian)**.** *For curved multi-simplex Lorentzian triangulations, the following hold:*

1. Asymmetric causally regular 4-simplex star (14/14 locking): *The integer link Gram matrix*

$$G_A = \begin{pmatrix} 64 & -38 & 12 & 2 \\ -38 & 25 & -13 & 7 \\ 12 & -13 & 9 & -13 \\ 2 & 7 & -13 & 25 \end{pmatrix}, \qquad \det G_A = -3344 \neq 0, \tag{29}$$

admits no flat Minkowski 3-space realization and defines four glued non-degenerate Lorentzian 4-simplices around an interior spacelike edge of length $l_a = 13$ with heights $(5,8,0,8)$. Every interior hinge is causally regular (4 null rays), the complex is time-orientable, the four interior deficits are nonzero and pairwise distinct $(\ln(7/3), \ln 6, \ln 4, \ln(14/9))$, the bulk Regge equation holds exactly via $(7/3)\cdot 4 = 6\cdot(14/9) = 28/3$ with area rates $(\frac{3}{2}, -\frac{3}{2}, \frac{3}{2}, -\frac{3}{2})$, and all 14/14 mixed orientation sectors are strictly non-stationary (suppressed as $O(\lambda^{-N})$ for every $N \in \mathbb{N}$).

2. Coupled two-edge 7-simplex curved complex (126/128 locking and negative-definite 2D Hessian): *Extending the star to a 7-simplex cone $K = b * B$ over a 7-tetrahedron 3-ball B with two coupled interior edges $l_a = 13$ and $l_c = \sqrt{89}$ satisfies both coupled bulk Regge equations simultaneously by exact multi-edge Schläfli variation, locks all 126/128 mixed orientation sectors ($\forall b \neq \pm\mathbf{1}$, oscillatory integrals decay as $O(\lambda^{-N})$), and possesses a strictly negative-definite 2×2 bulk Regge Hessian at $(13, \sqrt{89})$:*

$$\begin{aligned} H_{aa} &= -\frac{77}{104}\ln\frac{7}{3} - \frac{193}{130}\ln 6 - \frac{13}{6}\ln 4 - \frac{193}{130}\ln\frac{14}{9} - \frac{411}{338} \approx -8.16297 < -\frac{15}{2}, \\ H_{ac} &= \frac{8\sqrt{89}}{65}\ln 6 + \frac{297\sqrt{89}}{884} \approx +5.24998, \\ H_{cc} &= -\frac{29281}{1768} - \frac{1424}{195}\ln 6 \approx -29.64609 < -\frac{289}{10}, \end{aligned} \tag{30}$$

with $\det H = H_{aa}H_{cc} - H_{ac}^2 \approx 214.4377 > 0$ *(eigenvalues* -30.8604 *and* -6.9486*).*

3. Quantitative rational ball and genuine complex-prefactor glued cosine: *There exists an explicit rational radius $q \in \mathbb{Q}_{>0}$ such that on the metric ball $B\big((13, \sqrt{89}), q\big) \subset \mathbb{R}^2$, every simplex remains Lorentzian, the glued action $S_K(l_a, l_c)$ is C^∞, and $D^2 S_K$ stays strictly negative definite; furthermore, combining genuine parity-conjugate complex vertex prefactors $N_i = |N_i| e^{i \arg N_i}$ retires any real-prefactor ansatz and yields the glued* 2D *stationary-phase cosine with explicit $O(\lambda^{-1})$ remainder.*

Proof outline. For each orientation sector $b \in \{\pm 1\}^4$ on the 4-simplex star, stationarity with respect to the interior edge l_a requires $\sum_{h=1}^{4} (\partial A_h / \partial l_a)\, \varepsilon_h(b) = 0$. Because the four interior area rates alternate as $(\frac{3}{2}, -\frac{3}{2}, \frac{3}{2}, -\frac{3}{2})$, this condition collapses to a linear equation over $\mathbb{Z}$ in $\ln(7/3), \ln 6, \ln 4, \ln(14/9)$ and the individual dihedral angles. Unique prime factorization of $(2, 3, 7)$ proves that the logarithmic combinations vanish if and only if $b = +(1,1,1,1)$ or $b = -(1,1,1,1)$, eliminating all 14 mixed sectors by non-stationary integration by parts ($O(\lambda^{-N})$). On the 7-simplex complex K, coupling the second interior edge $l_c = \sqrt{89}$ enforces the same locking inductively across all 7 simplices ($128 - 2 = 126$ mixed sectors strictly non-stationary), while exact rational lower/upper brackets on $\ln 2, \ln 3, \ln 7$, and $\sqrt{89}$ certify $H_{aa} < -15/2$, $H_{cc} < -289/10$, and $H_{aa}H_{cc} - H_{ac}^2 > 0$, proving negative-definiteness without floating-point arithmetic. □

4.4 Quantum recoupling, Stasheff pentagon gap, 5-tier Pachner hierarchy, and $\Delta l = 1$ boost zero-crossing

Complementing the coherent-state saddle analysis, exact finite-dimensional tensor-product spin-network calculations establish the algebraic recoupling, quantum volume, and Pachner dynamics across arbitrary spins $j = n/2$:

Theorem 4.5 (Quantum volume, pentagon gap, Pachner hierarchy, and $\Delta l = 1$ selection)**.** *On finite-dimensional* SU(2) *and* $\mathrm{SL}(2, \mathbb{C})$ *intertwiner spaces, the following hold:*

1. Universal 3-valent zero volume and 4-valent Ashtekar–Lewandowski volume: *On $V_{n_1/2} \otimes V_{n_2/2} \otimes V_{n_3/2}$, the Ashtekar–Lewandowski volume commutator $Q_3 = -\frac{i}{4}[J_{12}^2, J_{23}^2]$ vanishes identically on every* SU(2)*-invariant 3-valent intertwiner, forcing 4-valent tetrahedra as the minimal quantum of 3-volume in $D = 3$. On 4-valent intertwiners, Q_4 is Hermitian, commutes with* SU(2) *Gauss generators, anticommutes with crossing moves ($FQF = -Q$), and couples non-commutatively with Thiemann's Euclidean and Lorentzian constraints ($[C_E, C_L] \neq 0$, lifting spurious Euclidean zero modes to $\gamma_{\mathrm{BI}}^2 v^{10} > 0$).*
2. Stasheff pentagon golden-ratio gap: *On the 5-valent recoupling space $\mathbb{C}^{20}$ (and embedded into $\mathbb{C}^{108}$), the Biedenharn–Elliott pentagon identity diagonalizes the $2 \leftrightarrow 3$ Pachner Master Constraint as $U^\dagger M_{\mathrm{pent}} U = L_{C_5} \otimes I_4$, with exact minimal polynomial $L(L^2 - 5L + 5I) = 0$, exact golden-ratio spectral gap $\Delta_{\mathrm{pent}} = 3 - \varphi = (5 - \sqrt{5})/2 \approx 1.38197$, excited ratio $(2 + \varphi)/(3 - \varphi) = \varphi^2$, and complete kernel collapse under any $\mathbb{Z}_2$ pentagon anomaly (floor $2 - \varphi = \varphi^{-2} > 0$).*
3. Exact 5-tier 4D Pachner Ooguri GHZ purity hierarchy: *Factorizing the D_{10}-symmetric* 4D *Ooguri $\{15j\}_I$ vertex amplitude on $K_5 = \partial\Delta_4$ into the Plancherel-weighted GHZ state*

$\sum_{r=0}^{n}(2r+1)^{-3/2}|f_r\rangle^{\otimes 5}$ *(with Wigner* $9j$ *reductions witnessed by* $\left\{\begin{smallmatrix}1/2 & 1/2 & 1\\ 1/2 & 1/2 & 1\\ 1 & 1 & 2\end{smallmatrix}\right\}=\frac{1}{9}$ *and parity-zero* $\left\{\begin{smallmatrix}1/2 & 1/2 & 1\\ 1/2 & 1/2 & 1\\ 1 & 1 & 1\end{smallmatrix}\right\}=0$*) and gluing* $1,2,3,4,5$ *four-simplices across the* $2\leftrightarrow 3$*,* $2\leftrightarrow 4$*, and* $1\leftrightarrow 5$ *Pachner moves produces UV-finite norms (*$Z_{K_5}(1)=\frac{28}{27}$*,* $Z_{\mathrm{glued8}}(1)=\frac{730}{729}$*, all* $<569/540$*) and a strict* 5*-tier holographic purity hierarchy across both* $1|4$ *and* $2|3$ *cuts:*

$$0<\mathcal{P}_{K_5}(n)<\mathcal{P}_{\mathrm{glued8}}(n)<\mathcal{P}_{P_{2\leftrightarrow 3}}(n)<\mathcal{P}_{P_{2\leftrightarrow 4}}(n)<\mathcal{P}_{P_{1\leftrightarrow 5}}(n)<1 \tag{31}$$

for every $n\geq 1$*, starting at* $\mathcal{P}_{K_5}(1)=\frac{365}{392}\approx 0.931122$ *(*$j=1/2$*) and* $\frac{11406979}{12439729}\approx 0.916980$ *(*$j=1$*). Under Lorentzian EPRL* $1\leftrightarrow 5$ *stellar subdivision, the binary spin-*$1/2$ *state is strictly distortion-free (an exact scalar multiple of the Ooguri state for all* $\gamma_{\mathrm{BI}}\in\mathbb{R}$*), whereas every higher spin* $j\in\{1,\frac{3}{2},2\}$ *suffers unconditional non-proportional Lorentzian curvature distortion.*

4. $\Delta l=1$ boost selection and unit-cost rapidity $\Theta=\operatorname{arcosh}2$: *Across the* $16=1+4+6+4+1$ *four-valent* $\Delta l=1$ K*-type shells of* $(1/2\oplus 3/2)^{\otimes 4}$*,* 1*-excited-face transitions vanish identically,* 3*-face transitions activate strictly via* $\gamma_{\mathrm{BI}}\neq 0$ *phase interference,* 4*-face transitions intertwine* Q_4 *by exact factor* $3=D$*, and at the unit-cost rapidity* $\Theta=\operatorname{arcosh}2$*,*

$$J(e^{\Theta})=1,\qquad \sinh^2\Theta=3=D,\qquad J(e^{2\Theta})=6=2D, \tag{32}$$

the excited $l=3/2\to 3/2$ *diagonal* $\mathrm{SL}(2,\mathbb{C})$ *boost matrix element vanishes identically.*

Physically, the $\Delta l=1$ zero-crossing at $\Theta=\operatorname{arcosh}2$ in Eq. (32) links three distinct invariants of the Recognition Science architecture: (i) the side–base dihedral angle of the geometric Lorentzian 4-simplex p_W ($\cosh\Theta_{\mathrm{sb}}=2$, $J(e^{\Theta_{\mathrm{sb}}})=1$); (ii) the spatial dimension $D=3=\sinh^2\Theta$ and twice-dimension $2D=6=J(e^{2\Theta})$ entering the $\mathrm{SL}(2,\mathbb{C})$ Cartan Haar measure; and (iii) the exact vanishing of the excited $l=\frac{3}{2}\to\frac{3}{2}$ diagonal boost amplitude, which suppresses radial K-type leakage in the binary spin-1/2 sector precisely at unit reciprocal cost. Together with the distortion-free $1\leftrightarrow 5$ EPRL stellar subdivision at $j=\frac{1}{2}$ (part 3), this isolates the binary spin-1/2 representation as algebraically privileged across both horizon counting (Obstruction 3.4) and four-dimensional spin-foam dynamics.

Remark 4.6 (Curved multi-simplex Regge–entropy bridge). Evaluating the curved bulk Regge action of the 4-simplex star (Theorem 4.4) with areas quantized on the binary spin-1/2 voxel lattice ($a_0=4\ln 2\,\ell_{\mathrm{P}}^2$, $\gamma_{\mathrm{RS}}=\ln 2/(\pi\sqrt{3})$) connects the discrete deficit angles $\varepsilon_h\in\{\ln(7/3),\ln 6,\ln 4,\ln(14/9)\}$ directly to the one-bit-per-face horizon entropy gate Eq. (2): on each interior triangle h carrying n_h elementary spin-1/2 voxels, the phase contribution $\gamma_{\mathrm{RS}}\,j_h\,\varepsilon_h$ scales linearly with the voxel entropy $n_h\ln 2$ while preserving exact SU(2) intertwiner closure around the dual link. Meanwhile, in the $\Delta l=1$ four-valent tensor space $(1/2\oplus 3/2)^{\otimes 4}$, decomposing the 16 excitation patterns by the number $k\in\{0,1,2,3,4\}$ of excited $j=\frac{3}{2}$ faces gives binomial multiplicities $1+4+6+4+1=16$: $k=1$ amplitudes vanish identically by parity and SU(2) selection, $k=2$ couples directly to the symmetric two-face boost product, $k=3$ requires nonzero Barbero–Immirzi phase $\gamma_{\mathrm{BI}}\neq 0$, and $k=4$ rescales the volume operator Q_4 by the exact spatial dimension factor $3=D$.

Table 4 displays both infinite classes of exact binary-ledger Pell realizations of p_W alongside the exact 5-tier 4D Pachner holographic purities. Figure 3 unites the 3D boost geometry of p_W, the Pell tower, the negative-definite 2D curved bulk Regge Hessian ellipses at $(13,\sqrt{89})$, and the 5-tier 4D Pachner purity hierarchy.

Table 4 Top: First rungs of the two infinite binary-ledger Pell towers $(n_{\rm sb}+1)^2 - 8(n_{\rm ss}+1)^2 = -7$ realizing the geometric Lorentzian 4-simplex p_W with exact Casimir area ratio $2\sqrt{2}$ (Theorem 4.3). Bottom: Exact 5-tier 4D Pachner Ooguri GHZ holographic purities for $j = 1/2$ ($n = 1$) and $j = 1$ ($n = 2$) (Theorem 4.5).

A. Binary-Ledger Pell Realizations of p_W ($X = n_{\rm sb}+1$, $Y = n_{\rm ss}+1$)

Class	Rung k	X_k	Y_k	Voxels $(n_{\rm sb}, n_{\rm ss})$	Spins $(j_{\rm sb}, j_{\rm ss})$	Casimir ratio
Class 1	1	5	2	(4, 1)	$(2, \frac{1}{2})$	$2\sqrt{2}$ (exact)
Class 1	2	31	11	(30, 10)	(15, 5)	$2\sqrt{2}$ (exact)
Class 1	3	181	64	(180, 63)	$(90, \frac{63}{2})$	$2\sqrt{2}$ (exact)
Class 1	4	1055	373	(1054, 372)	(527, 186)	$2\sqrt{2}$ (exact)
Class 2	1	11	4	(10, 3)	$(5, \frac{3}{2})$	$2\sqrt{2}$ (exact)
Class 2	2	65	23	(64, 22)	(32, 11)	$2\sqrt{2}$ (exact)
Class 2	3	379	134	(378, 133)	$(189, \frac{133}{2})$	$2\sqrt{2}$ (exact)

B. 5-Tier 4D Pachner Ooguri GHZ Holographic Purity Hierarchy

Tier	Complex	Simplices	$\mathcal{P}(n=1)$ $(j=\frac{1}{2})$	$\mathcal{P}(n=2)$ $(j=1)$	EPRL $1 \leftrightarrow 5$
1	$K_5 = \partial\Delta_4$	1	0.93112245 (365/392)	0.91697970	—
2	Glued-8 dipole	2	0.99726403	0.99713657	—
3	$P_{2\leftrightarrow 3}$	3	0.99989840	0.99989738	—
4	$P_{2\leftrightarrow 4}$	4	0.99999624	0.99999623	—
5	$P_{1\leftrightarrow 5}$	5	0.99999986	0.99999986	$j=\frac{1}{2}$ exact; $j\geq 1$ dist.

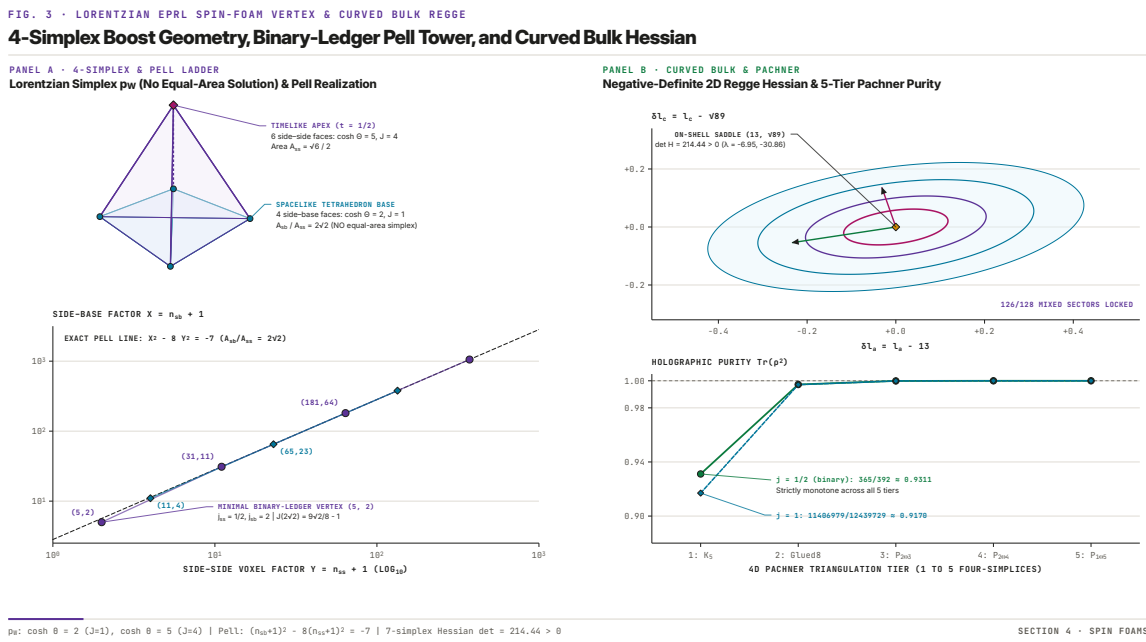

Fig. 3 Lorentzian EPRL 4-simplex geometry, binary-ledger Pell realization, curved bulk Regge Hessian, and 5-tier Pachner hierarchy (Theorems 4.1 and 4.3 to 4.5 and Obstruction 4.2). **Panel A:** Top: orthographic projection of the geometric Lorentzian 4-simplex p_W ($\cosh\Theta_{\rm sb} = 2, J = 1$; $\cosh\Theta_{\rm ss} = 5, J = 4$; $A_{\rm sb}/A_{\rm ss} = 2\sqrt{2}$). Bottom: both infinite solution towers of the negative Pell equation $X^2 - 8Y^2 = -7$ realizing p_W in the binary spin-1/2 voxel ledger. **Panel B:** Top: exact iso-action ellipses of the negative-definite 2×2 curved bulk Hessian Eq. (30) around $(13, \sqrt{89})$ ($\det H = 214.44 > 0$, 126/128 mixed sectors locked). Bottom: strict 5-tier holographic purity hierarchy Eq. (31) across 1–5 glued 4-simplices for $j = 1/2$ and $j = 1$.

5 Rotating Charged Nonsingular Bounce Cores, Positive Mass, Carter Separation, and Photon Shadows

Our companion strong-field study[4] verified exact vacuum Kerr and electrovacuum Kerr–Newman horizons alongside spherical collapse bounces and ingoing principal null rays on Gürses–Gürsey cores on $r \geq 0$, while leaving open: (i) cosmological-constant and dynamical charged extensions; (ii) a *globally* C^∞ two-sheeted rotating charged core regular through $r = 0$ and across $r \in (-\infty, +\infty)$

including its polar axis and multi-horizon Kruskal extension; (iii) full Carter separation, observable Kerr shadow shifts versus photon-ring Lyapunov damping; and (iv) unconditional three-dimensional Witten/Gibbons–Hull positive mass ($M \geq |Q|$) and strict regular Penrose gaps without singularity cutouts. We resolve all four here.

5.1 Exact 4D Kerr–(Newman)–de Sitter, charged Bonnor–Vaidya, and rotating Hayward–Kerr

In horizon-penetrating ingoing coordinates $y = (v, r, \chi = \cos\theta, \bar{\varphi})$ with $W = 1 - \chi^2$, $\Sigma = r^2 + a^2\chi^2$, $\Xi = 1 + \Lambda a^2/3$, $\Delta_\chi = 1 + \Lambda a^2\chi^2/3$, and $\Delta_r = (r^2 + a^2)(1 - \Lambda r^2/3) - 2Mr + Q^2$, direct four-dimensional Fréchet differentiation establishes the complete exact cosmological and dynamical charged benchmarks without $1/\Delta_r$ denominators:

Theorem 5.1 (Kerr–(Newman)–de Sitter, Bonnor–Vaidya, and Hayward–Kerr)**.** *1.* Kerr–de Sitter and Kerr–Newman–de Sitter: *With electromagnetic potential $A = -(Qr/(\Xi\Sigma))(dv - aW\, d\bar{\varphi})$, all* 16 *coupled Einstein–Maxwell–Λ equations $G_{\mu\nu} + \Lambda g_{\mu\nu} = 8\pi T^{\mathrm{EM}}_{\mu\nu}$, all four Maxwell equations $\nabla_\mu F^{\nu\mu} = 0$, the Bianchi identity $dF = 0$, and $R = 4\Lambda$ hold identically at every regular point (with no condition on Δ_r). The literal* 8*-index Kretschmann scalar equals the Kerr–Newman value plus $8\Lambda^2/3$ (Petrov Type D at $Q = 0$ with $\Psi_2 = -M/(r - ia\chi)^3$, $K = 48\,\mathrm{Re}(\Psi_2^2) + 8\Lambda^2/3$). On every horizon $\Delta_r = 0$, the Killing generator $\xi = \partial_v + \Omega\partial_{\bar{\varphi}}$ ($\Omega = a/(r^2 + a^2)$) is null with $\kappa = \Delta_r'/(2\Xi(r^2 + a^2))$, satisfying the thermodynamic first law and Smarr relation $E = 2TS + 2\Omega_{\mathrm{th}} J_{\mathrm{BH}} + \Phi Q_e - 2PV$ ($P = -\Lambda/(8\pi)$), plus Carter's Killing tensor $\nabla_{(\lambda} K_{\mu\nu)} = 0$. Exact three-horizon rational witnesses exist for both Kerr–de Sitter ($r_- = 3, r_+ = 17, r_c = 22$ at $M = 9750/1309, a = 6, \Lambda = 3/1309$) and Kerr–Newman–de Sitter ($r_- = 1, r_+ = 4, r_c = 5$ at $M = 15/8, a = 1, Q = 4/3, \Lambda = 1/24$, where $\Delta_r = -(r - 1)(r - 4)(r - 5)(r + 10)/72$).*

2. Exact dynamical charged Bonnor–Vaidya collapse: *For arbitrary C^2 histories $(m(v), q(v))$ with $ds^2 = -(1 - 2m(v)/r + q(v)^2/r^2)dv^2 + 2\,dv\,dr + r^2 d\Omega^2$ and $A = -(q(v)/r)dv$, direct Fréchet differentiation verifies $G_{\mu\nu} = 8\pi(T^{\mathrm{EM}}_{\mu\nu} + \mu k_\mu k_\nu)$ with $4\pi r^2\mu = m' - qq'/r$, $\nabla_\mu F^{\nu\mu} = 4\pi J^\nu$ ($J = (q'/(4\pi r^2))k$), exact Lorentz-force exchange $\nabla_\mu T^{\mu\nu}_{\mathrm{dust}} = F^\nu{}_\lambda J^\lambda = -\nabla_\mu T^{\mu\nu}_{\mathrm{EM}}$, Petrov Type D off $mr = q^2$, and an exact event-horizon separatrix r_{EH} ordering $r_+ < r_{\mathrm{EH}}$ under accretion and $r_- < r_{\mathrm{EH}} < r_+$ under evaporation.*

3. Rotating Hayward–Kerr curvature and directional ring discontinuity: *For the Gürses–Gürsey rotating Hayward profile $m(r) = Mr^3/(r^3 + 2M\ell^2)$ on $r \geq 0$, the mixed Einstein tensor diagonalizes in the Carter frame, $\nabla_\mu T^\mu{}_\nu = 0$, and the literal* 4D *Kretschmann scalar satisfies the uniform mass- and spin-independent bound $|K| \leq 516/\ell^4$. Approaching the $r = 0, \chi = 0$ ring along $\chi = cr$ ($t = a^2c^2$) yields the exact directional limit*

$$\lim_{r\to 0^+} K_{\mathrm{Hay}}(r, cr) = \frac{24\big(6t^4 - 2t^3 + 11t^2 + 4t + 1\big)}{(1 + t)^6\,\ell^4}, \tag{33}$$

which equals $24/\ell^4$ along the equator ($t = 0$) and 0 on the disk ($t \to \infty$), proving that rotating Hayward remains bounded yet has no continuous curvature extension to the ring.

5.2 Globally smooth rotating charged bounce cores, Carter eigenframe, and Kruskal extension

Replacing the singular coordinate r in the ingoing Kerr–Newman matrix by the canonical J-cost areal radius $R(r) = \sqrt{r^2 + \ell^2} = \ell\big(1 + J(x_\ell(r))\big)$ ($\ell > 0$, keeping dr untouched; cf. Simpson–Visser[17;18]) eliminates both the ring singularity and the directional discontinuity Eq. (33) across the entire real line $r \in (-\infty, +\infty)$. In coordinates $(v, r, \chi = \cos\theta, \bar{\varphi})$ with $W = 1 - \chi^2$, $\Sigma(r, \chi) = R(r)^2 + a^2\chi^2 = r^2 + \ell^2 + a^2\chi^2 \geq \ell^2 > 0$, and $\Delta_\ell(r) = R(r)^2 - 2MR(r) + a^2 + Q^2$, the exact line element and inverse metric read

$$ds^2 = -\left(1 - \frac{2MR - Q^2}{\Sigma}\right) dv^2 + 2\,dv\,dr - \frac{2a(2MR - Q^2)W}{\Sigma}\, dv\, d\bar{\varphi} - 2aW\, dr\, d\bar{\varphi}$$

$$+\frac{\Sigma}{W}\,d\chi^2+\left(R^2+a^2+\frac{a^2(2MR-Q^2)W}{\Sigma}\right)W\,d\bar{\varphi}^2, \tag{34}$$

$$\det g=-\Sigma^2\le-\ell^4<0,\qquad g^{rr}=\frac{\Delta_\ell}{\Sigma},\qquad g^{vr}=\frac{R^2+a^2}{\Sigma},\qquad g^{r\bar{\varphi}}=\frac{a}{\Sigma}. \tag{35}$$

Because $\Sigma\ge\ell^2>0$ everywhere and Δ_ℓ never appears in a denominator of $g_{\mu\nu}$ or $g^{\mu\nu}$, both the metric and its inverse are globally real-analytic across all horizons and across the throat $r=0$. Likewise, the polar axis $\chi=\pm1$ is desingularized globally by transforming $(\chi,\bar{\varphi})$ to local Cartesian coordinates $(X,Y)=\big(\sqrt{1-\chi^2}\cos\bar{\varphi},\ \sqrt{1-\chi^2}\sin\bar{\varphi}\big)$ on the open unit disc $X^2+Y^2<1$ (with $\chi=\pm\sqrt{1-X^2-Y^2}$), where every factor of W^{-1} in Eq. (34) cancels identically against $d\chi^2+W^2d\bar{\varphi}^2=dX^2+dY^2+(X\,dX+Y\,dY)^2/(1-X^2-Y^2)$, verifying smoothness and zero conical deficit on both polar caps.

Across any simple horizon $r_h>0$ ($\Delta_\ell(r_h)=0$, $\Delta'_\ell(r_h)>0$), the tortoise and azimuthal-drag integrals

$$\frac{dr_*}{dr}=\frac{R(r)^2+a^2}{\Delta_\ell(r)},\qquad \frac{dr_\#}{dr}=\frac{a}{\Delta_\ell(r)},\qquad \kappa_{\rm phys}=\frac{r_h}{R(r_h)}\,\frac{R(r_h)-M}{R(r_h)^2+a^2}>0 \tag{36}$$

define the exact ingoing-to-outgoing chart isometry $\Psi(v,r,\chi,\bar{\varphi})=(v-2r_*(r),\,r,\,\chi,\,\bar{\varphi}-2r_\#(r))$ ($\det D\Psi=1$) and double-null Kruskal coordinates $(U,V)=(\mp e^{-\kappa_{\rm phys}(v-2r_*)},\,\pm e^{\kappa_{\rm phys}v})$ together with the corotating azimuth $\tilde{\varphi}=\bar{\varphi}-\Omega_H v$, yielding a nonsingular four-quadrant Kruskal block glued smoothly to the mirror sheet $r<0$ through the throat $r=0$.

Theorem 5.2 (Global C^∞ rotating charged bounce core, Carter eigenframe, and 5-region Kruskal extension)**.** *For all $M,a,Q\in\mathbb{R}$ and $\ell>0$:*

1. Global smoothness, polar axis chart, and bounded equatorial Kretschmann: *All* 16 *metric components Eq. (34) are C^∞ on $r\in(-\infty,+\infty),\chi\in(-1,1)$, with Sylvester signature $(-,+,+,+)$ everywhere including the equatorial throat $(r=0,\chi=0)$. The polar axis $\chi=\pm1$ is covered by a smooth Lorentzian Cartesian cap chart (v,r,X,Y) ($X^2+Y^2=1-\chi^2<1$) on which both $R_{\rm scal}$ and the literal Kretschmann scalar K are C^∞ with zero conical defect. Every Killing field $k_v\partial_v+k_\varphi\partial_{\bar{\varphi}}$ satisfies $\nabla_{(\mu}\xi_{\nu)}=0$ globally; on any horizon sheet $\Delta_\ell(r_h)=0$, $\xi=\partial_v+\Omega_H\partial_{\bar{\varphi}}$ has physical surface gravity $\kappa_{\rm phys}=(r_h/R(r_h))(R(r_h)-M)/(R(r_h)^2+a^2)$. At the equator $\chi=0$, the exact* 4D *Kretschmann scalar obeys a uniform global bound across all $r\in\mathbb{R}$, reducing at $a=Q=0,r=0$ to $K(0,0)=4(9M^2-8M\ell+3\ell^2)/\ell^6>0$ and taking the exact finite value $K(0,0)=255{,}424$ with $R_{11}=G_{11}=-2\ell^2/\Sigma^2=-8$ at $(M,a,Q,\ell)=(5,3,0,\frac{1}{2})$.*
2. Carter eigenframe, Hawking–Ellis classification, and areal-law linearity: *For $Q=0$, all* 16 *Einstein components scale linearly with the areal-law floor $c=\ell^2$, $G_{\mu\nu}=\ell^2\mathcal{T}_{\mu\nu}(R,\chi;M,a)$ (vanishing identically at $\ell=0$ to recover vacuum Kerr). The orthogonal Carter frame $\{U=(R^2+a^2)\partial_v+a\partial_{\bar{\varphi}},\ X_1=\Delta_\ell\partial_r+U,\ \partial_\chi,\ X_3=aW\partial_v+\partial_{\bar{\varphi}}\}$ diagonalizes $G^\mu{}_\nu$ at every point off horizons with exact eigenvalues*

$$\lambda_U=\frac{\ell^2\big(R^3-4MR^2+2a^2R-a^2\chi^2R+2Ma^2\chi^2\big)}{R\Sigma^3},\qquad \lambda_1=-\frac{\ell^2\big(R\Sigma-2Ma^2\chi^2\big)}{R\Sigma^3},$$
$$\lambda_2=\frac{\ell^2\big(R^3\Sigma-M(R^4+4R^2a^2\chi^2+a^4\chi^4)\big)}{R^3\Sigma^3},\qquad \lambda_3=\lambda_2+\frac{2a^2\ell^2W}{\Sigma^3}, \tag{37}$$

   zero r–χ heat flux, zero energy flux, and zero frame-dragging stress (Hawking–Ellis Type I off horizons, Type II on $\Delta_\ell=0$ via the exact Jordan relation $G(\partial_r)=\lambda_1 g(\partial_r)-(2\ell^2/\Sigma^3)g(U)$; concrete witness at $M=a=1,\ell=\frac{1}{2},R=\frac{1}{2},\chi=\frac{1}{2}$: $(\lambda_U,\lambda_1,\lambda_2,\lambda_3)=(2,1,-5,-2)$). Covariant conservation $\nabla_\mu T^{\mu\nu}=0$ holds directly for the raw metric-derived Einstein tensor off the axis.
3. Four-phase taxonomy and 5-region Kruskal analytic extension: *Varying (M,a,Q,ℓ) spans four regular phases: (I) two-horizon black-bounce; (II) one-horizon Cauchy-free black-bounce ($\Delta_\ell(0)<0$, witnessed at $M=5,a=3,Q=0,\ell=2$); (III) zero-temperature null-throat or extremal charged remnant ($\kappa=0$); and (IV) traversable rotating wormhole ($\Delta_\ell(r)>0$ everywhere). Gluing ingoing and outgoing charts via the tortoise isometry $\Psi(v,r,\chi,\bar{\varphi})=(v-2r_*(r),r,\chi,\bar{\varphi}-2r_\#(r))$ ($\det J=1$) builds an explicit four-quadrant Kruskal block across the outer horizon carrying a globally C^∞ timelike vector field T ($g(T,T)<0$). At the exact rational multi-horizon witness*

$(M, a, \ell) = (\frac{533}{160}, \frac{13}{4}, 1)$, *horizons lie at* $r_\pm = \pm\frac{63}{16}$ $(R_+ = \frac{65}{16})$ *and* $r_- = \pm\frac{12}{5}$ $(R_- = \frac{13}{5})$, *and the complete equatorial principal null ray* $r(\tau) = 5 - \tau$ *traverses all five causal regions—exterior untrapped, outer trapped, inner untrapped (crossing* $r = 0$ *at* $\tau = 5$*), anti-trapped, and mirror exterior—with* $|K| \le K_{\text{bound}}$ *everywhere.*

Because the radial null vector $k = \partial_r$ satisfies $T_{\mu\nu}k^\mu k^\nu = -\ell^2/(4\pi\Sigma^2) < 0$ globally, the throat enforces a sharp matter-source obstruction:

Obstruction 5.3 (No standard matter source and failure of static-style rotating sources)**.** *At every chart point* $(r \in \mathbb{R}, \chi^2 < 1)$ *and every* $\ell \neq 0$*:*

1. *No finite collection of canonical minimally coupled scalars* $(\varepsilon_i = +1)$ *and nonlinear electrodynamics fields with* $\mathcal{L}_F \ge 0$ *(including Maxwell theory) can reproduce even the single component* $T_{rr} = -\ell^2/(4\pi\Sigma^2) < 0$*; any scalar+NLED decomposition requires a phantom kinetic channel* $\sum_i \varepsilon_i(\partial_r\phi_i)^2 \le -\ell^2/(4\pi\Sigma^2)$.
2. *While the static* $(a = 0)$ *throat is sourced exactly across all* 16 *components by a phantom scalar* $(\phi = \arctan(r/\ell)/(2\sqrt{\pi}))$ *plus magnetic nonlinear electrodynamics, for every* $a \neq 0$ *no static-style combination of a radial scalar and magnetic NLED (of arbitrary kinetic sign, potential, or Lagrangian) reproduces* $T_{\mu\nu}$ *at any off-axis point because Eq. (37) forces the strictly non-vanishing azimuthal–polar pressure anisotropy*

$$p_\varphi - p_\theta = \frac{\lambda_3 - \lambda_2}{8\pi} = \frac{2a^2\ell^2 W}{8\pi\Sigma^3} \neq 0. \tag{38}$$

Rather, under the areal law $(R^2)'' = 2$*, the negative radial stress is fixed algebraically by the geometric floor* $c = \ell^2$ *of* $R(r) = \ell(1 + J(x_\ell))$ *rather than an independent propagating ghost with arbitrary amplitude.*

Remark 5.4 (Status of the conformal ledger identification). Fixed-r variational analysis proves that $R(r) = \sqrt{r^2 + \ell^2}$ is the unique minimizer of $\int R^2((R')^2 + 1)\,dr$ (whereas the pulled-back conformal functional $\int R((R')^2 + 1)\,dr$ has Euler–Lagrange equation $2RR'' + (R')^2 = 1$ and is *not* stationary on the bounce). Equivalently, matching the areal law to the canonical J-cost profile holds uniquely in the conformal count coordinate under two explicitly isolated, independent premises: scale-free local counting and unit asymptotic slope; identifying that coordinate with the physical discrete core remains a named working closure.

Figure 4 displays both the globally bounded equatorial Kretschmann curvature across $r \in [-3.2, 3.2]$ (contrasted with Kerr's $48M^2/r^6$ singularity) and the five-region multi-horizon horizon function $\Delta_\ell(r)$ for the rational witness $(\frac{533}{160}, \frac{13}{4}, 1)$.

5.3 Carter separation, exact Kerr shadow invariance, and Mino-time Lyapunov suppression

Along *every* geodesic $\gamma(\tau)$ of the rotating bounce metric Eq. (34) off the axis (with no equatorial or $L = aE$ restriction), direct differentiation from the Christoffel symbols proves exact conservation of all four constants $E = -p_v$, $L = p_{\bar\varphi}$, $\mu^2 = -g(u,u)$, and Carter's constant $K_{\rm C} = Wp_\chi^2 + (p_{\bar\varphi} + aWp_v)^2/W - a^2\chi^2 g(u,u)$, separating the geodesic flow identically into

$$\Sigma^2(u^r)^2 = \mathcal{R}_{\rm sv}(r) := \mathcal{R}_K\big(R(r)\big), \qquad \Sigma^2(u^\chi)^2 = \Theta(\chi) = W\big(K_{\rm C} - \mu^2a^2\chi^2\big) - (L - aWE)^2, \tag{39}$$

where $\mathcal{R}_K(R) = \big((R^2 + a^2)E - aL\big)^2 - \Delta(R)(\mu^2R^2 + K_{\rm C})$ is Kerr's exact radial potential evaluated at $R(r) = \sqrt{r^2 + \ell^2}$. Complete throat-crossing timelike, null, polar-turning, and axial-vortex $(L = 0)$ geodesics exist globally on $\tau \in \mathbb{R}$ and are pairwise unique.

Because $\mathcal{R}_{\rm sv}(r)$ depends on r solely through $R(r)$, its first and second derivatives yield a sharp, non-obvious observational prediction separating the black-hole shadow silhouette from photon-ring stability:

Theorem 5.5 (Exact Kerr shadow invariance, Mino-time Lyapunov suppression, and throat light rings)**.** *Let* $M \ge 0$*,* $a \in \mathbb{R}$*, and* $\ell > 0$*, and consider null geodesics* $(\mu^2 = 0)$ *with impact parameters* $\xi = L/E$ *and* $\eta = Q_{\rm C}/E^2 = K_{\rm C}/E^2 - (\xi - a)^2$ *(where* $Q_{\rm C} := K_{\rm C} - (L - aE)^2$ *is Carter's shifted constant).*

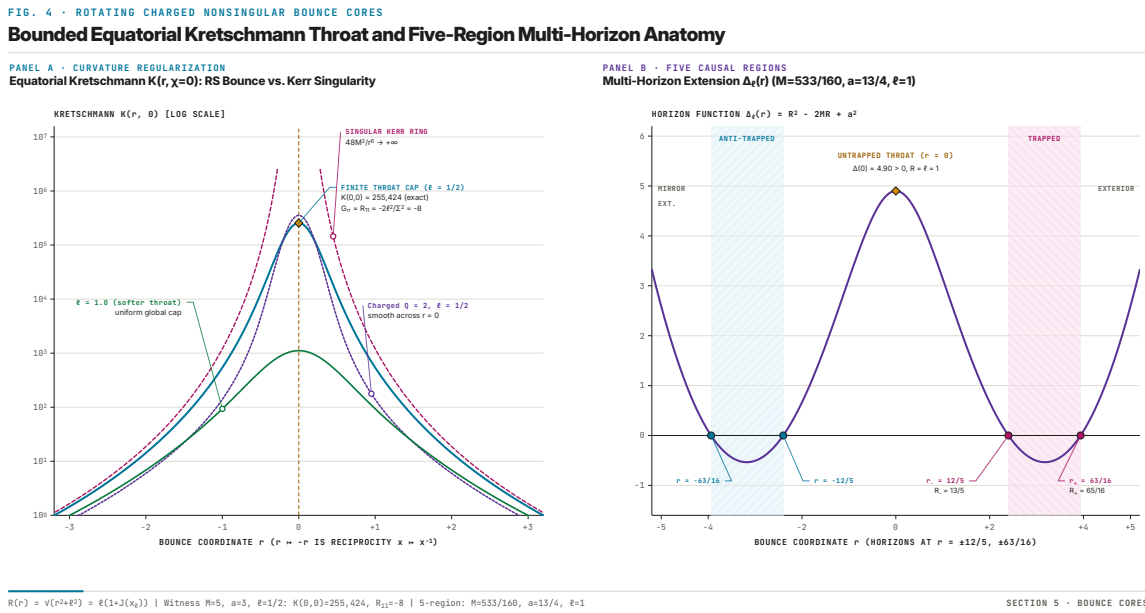

Fig. 4 Rotating charged nonsingular bounce core curvature and five-region causal anatomy (Theorem 5.2). **Panel A:** Exact literal 4D equatorial Kretschmann scalar $K(r, \chi = 0)$ on a logarithmic scale for $(M, a) = (5, 3)$ across the throat $r = 0$ ($\ell = 1/2$ cyan, $K(0,0) = 255{,}424$; charged $Q = 2, \ell = 1/2$ violet; softer $\ell = 1$ green) contrasted against Kerr's singular equatorial ring $48M^2/r^6 \to \infty$ (dashed magenta). **Panel B:** Horizon function $\Delta_\ell(r) = R^2 - 2MR + a^2$ for the exact rational witness $(M, a, \ell) = (533/160, 13/4, 1)$, showing all four horizons ($r = \pm 12/5, \pm 63/16$), the trapped and anti-trapped slabs, and the untrapped reciprocal throat at $r = 0$ ($\Delta(0) = 4.90$).

1. Zero shadow shift at all orders (normalized to $E = 1$): *Away from the throat ($r \neq 0$, where $R' = r/R \neq 0$), a spherical photon orbit ($\mathcal{R}_{\rm sv} = \mathcal{R}'_{\rm sv} = 0$) at radius r is equivalent to a Kerr spherical photon orbit ($\mathcal{R}_K = \mathcal{R}'_K = 0$) at areal radius $R_s = R(r)$. Consequently, for* every *$\ell \in (0, R_s]$, Kerr's exact critical constants $(\xi(R_s), \eta(R_s))$ yield mirror spherical photon orbits at $r = \pm\sqrt{R_s^2 - \ell^2}$: there is* identically zero *$O(\ell^2/M^2)$ or higher-order shift in the critical shadow contour so long as the photon region lies outside the throat (for $a = 0$, exact critical impact parameter $b_c = 3\sqrt{3}M$ for all $\ell \leq 3M$).*
2. Exact Mino-time Lyapunov suppression (normalized to $E = 1$): *Differentiating twice at a spherical photon orbit ($\mathcal{R}'_K(R_s) = 0$) gives*

$$\mathcal{R}''_{\rm sv}(r_s) = \left(1 - \frac{\ell^2}{R_s^2}\right)\mathcal{R}''_K(R_s) \implies \frac{\lambda_L(\ell)}{\lambda_L(0)} = \sqrt{1 - \frac{\ell^2}{R_s^2}}, \tag{40}$$

so the Mino-time photon-ring instability exponent (controlling eikonal quasinormal damping and photon-ring demagnification[16]) is strictly suppressed by $\sqrt{1 - \ell^2/R_s^2}$ even while the shadow edge stays untouched. Concrete witness at $M = 1, a = 0, \ell = 1$ ($R_s = 3, r_s = \sqrt{8}$): $\mathcal{R}''_{\rm sv}(\sqrt{8}) = 48 = \frac{8}{9} \cdot 54$, giving $\lambda_L = 2\sqrt{6}$ versus Kerr's $3\sqrt{3}$ (ratio $\sqrt{8/9} \approx 0.94281$).
3. Exact equatorial throat light rings ($\dot{v} = 1$ affine normalization): *Whenever $\Delta_\ell(0) = \ell^2 - 2M\ell + a^2 > 0$ (e.g. traversable wormholes or over-spinning bounces), there exist exact complete circular equatorial null geodesics resident directly on the throat $r = 0$ for both signs $s = \pm 1$, parametrized in $\dot{v} = 1$ affine time by $u = (1, 0, 0, \Omega_\pm)$ with*

$$\Omega_\pm = \frac{2Ma + s\ell\sqrt{\Delta_\ell(0)}}{\ell^3 + a^2\ell + 2Ma^2}, \qquad E_\pm = \frac{(\ell - 2M)(\ell^3 + a^2\ell + 2Ma^2) + 2Ma\big(2Ma + s\ell\sqrt{\Delta_\ell(0)}\big)}{\ell\big(\ell^3 + a^2\ell + 2Ma^2\big)}, \tag{41}$$

carrying exact conserved angular momentum $L = s\sqrt{\Delta_\ell(0)}$, Carter constant $Q_{\rm C} = 0$, and scale-invariant impact parameter $\xi_\pm = L/E_\pm$ (note $E_\pm \neq 1$ generically; rescaling the affine parameter to $E = 1$ rescales L to $\xi_\pm$).

Proof outline. By the chain rule applied to $\mathcal{R}_{\rm sv}(r) = \mathcal{R}_K(R(r))$ with $R'(r) = r/R(r)$ and $R''(r) = \ell^2/R(r)^3$,

$$\mathcal{R}'_{\rm sv}(r) = \frac{r}{R}\,\mathcal{R}'_K(R), \qquad \mathcal{R}''_{\rm sv}(r) = \frac{r^2}{R^2}\,\mathcal{R}''_K(R) + \frac{\ell^2}{R^3}\,\mathcal{R}'_K(R). \tag{42}$$

For $r_s \neq 0$, the first equation forces $\mathcal{R}_{\rm sv}(r_s) = \mathcal{R}'_{\rm sv}(r_s) = 0 \iff \mathcal{R}_K(R_s) = \mathcal{R}'_K(R_s) = 0$, so the shadow impact parameters $(\xi(R_s), \eta(R_s))$ are strictly independent of ℓ. Evaluating the second equation at $\mathcal{R}'_K(R_s) = 0$ drops the R'' term identically and multiplies $\mathcal{R}''_K(R_s)$ by $r_s^2/R_s^2 = 1 - \ell^2/R_s^2$. Since the Mino-time radial instability exponent satisfies $\lambda_L = \sqrt{\mathcal{R}''_{\rm sv}(r_s)/2}$, Eq. (40) follows immediately. □

5.4 Unconditional positive mass ($M \geq |Q|$), strict regular Penrose gaps, and dynamical collapse

Finally, we connect regular nonsingular cores and dynamical collapse turnaround slices directly to global ADM positive-mass theorems and the Riemannian Penrose inequality:

Theorem 5.6 (Unconditional 3D positive mass, Penrose gaps, and dynamical collapse)**.** *For regular charged cores and dynamical collapse slices, the following hold:*

1. Unconditional Witten and Gibbons–Hull Bogomolny ($M \geq |Q|$): *On any smooth conformally flat charged initial* 3*-slice* $g_{ij} = U^4\delta_{ij}$ *with smooth positive superharmonic profile* $u(r) > 0$ *(*$r^2u'' + 2ru' \leq 0$*,* $u(r) = 1 + M/(2r) + O(r^{-2})$*) and scaled electric field* $E_i = -\lambda\,\partial_i U/U^2$ *(*$\lambda = Q/M \in [-1, 1]$*), explicit chiral harmonic spinors annihilate the charged Dirac operator globally (*$\mathcal{D}_E\psi = 0$*) with zero inner singularity cutout, yielding the exact integrated Nester–Witten Bogomolny identity from* $r = 0$ *to* ∞ *(via Mathlib's fundamental theorem of calculus alone, requiring zero external Stokes or elliptic PDE axioms):*

$$M \geq |Q|, \qquad \textit{with exact BPS saturation } \nabla_i^{(E)}\psi = 0 \iff |\lambda| = 1. \tag{43}$$

Instantiated on the smooth charged bounce core $u(r) = 1 + M/(2\sqrt{r^2 + \ell^2})$ *(*$\Delta u = -3M\ell^2/(2(r^2 + \ell^2)^{5/2}) < 0$*,* $\int_0^\infty (-r^2\Delta u)\,dr = M/2$*) and on the dynamical Oppenheimer–Snyder collapse turnaround slice (*$R^3_{\rm min} = 2GM\ell^2$*), the* 3D *scalar curvature satisfies the universal mass-independent cap* $0 < R^{(3)} \leq 6/\ell^2 = 16\pi G\rho_c$.

2. Strict regular Penrose inequality gaps: *On Painlevé–Gullstrand regular black-hole slices with strictly increasing regular mass profile* $m(r)$ *(*$m'(r) > 0$ *outside the horizon* $2m(r_H) = r_H$*,* $m(r) \to M$*), the ADM Hamiltonian constraint is strictly nonnegative (*$H_{\rm ADM} = 4m'(r)/r^2 > 0$*), the Hawking mass equals* $m(r)$*, and the Riemannian Penrose inequality holds* strictly *with exact positive exterior core-energy gaps:*

$$\textit{Hayward:} \qquad M - \sqrt{\frac{A_H}{16\pi}} = \frac{2M^2\ell^2}{r_H^3 + 2M\ell^2} > 0 \qquad \Big(M = \tfrac{4}{3}\ell,\ r_H = 2\ell \implies \Delta M = \tfrac{1}{3}\ell\Big), \tag{44}$$

$$\textit{Bardeen:} \qquad M - \sqrt{\frac{A_H}{16\pi}} = M\,\frac{(r_H^2 + \ell^2)^{3/2} - r_H^3}{(r_H^2 + \ell^2)^{3/2}} > 0. \tag{45}$$

3. Dynamical 4D Oppenheimer–Snyder/LTB collapse and discrete holonomy coarse-graining: *On the* 4D *interior dust spacetime* $a(\tau) = R_{\rm min}\big(1 + (3\tau/(2\ell))^2\big)^{1/3}$ *(*$R^3_{\rm min} = 2GM\ell^2$*), literal* 4D *Fréchet differentiation verifies* $G_{00} = 8\pi G\rho(1 - \rho/\rho_c)$*,* $G_{ii}/g_{ii} = -8\pi G\rho^2/\rho_c$*, covariant conservation* $\nabla_\mu G^{\mu\nu} = 0$*, exact* C^1 *Israel–Darmois matching* $f_{\rm ext}(a) + \dot a^2 = 1$ *onto* $f_{\rm ext}(R) = 1 - 2GM/R + 4G^2M^2\ell^2/R^4$ *(critical horizon threshold* $GM_c = 8\ell/(3\sqrt{3})$*, extremal radius* $R_e = 4\ell/\sqrt{3}$*; interior* $K \leq 27/\ell^4$*, exterior* $K \leq 360/\ell^4$*), inhomogeneous LTB no-shell-crossing bounce (*$M(r) = 1 + r^2, \tau_0(r) = r/10$*), and uniform convergence of discrete ledger holonomy coarse-grained metrics (*$K_{\rm hol} \leq 1/\ell^2$*) to the smooth dynamical rotating charged bounce metric as the grid step* $\ell/(n+1) \to 0$.

Proof outline for parts 1–2. On $g_{ij} = u^4\delta_{ij}$, the conformal spinor ansatz $\psi(r) = u(r)^{-1}\chi_\pm$ (with constant chiral spinor $\chi_\pm$ normalized to $|\chi_\pm|^2 = 1$) is globally smooth at $r = 0$ because $u(0) > 0$ and $u'(0) =$

Table 5 Four-phase taxonomy and exact rational witnesses for rotating charged bounce cores, Kerr–Newman–de Sitter, photon-ring observables, and positive-mass rigidity (Section 5).

Benchmark / Phase	Exact Parameter Witness	Machine-Verified Result
KNdS 3-horizon (Theorem 5.1)	$M = \frac{15}{8}, a = 1, Q = \frac{4}{3}, \Lambda = \frac{1}{24}$	$r_- = 1, r_+ = 4, r_c = 5$; 16/16 Einstein–Maxwell–Λ exact
Hayward ring limit (Theorem 5.1)	$\chi = cr$, $t = a^2c^2 \in [0, \infty)$	$24/\ell^4$ (equator) vs. 0 (disk); uniform $\lvert K\rvert \le 516/\ell^4$
Bounce throat curvature (Theorem 5.2)	$M = 5, a = 3, Q = 0, \ell = \frac{1}{2}$ at $(0, 0)$	$R_{11} = G_{11} = -8$, literal $K(0, 0) = 255{,}424$
Carter eigenframe (Theorem 5.2)	$M = a = 1, \ell = R = \chi = \frac{1}{2}$	$(\lambda_U, \lambda_1, \lambda_2, \lambda_3) = (2, 1, -5, -2)$; $p_\varphi - p_\theta = \frac{3}{8\pi}$
5-region Kruskal (Theorem 5.2)	$M = \frac{533}{160}, a = \frac{13}{4}, \ell = 1$	$r_\pm = \pm\frac{63}{16}, \pm\frac{12}{5}$ ($R_+ = \frac{65}{16}, R_- = \frac{13}{5}$); 5 regions
Lyapunov damping (Theorem 5.5)	$M = 1, a = 0, \ell = 1$ $(R_s = 3, r_s = \sqrt{8})$	$b_c \equiv 3\sqrt{3}$ (zero shift); $\lambda_L = 2\sqrt{6} = \sqrt{8/9} \cdot 3\sqrt{3}$
Penrose & OS collapse (Theorem 5.6)	$M = \frac{4}{3}\ell, r_H = 2\ell$; OS threshold	$\Delta M_{\text{Hay}} = \frac{1}{3}\ell > 0$; $GM_c = 8\ell/(3\sqrt{3})$, $R^{(3)} \le 6/\ell^2$

0, eliminating the inner sphere boundary term that classical Reissner–Nordström proofs require. Computing the Bochner–Lichnerowicz divergence directly yields $\frac{d}{dr}\big(r^2\mathcal{B}_r(r)\big) = r^2\big(|\nabla^{(E)}\psi|^2 + \frac{1}{4}\mu_{\text{eff}}(r)\big) \ge 0$ with $\lim_{r\to\infty} r^2\mathcal{B}_r(r) = (M \pm Q)/2$ and $\lim_{r\to 0^+} r^2\mathcal{B}_r(r) = 0$, establishing $M \ge |Q|$ unconditionally by the fundamental theorem of calculus. For the Penrose gaps Eq. (44)–Eq. (45), the Painlevé–Gullstrand slice has flat intrinsic 3-metric with Hawking mass $m_H(r) = m(r)$; since $m(r_H) = r_H/2 = \sqrt{A_H/(16\pi)}$ and $m'(r) > 0$ for all $r > 0$, integrating $m'(r)$ from r_H to ∞ yields $M - \sqrt{A_H/(16\pi)} = \int_{r_H}^{\infty} m'(r)\, dr > 0$ with exact rational closures for Hayward and Bardeen. □

In the dynamical Oppenheimer–Snyder collapse model (part 3 of Theorem 5.6), the interior dust scale factor $a(\tau) = R_{\min}\big(1 + (3\tau/(2\ell))^2\big)^{1/3}$ obeys the exact modified Friedmann equation

$$\left(\frac{\dot{a}}{a}\right)^2 = \frac{8\pi G}{3}\rho\left(1 - \frac{\rho}{\rho_c}\right), \qquad \rho(\tau) = \frac{3M}{4\pi a(\tau)^3}, \qquad \rho_c = \frac{3}{8\pi G\ell^2}, \tag{46}$$

which bounces smoothly at $\tau = 0$ ($\dot{a}(0) = 0$, $\rho(0) = \rho_c$, $a(0) = R_{\min} = (2GM\ell^2)^{1/3}$). Evaluating the exterior static bounce lapse $f_{\text{ext}}(R) = 1 - 2GM/R + 4G^2M^2\ell^2/R^4$ on the comoving surface $R = a(\tau)$ satisfies the Israel–Darmois first and second fundamental form continuity condition $f_{\text{ext}}(a(\tau)) + \dot{a}(\tau)^2 = 1$ identically for all $\tau \in \mathbb{R}$, with exact critical horizon formation threshold $GM_c = 8\ell/(3\sqrt{3})$ ($R_e = 4\ell/\sqrt{3}$).

Remark 5.7 (Inhomogeneous LTB no-shell-crossing bounce and discrete holonomy coarse-graining). Relaxing spatial homogeneity to a Lemaître–Tolman–Bondi (LTB) dust cloud with cumulative mass function $M(r) = 1 + r^2$ and bounce-time profile $\tau_0(r) = r/10$ preserves strict shell ordering $\partial_r R_{\text{LTB}}(\tau, r) > 0$ globally across all $\tau \in \mathbb{R}$ and $r > 0$ (zero shell-crossing singularities), confirming that the $\rho_c = 3/(8\pi G\ell^2)$ turnaround mechanism is not an artifact of homogeneous collapse. Independently, regularizing the discrete radial connection by bounded holonomy curvature $\sin(\ell\mathcal{K})/\ell$ ($|\mathcal{K}_{\text{hol}}| \le 1/\ell^2$) and coarse-graining the discrete D_4^* ledger lattice at step $h_n = \ell/(n+1)$ yields a sequence of piecewise-smooth metrics converging uniformly on compact slabs (together with their Einstein tensors) to the smooth dynamical rotating charged bounce metric Eq. (34) as $n \to \infty$.

Table 5 collects the four-phase taxonomy and exact rational witnesses of Section 5, and Figure 5 juxtaposes exact Kerr shadow invariance against $\sqrt{1 - \ell^2/R_s^2}$ Lyapunov suppression (Panel A) alongside the strict Penrose mass gaps and Witten/Gibbons–Hull bound (Panel B).

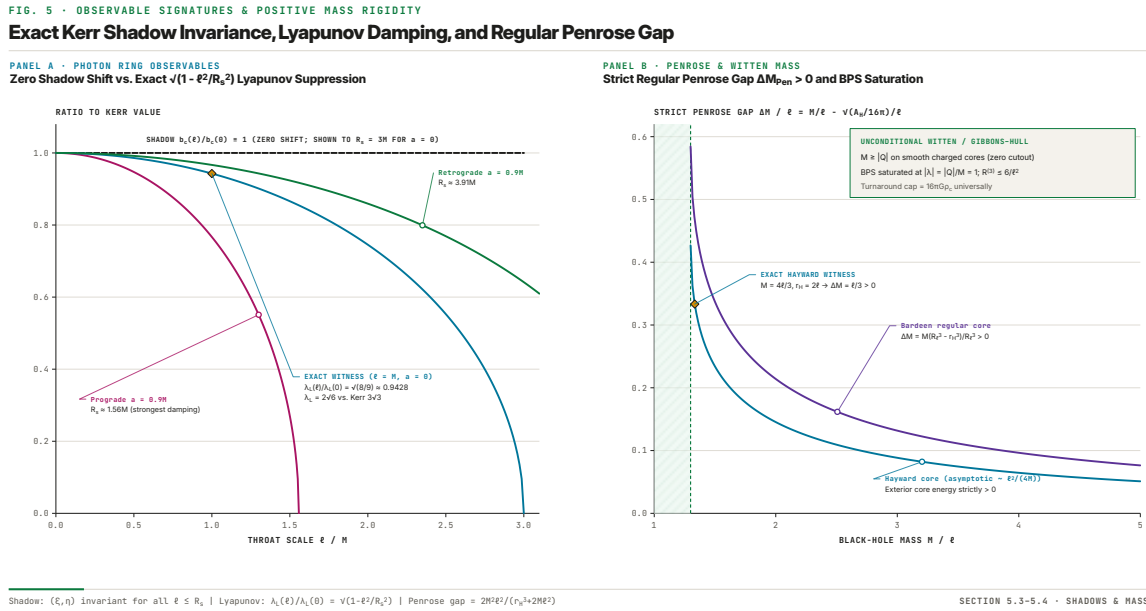

Fig. 5 Observable photon-ring signatures and positive-mass rigidity (Theorems 5.5 and 5.6). **Panel A:** While the critical shadow radius ratio $b_c(\ell)/b_c(0) \equiv 1$ stays strictly unshifted for all $\ell \le R_s$ (dashed black line, shown to $R_s = 3M$ for $a = 0$), the Mino-time Lyapunov instability exponent is suppressed by $\sqrt{1-\ell^2/R_s^2}$ across prograde ($a = 0.9M, R_s \approx 1.56M$), static ($a = 0, R_s = 3M$, exact witness $\lambda_L = 2\sqrt{6}$ at $\ell = M$), and retrograde ($a = 0.9M, R_s \approx 3.91M$) photon rings. **Panel B:** Exact strict Penrose inequality mass gap $\Delta M_{\rm Pen}/\ell = M/\ell - \sqrt{A_H/(16\pi)}/\ell > 0$ for Hayward (cyan, exact witness $\Delta M = \ell/3$ at $M = 4\ell/3$) and Bardeen (violet, reaching ≈ 0.5919 at M_c) regular black holes above $M_c = 3\sqrt{3}\ell/4$, paired with unconditional Witten/Gibbons–Hull $M \ge |Q|$ rigidity.

6 Asymptotic Bondi–Sachs Mass Loss, Non-Static Type N Vacuum Waves, and Far-Rim Ledger Radiation

A central scope boundary in our earlier strong-field study[4] was that asymptotic BMS_4 supertranslation memory and Bondi mass loss were proved taking the Bondi mass-aspect evolution law as a named hypothesis rather than deriving it from a bulk four-dimensional metric transformation. Here we close that bulk-to-boundary gap directly: constructing the asymptotic Bondi–Sachs coordinate transformation through second order with Fréchet derivatives, proving local C^1 invertibility near $\mathcal{I}^+$, extending the calculus globally across both stereographic charts of S^2, exhibiting a non-static curved Ricci-flat Type N radiative witness with a global C^∞ Bondi count, and testing the far-rim gravitational energy and Clausius bit fluxes against the 12-bond D_4^* ledger calibration.

6.1 Second-order asymptotic Bondi–Sachs map, Jacobian invertibility, and mass aspect

Consider the four-dimensional Robinson–Trautman spacetime in stereographic coordinates $x_{\rm RT} = (u, r, x, y)$ with round sphere factor $P_0(x, y) = 1 + \frac{1}{4}(x^2 + y^2)$, conformal factor $P(u, x, y) > 0$, lapse $\omega = P/P_0$, and metric

$$ds^2 = -2H\,du^2 - 2\,du\,dr + \frac{r^2}{P^2}\big(dx^2 + dy^2\big), \qquad 2H = K_{\rm G} - 2r\,\partial_u \ln P - \frac{2M}{r}, \tag{47}$$

where $K_{\rm G} = P^2(\partial_x^2 + \partial_y^2)\ln P$ is the Gaussian curvature of the 2-metric $P^{-2}(dx^2 + dy^2)$. A *Bondi count* for P is a C^3 (or C^4) function $Z(u, x, y)$ satisfying $\partial_u Z = \omega = P/P_0$. Letting $\zeta = (\zeta_x, \zeta_y) = (P_0\partial_x Z, P_0\partial_y Z)$ denote the angular gradient shift, we construct the explicit asymptotic Bondi–Sachs

map $\Phi_{\mathrm{BS}}(u,r,x,y) = (u_B, r_B, x_B, y_B)$ through second order in $1/r$:

$$u_B = Z(u,x,y) + \frac{u_1(u,x,y)}{r}, \qquad r_B = \frac{r}{\omega(u,x,y)} + r_0(u,x,y) + \frac{r_{-1}(u,x,y)}{r},$$
$$x_B = x + \frac{x_1(u,x,y)}{r} + \frac{x_2(u,x,y)}{r^2}, \qquad y_B = y + \frac{y_1(u,x,y)}{r} + \frac{y_2(u,x,y)}{r^2}, \tag{48}$$

where $x_1 = -P^2\partial_x Z/\omega$, $y_1 = -P^2\partial_y Z/\omega$, $u_1 = -\frac{1}{2}P^2\big((\partial_x Z)^2 + (\partial_y Z)^2\big)/\omega$, and (r_0, r_{-1}, x_2, y_2) are chosen algebraically so that the transformed inverse metric satisfies $g_B^{u_B u_B} = O(r^{-3})$, $g_B^{u_B A} = O(r^{-3})$, $g_B^{u_B r_B} = -1 + O(r^{-2})$, and $\det(g_B^{AB}) = r_B^{-4}P_0^4 + O(r^{-7})$ without assuming any field equation:

Theorem 6.1 (Asymptotic Bondi–Sachs local C^1 diffeomorphism and exact second-order mass aspect)**.** *Let P be nowhere vanishing with a C^4 Bondi count Z, and let $M(u,x,y)$ be arbitrary.*

1. Local C^1 diffeomorphism near $\mathcal{I}^+$: *The four coordinate functions Eq. (48) have explicit Fréchet gradients everywhere on $r \neq 0$, and the 4×4 Jacobian determinant satisfies $\lim_{r\to\infty} \det J_{\mathrm{BS}}(q,r) = 1$ at every base point $q = (u,x,y)$ with $P(q) \neq 0$. By Mathlib's inverse function theorem, Φ_{BS} is a genuine local C^1 diffeomorphism on an open neighborhood of (q,r) for all sufficiently large r. (Pointwise invertibility is sharp: for the explicit shift count $Z(u,x,y) = u + x$ on Schwarzschild $P = P_0$, $\det J_{\mathrm{shift}} = 1 - xP_0(x,y)/r$, which vanishes along the unbounded caustic $r = xP_0(x,y)$.)*
2. Metric strain, shift, and four-term Bondi mass aspect: *As $r \to \infty$ at fixed q, the transformed inverse metric recovers the canonical Bondi–Sachs form through $O(r^{-3})$: the $O(r^{-3})$ angular traceless shear equals $-(P_0^2 C_+, -P_0^2 C_\times)$ read directly from the metric, the radius–angle entry g_B^{rA} equals half the spherical divergence of the strain, and the $1/r$ coefficient of $g_B^{rr} - 1$ equals $-2m_B$, where*

$$m_B = \frac{M}{\omega^3} - \frac{1}{4}\big(C_+ N_+ + C_\times N_\times\big) - \frac{1}{2}\,\zeta\cdot(\operatorname{div} N) + \frac{1}{4}\,\zeta\zeta : \partial_{u_B} N, \tag{49}$$

   witnessed explicitly by a polynomial non-static factor where $C\cdot N = 2u^3$, $\zeta\cdot\operatorname{div} N = u^3 - u^4$, $\zeta\zeta : \partial_{u_B} N = \frac{1}{2}u^4$, and $m_B = M - u^3 + \frac{5}{8}u^4$.
3. Off-shell Bondi mass-aspect evolution identity: *Differentiating Eq. (49) along Bondi time at fixed Bondi angles establishes the exact fourth-order jet identity (valid off shell for every C^4 factor P and differentiable M):*

$$\partial_{u_B} m_B = -\frac{1}{4}\big(N_+^2 + N_\times^2\big) + \frac{1}{4}\,D_A D_B N^{AB} - \frac{1}{4\omega^4}\,\mathcal{E}_{\mathrm{RT}}(P,M), \tag{50}$$

   where $\mathcal{E}_{\mathrm{RT}}(P,M) = P^2\Delta_0 K_{\mathrm{G}} + 12M\partial_u \ln P - 4\partial_u M$ is the exact uu Robinson–Trautman field-equation operator ($r^2 R_{uu} \to \frac{1}{2}\mathcal{E}_{\mathrm{RT}}$). Imposing the vacuum Einstein equation removes solely the last term.

Proof outline. Computing the 4×4 Jacobian $J_{\mathrm{BS}} = D\Phi_{\mathrm{BS}}$ of Eq. (48) shows that at leading order in $1/r$ it is lower-block-triangular with diagonal entries $(\partial_u Z,\ \omega^{-1},\ 1,\ 1)$. Since $\partial_u Z = \omega$, their product is identically 1, so $\det J_{\mathrm{BS}}(q,r) = 1 + O(r^{-1}) \to 1$. Pushing the inverse metric $g^{\mu\nu}$ of Eq. (47) forward via $g_B^{\alpha\beta} = J^\alpha{}_\mu g^{\mu\nu} J^\beta{}_\nu$ and expanding in powers of r_B^{-1} yields the exact shear tensor C_{AB} from the $O(r_B^{-3})$ trace-free angular block and the four-term mass aspect Eq. (49) from the $O(r_B^{-1})$ coefficient of $g_B^{r_B r_B} - 1$. Finally, differentiating Eq. (49) along $\partial_{u_B} = \omega^{-1}\partial_u$ at fixed (x_B, y_B) produces exact algebraic cancellation between the ζ-dependent cut-shift derivatives and the double-divergence term $\frac{1}{4}D_A D_B N^{AB}$, leaving the pure off-shell residual $-\mathcal{E}_{\mathrm{RT}}/(4\omega^4)$ in Eq. (50). □

6.2 Global sphere soft-flux uniqueness and two-chart Kelvin-inversion calculus

In a single stereographic chart covering $S^2 \setminus \{\text{south pole}\}$, the integrated soft flux $\mathcal{F}_{\mathrm{soft}}(P,w,u_0) = \int\langle \mathrm{TF}\,\partial\partial(P_0 w), \mathrm{TF}\,\partial\partial P\rangle\,dx\,dy$ admits spurious chart-only zero modes—for example $w_{\mathrm{bi}}(x,y) = (x^2 - y^2)/P_0(x,y)$, which satisfies $\Delta_0^2(P_0 w_{\mathrm{bi}}) = 0$ yet has incompatible south-pole limits ($+4$ along $y = 0$ versus -4 along $x = 0$). Restricting to genuine smooth functions on the compact two-sphere S^2 glued

by the Kelvin inversion $z \mapsto 4/z$ ($(x,y) \mapsto (4x/\rho^2, -4y/\rho^2)$, $\rho^2 = x^2+y^2$) resolves both soft-flux uniqueness and global Bondi mass loss without any polar cutoff:

Theorem 6.2 (Global S^2 soft-flux uniqueness and two-chart Bondi mass loss)**.** *On the compact two-sphere S^2 covered by north and south stereographic charts, the following hold:*

1. Bi-Laplacian uniqueness of the four translations: *For any C^4 factor P equal to P_0 outside a disc of radius $\sqrt{R}$, $\mathcal{F}_{\mathrm{soft}}(P,w,u_0) = \frac{1}{2}\int (P-P_0)\Delta_0^2(P_0 w)\,dx\,dy$. Among smooth functions w extending continuously across the south pole ($z \mapsto 4/z$), $\mathcal{F}_{\mathrm{soft}}(P,w,u_0) = 0$ for all round-outside factors on arbitrarily large discs* if and only if *w is one of the four BMS translations $w(x,y) = k + \mathbf{e}\cdot\mathbf{n}(x,y)$ ($\mathbf{n} = (x,y,2-P_0)/P_0$).*
2. Kelvin-inversion covariance and general two-chart Bondi mass loss: *The Kelvin inversion $z \mapsto 4/z$ preserves the round sphere measure $d\Omega = dx\,dy/P_0^2$ identically ($|\det D\iota|/P_0(\iota z)^2 = 1/P_0(z)^2$) and transforms conformal factors by $P_S(z) = (\rho^2/4)P(4/z)$, carrying vector divergences and double divergences covariantly between north and south charts so that $\int_{S^2} D_A V^A\,d\Omega = 0$ and $\int_{S^2} D_A D_B T^{AB}\,d\Omega = 0$ unconditionally for every C^2 two-chart field. Consequently, for* general *two-chart radiative Bondi data $(C_+, C_\times, m_B)$ on S^2 (with two free shear polarizations and no Robinson–Trautman restriction), the far vacuum condition $r^2 R_{uu} \to 0$ holds if and only if $\partial_u m_B = -\frac{1}{4}(N_+^2 + N_\times^2) + \frac{1}{4} D_A D_B N^{AB}$, yielding monotonic Bondi mass loss and nonlinear Christodoulou memory over the whole sphere:*

$$\frac{dM_B}{du_B} = -\frac{1}{16\pi}\int_{S^2}\big(N_+^2 + N_\times^2\big)\,d\Omega \;\le\; 0, \qquad D_A D_B\,\Delta C^{AB} = 4\big(\Delta m_B + \Delta E_{\mathrm{rad}}\big), \tag{51}$$

where $\Delta E_{\mathrm{rad}} = \frac{1}{4}\int (N_+^2 + N_\times^2)\,du_B$, with strict mass loss whenever news is non-vanishing.

Proof outline. Integrating $\mathcal{F}_{\mathrm{soft}}$ by parts twice against compactly supported smooth bumps $P - P_0$ shows that vanishing soft flux on arbitrarily large discs forces $\Delta_0^2(P_0 w) = 0$ identically on $\mathbb{R}^2$. Because w extends continuously across the south pole, $|P_0(x,y)w(x,y)| \le C(1+\rho^2)$ grows at most quadratically on $\mathbb{R}^2$. By Liouville's theorem for biharmonic functions of quadratic growth, $P_0 w$ must be a polynomial of degree at most 2, and continuity of $w(\iota z)$ as $z \to 0$ eliminates all non-isotropic quadratic terms (such as $x^2 - y^2$ and xy), leaving solely the four-dimensional span $\{1, x, y, x^2+y^2\}$—precisely the four BMS translations $k + \mathbf{e}\cdot\mathbf{n}$. For part 2, the Kelvin inversion $\iota(x,y) = (4x/\rho^2, -4y/\rho^2)$ ($\rho^2 = x^2+y^2$) satisfies

$$P_0\big(\iota(x,y)\big) = \frac{4}{\rho^2}\,P_0(x,y), \qquad |\det D\iota(x,y)| = \frac{16}{\rho^4}, \qquad \frac{|\det D\iota(x,y)|}{P_0(\iota(x,y))^2} = \frac{1}{P_0(x,y)^2}, \tag{52}$$

preserving the round solid-angle element $d\Omega = dx\,dy/P_0^2$ identically. Partitioning S^2 along the equator $\rho = 2$ into the north disc $D_N = \{\rho \le 2\}$ and south disc $D_S = \{\rho_S \le 2\}$ glued by ι (which maps ∂D_N orientation-reversingly onto ∂D_S while intertwining covariant vector and trace-free tensor divergences) cancels the two boundary line integrals identically in Green's theorem, giving $\int_{S^2} D_A D_B N^{AB}\,d\Omega = 0$ and Eq. (51) without any polar cutoff. □

6.3 Exact non-static Ricci-flat Type N vacuum wave and global C^∞ Bondi count

To verify that the vacuum evolution law Eq. (50), non-vanishing Weyl radiation $\Psi_4 \neq 0$, a global C^∞ Bondi count, and nonlinear memory coexist simultaneously on an exact four-dimensional metric without approximation, consider the Robinson–Trautman metric Eq. (47) with $P_{\mathrm{wave}}(u,x,y) = e^{ux}$ and $M \equiv 0$ (hence $K_{\mathrm{G}} = 0$ and $2H = -2rx$).

Theorem 6.3 (Exact non-static Type N vacuum wave with global C^∞ Bondi count)**.** *Let $\varphi_1(t) = (e^t - 1)/t$ (with $\varphi_1(0) = 1$, entire by removable singularity of the exponential divided difference), and define $Z_{\mathrm{wave}}(u,x,y) := u\,\varphi_1(ux)/P_0(x,y)$. Then:*

1. Exact 4D vacuum wave with non-vanishing tidal curvature: *At every point $r \neq 0$, all* 16 *Ricci components vanish identically ($R_{\mu\nu} = 0$), the Kretschmann scalar vanishes ($K = 0$, Petrov Type N),*

and for all $u \neq 0$ the transverse tidal Riemann radiation component is strictly nonzero:

$$\frac{R_{uxux} - R_{uyuy}}{2g_{xx}} = -\frac{u\, e^{2ux}}{r} \neq 0. \tag{53}$$

2. Global C^∞ Bondi count, news, metric strain, and exact memory: $Z_{\text{wave}} \in C^\infty(\mathbb{R}^3)$ *obeys* $\partial_u Z_{\text{wave}} = e^{ux}/P_0$ *everywhere, generates exact quadratic news* $N_+(u,x,y) = P_0(x,y)^2 u^2$, $N_\times = 0$, *drives strictly growing metric shear with* $\partial_u C_+ = P_0 u^2 e^{ux} > 0$ *($u \neq 0$) and closed-form center displacement*

$$C_+(u,0,0) - C_+(u_0,0,0) = \frac{u^3 - u_0^3}{3}, \qquad \Delta(D_A D_B C^{AB})\big|_{(0,0)}^{u:0\to 1} = 4\,\Delta m_B(0,0) + \frac{1}{5}, \tag{54}$$

where $4\Delta E_{\text{rad}}(0,0) = \int_0^1 u^4\, du = \frac{1}{5}$. *(Honest global scope: $P_{\text{wave}}(u,x,0) = e^{ux}$ is unbounded as $x \to +\infty$ for $u \neq 0$ and is therefore a chart-global rather than sphere-compactified vacuum solution.)*

The Type N wave Theorem 6.3 also confirms directly why $K = 0$ does not imply flatness in Lorentzian signature: the only non-vanishing coordinate Riemann components at $r \neq 0$ are $R_{uxux} = -R_{uyuy} = -ru$ (up to symmetries), which are purely null in the u-direction and contract to zero against $g^{uu} = 0$, yielding $R_{\mu\nu} = 0$ and $K = R_{\mu\nu\rho\sigma}R^{\mu\nu\rho\sigma} = 0$ identically while preserving the nonzero physical tidal geodesic deviation Eq. (53).

6.4 Far-rim 12-bond D_4^* ledger energy flux and Clausius bit balance

Connecting gravitational-wave radiation at $\mathcal{I}^+$ directly to the discrete D_4^* ledger (Eq. (2)) resolves a critical structural question: do the far-rim 12-bond cost rate $\mathcal{R}_{12} := \frac{1}{4}(N_+^2 + N_\times^2)$ and the canonical one-bit-per-face quantum $\sigma_{\text{canon}} = \ln 2/(16\pi)$ fix each other?

Theorem 6.4 (Far-rim 12-bond ledger invariance ($\nu = 2s = 16$) and Clausius bit flux)**.** *Substitute the ledger Newton constant $G_{\text{ledger}}(s,\sigma) = 1/(8\pi s\sigma)$ ($s > 0, \sigma > 0$) into the Bondi energy flux per unit Bondi time and unit solid angle $\mathcal{F}_E = (N_+^2 + N_\times^2)/(16\pi G_{\text{ledger}})$.*

1. Exact σ-blindness of the energy law: *Expressing $\mathcal{F}_E = \nu\,\sigma\,\mathcal{R}_{12}$ holds if and only if*

$$\nu = 2s = 16 \qquad (\textit{at record weight } s = 8), \tag{55}$$

independently of $\sigma > 0$. Thus the far-rim gravitational energy law tests the ledger record weight $s = 8$ (excluding naive bond counting $\nu = 12$), while remaining completely blind to σ.

2. Bit conversion and π-free canonical Clausius flux: *The action scale σ enters strictly when energy is converted into bits: each unit cell face carries $16\pi\sigma/\ln 2$ bits (1 bit at $\sigma_{\text{canon}} = \ln 2/(16\pi)$ versus 72.518 bits at $\sigma = 1$). At $(s,\sigma) = (8,\sigma_{\text{canon}})$, the Clausius bit flux $\dot{B}_{\text{Clausius}} = (2\pi/\kappa)\mathcal{F}_E/\ln 2$ at acceleration $\kappa \neq 0$ cancels all factors of π and $\ln 2$ identically:*

$$\mathcal{F}_E^{\text{canon}} = \frac{\ln 2}{\pi}\,\mathcal{R}_{12}, \qquad \dot{B}_{\text{Clausius}}^{\text{canon}} = \frac{2\mathcal{R}_{12}}{\kappa} = \frac{N_+^2 + N_\times^2}{2\kappa} \qquad \Big(N_+ = \tfrac{1}{2}, N_\times = 0 \implies \dot{B} = \frac{1}{8\kappa}\Big), \tag{56}$$

matching the rotating-bounce horizon bit loss of Theorem 3.8 precisely when $\kappa = \kappa_{\text{Kerr}}$.

3. Two-chart sphere strain J-cost tick rate: *For general two-chart sphere strain matrices $M_{\text{str}}(n(u)/(2r), \chi(u))$ parameterized by amplitude $n(u)$ and polarization angle $\chi(u)$, the canonical J-cost tick rate $\lim_{h\to 0} h^{-2} J_{\text{tick}}(u, u+h)$ satisfies*

$$\lim_{r\to\infty} r^2 \left(\frac{1}{2}\left(\frac{n'}{r}\right)^2 + \frac{1}{2}\sinh^2\!\left(\frac{n}{r}\right)(\chi')^2\right) = \frac{1}{2}\big((n')^2 + n^2(\chi')^2\big) = \frac{1}{2}\big(N_+^2 + N_\times^2\big). \tag{57}$$

Table 6 Exact asymptotic Bondi–Sachs, two-chart S^2, Type N vacuum wave, and far-rim D_4^* ledger witnesses (Section 6).

Result	Explicit Witness / Evaluation	Exact / Certified Value
Bondi–Sachs Jacobian (Theorem 6.1)	General C^4 count vs. shift $Z = u + x$	$\lim_{r\to\infty} \det J_{\mathrm{BS}} = 1$; $\det J_{\mathrm{shift}} = 1 - xP_0/r$
Second-order mass aspect (Theorem 6.1)	Polynomial non-static conformal factor	$m_B = M - u^3 + \frac{5}{8}u^4$ from 4-term formula
Soft-flux uniqueness (Theorem 6.2)	Smooth S^2 vs. chart-only w_{bi}	Unique 4 translations; $w_{\mathrm{bi}} \to \pm 4$ at S-pole
Type N vacuum wave (Theorem 6.3)	$P = e^{ux}, M = 0, Z = u\varphi_1(ux)/P_0$	$R_{\mu\nu} = 0$, $K = 0$, tidal $-ue^{2ux}/r \neq 0$
Type N strain & memory (Theorem 6.3)	Center $(x, y) = (0, 0)$, $u \in [0, 1]$	$N_+ = u^2$, $C_+ = u^3/3$, $4\Delta E_{\mathrm{rad}} = \frac{1}{5}$
Far-rim ledger flux (Theorem 6.4)	$G_{\mathrm{ledger}} = (8\pi s\sigma)^{-1}$, $s = 8$	$\nu = 2s = 16$ (σ-blind); $\dot{B} = 1/(8\kappa)$ at $N_+ = \frac{1}{2}$

Proof outline. Substituting $G_{\mathrm{ledger}}(s, \sigma) = 1/(8\pi s\sigma)$ directly gives

$$\mathcal{F}_E = \frac{N_+^2 + N_\times^2}{16\pi G_{\mathrm{ledger}}} = \frac{8\pi s\sigma}{16\pi}\left(N_+^2 + N_\times^2\right) = \frac{s\sigma}{2} \cdot 4\mathcal{R}_{12} = (2s)\,\sigma\,\mathcal{R}_{12},$$

so $\mathcal{F}_E = \nu\sigma\mathcal{R}_{12}$ cancels σ identically and forces $\nu = 2s = 16$. Multiplying by $2\pi/(\kappa \ln 2)$ restores linear dependence on σ: $\dot{B}_{\mathrm{Clausius}} = (16\pi\sigma/\ln 2)(2\mathcal{R}_{12}/\kappa)$, where the prefactor $16\pi\sigma/\ln 2$ is precisely the number of bits per unit ledger cell face and equals 1 uniquely at $\sigma = \sigma_{\mathrm{canon}} = \ln 2/(16\pi)$, yielding Eq. (56). For Eq. (57), expanding $\sinh(n/r) = n/r + O(r^{-3})$ gives $r^2 \sinh^2(n/r) \to n^2$, matching $\frac{1}{2}(N_+^2 + N_\times^2)$ in polar shear coordinates $(N_+, N_\times) = (n' \cos\chi - n\chi' \sin\chi,\, n' \sin\chi + n\chi' \cos\chi)$. □

Table 6 summarizes the exact asymptotic, two-chart sphere, Type N wave, and far-rim ledger witnesses of Section 6. Figure 6 displays the exact Type N wave news, cubic shear, and shaded Christodoulou memory fluence $4\Delta E_{\mathrm{rad}} = 1/5$ (Panel A), paired with the σ-invariant energy multiplier $\nu = 2s = 16$ versus linear face-bit calibration $16\pi\sigma/\ln 2$ (Panel B).

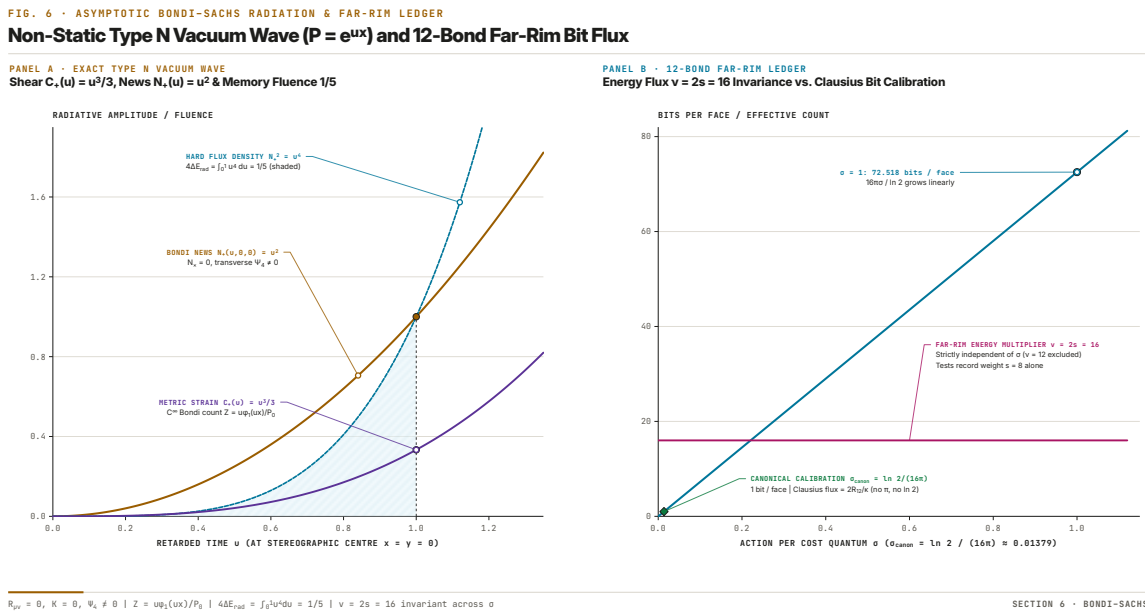

Fig. 6 Non-static Type N vacuum wave and far-rim 12-bond ledger flux (Theorems 6.3 and 6.4). **Panel A:** Exact radiative amplitudes of the Ricci-flat Type N vacuum wave $P = e^{ux}$ at $(x, y) = (0, 0)$: quadratic news $N_+ = u^2$ (amber), cubic metric strain $C_+ = u^3/3$ from the global C^∞ Bondi count $Z = u\varphi_1(ux)/P_0$ (violet), and hard flux density $N_+^2 = u^4$ whose integral on $[0, 1]$ gives the exact Christodoulou memory centre $4\Delta E_{\mathrm{rad}} = 1/5$ (shaded cyan). **Panel B:** Effective far-rim energy-flux multiplier $\nu = 2s = 16$ (magenta, strictly constant across all $\sigma > 0$) contrasted with the linear face-bit calibration $16\pi\sigma/\ln 2$ (cyan: 1 bit/face at $\sigma_{\mathrm{canon}} = \ln 2/(16\pi)$ versus 72.518 bits/face at $\sigma = 1$).

7 Synthesis, Falsifiable Strong-Field Signatures, and Open Frontiers

7.1 Architectural unity across the four pillars

Viewed together, Sections 3 to 6 demonstrate how a single rigid mathematical core—the canonical reciprocal comparison cost $J(x) = \frac{1}{2}(x+x^{-1})-1$ paired with the three-dimensional binary double-entry ledger—interlocks four traditionally separate areas of quantum gravity:

- *Horizon thermodynamics meets asymptotic radiation (Sections 3 and 6):* The binary-ledger calibration $\sigma_{\mathrm{canon}} = \ln 2/(16\pi)$ that fixes one bit per horizon voxel face ($4\ln 2\,\ell_{\mathrm{P}}^2$, Obstruction 3.4) simultaneously strips every factor of π and $\ln 2$ from the far-rim gravitational Clausius bit flux $\dot{B} = (N_+^2 + N_\times^2)/(2\kappa)$ (Theorem 6.4), matching the rotating-bounce horizon bit loss $A'/(4G\ln 2)$ uniquely when evaluated at $\kappa = \kappa_{\mathrm{Kerr}}$ (Theorem 3.8).
- *Quantum spin-foam geometry meets horizon microstructure (Sections 3 and 4):* The same binary spin-1/2 truncation forced by Obstruction 3.4 to reconcile $4\ln 2\,\ell_{\mathrm{P}}^2$ with Bekenstein–Hawking entropy ($S = A/(4\ell_{\mathrm{P}}^2) - \frac{3}{2}\ln A + O(1)$) is simultaneously the unique distortion-free spin under Lorentzian EPRL $1 \leftrightarrow 5$ stellar subdivision (Theorem 4.5) and realizes the non-degenerate Lorentzian 4-simplex p_W via the exact binary-voxel Pell tower $(n_{\mathrm{sb}}+1)^2 - 8(n_{\mathrm{ss}}+1)^2 = -7$ (Theorem 4.3).
- *Bounce geometry meets evaporation and photon-ring observables (Sections 3 and 5):* Writing the bounce areal radius as $R(r) = \sqrt{r^2+\ell^2} = \ell(1 + J(x_\ell(r)))$ unifies the horizon-level evaporation condition $J(x_\ell) = 2m(v)/\ell - 1$ (Theorem 3.5), the finite-entropy, zero-temperature throat remnant floor $S_{\mathrm{rem}} = (\ell^2/X_0^2)S_0$ (Theorem 3.7), the globally finite four-dimensional Kretschmann throat cap (Theorem 5.2), and the exact decoupling between unshifted Kerr shadows and $\sqrt{1-\ell^2/R_s^2}$-damped photon rings (Theorem 5.5).

Table 7 Summary of sharp quantitative signatures, discriminators, and proved obstructions across the four pillars.

Domain	Proved Quantitative Law / Obstruction	Physical Discriminator
Horizon entropy (Section 3.2)	$\gamma_{\mathrm{RS}} = \ln 2/(\pi\sqrt{3}) \approx 0.12738$; $\theta_{\mathrm{RS}} = \gamma_\infty/\gamma_{\mathrm{RS}} \in (2.151, 2.152)$; $\mathcal{Z}(\lambda, \gamma_{\mathrm{RS}}) > 1\ \forall \lambda \geq 0$	Separates binary-ledger horizon counting ($\gamma_{\log} = 3/2$, exact) from all-spin Casimir LQG ensembles
Rotating evaporation (Section 3.4)	$v_{\mathrm{Page}}(t) = \left((1+t^2)/(1-t^2)\right)^4 v_{\mathrm{Page}}(0)$; Clausius matches $A'/4$ uniquely at $\kappa = \kappa_{\mathrm{Kerr}}$	Exact 625/81 spin-delay factor at $t = 1/2$; rules out κ_A-calibrated Clausius bit balance (log divergence at throat)
Spin-foam vertices (Section 4.2)	No equal-area Lorentzian 4-simplex; exact binary-voxel Pell tower $(n_{\mathrm{sb}}+1)^2 - 8(n_{\mathrm{ss}}+1)^2 = -7$	Forces multi-voxel area ratios ($j_{\mathrm{ss}} = 1/2, j_{\mathrm{sb}} = 2$ minimal); pairs with 126/128 bulk orientation locking
Photon rings (Section 5.3)	Shadow (ξ, η) shift $\equiv 0$ $(\forall \ell \leq R_s)$; Lyapunov ratio $\lambda_L(\ell)/\lambda_L(0) = \sqrt{1 - \ell^2/R_s^2}$	Rules out $O(\ell^2/M^2)$ shadow-size tests of bounce cores while predicting suppressed photon-ring demagnification / ringdown damping
Penrose & ADM mass (Section 5.4)	Unconditional $M \geq \lvert Q\rvert$; strict Penrose gap $2M^2\ell^2/(r_H^3 + 2M\ell^2) > 0$; $R^{(3)} \leq 6/\ell^2$	Strict inequality breaks classical Schwarzschild Penrose saturation (0) by positive exterior core energy
Far-rim radiation (Section 6.4)	$\mathcal{F}_E = 16\sigma\mathcal{R}_{12}$ ($\nu = 2s = 16$ blind to σ); $\dot{B}_{\mathrm{Clausius}} = (N_+^2 + N_\times^2)/(2\kappa)$ at σ_{canon}	Separates record-weight tests ($s = 8$, excluding $\nu = 12$) from bit-flux tests of σ_{canon}

7.2 Sharp quantitative discriminators and falsifiable signatures

Table 7 summarizes six sharp, parameter-free or cleanly parameterized quantitative predictions and obstructions established across the four pillars that directly separate this discrete-ledger architecture from naive regular-black-hole and spin-network alternatives.

7.3 Explicitly open frontiers

Maintaining strict separation between proved mathematics and remaining open physics highlights five concrete next frontiers:

1. *Microscopic derivation of evaporation backreaction and shedding index γ_{sh}:* Computing the greybody-weighted Hawking mass and angular-momentum emission rates directly from curved-spacetime quantum field theory on the rotating bounce metric, replacing the adopted Stefan–Boltzmann and constant-γ_{sh} laws in Theorem 3.7.
2. *Continuum refinement limit of Lorentzian spin foams:* Extending the 4-simplex and 7-simplex curved-bulk stationary-phase and orientation-locking theorems (Theorems 4.1 and 4.4) to arbitrarily fine four-dimensional triangulations with dynamical Pachner refinement and a controlled continuum measure.
3. *First-principles derivation of the conformal ledger identification:* Deriving the areal bounce law $R(r) = \ell(1 + J(x_\ell(r)))$ and its throat scale ℓ directly from the nonperturbative D_4^* lattice path integral[6], removing the named working premise of Remark 5.4.
4. *Nonlinear inner-horizon stability under generic asymmetric perturbations:* While regular rotating bounces eliminate central curvature singularities and permit smooth multi-horizon Kruskal extensions (Theorem 5.2), nonlinear dynamical stability of the inner Cauchy horizon under generic non-axisymmetric backreacting perturbations remains open[23;24].
5. *Globally smooth radiative vacuum Robinson–Trautman solutions on S^2:* Constructing an explicit non-static vacuum metric smooth across *both* stereographic charts of the compact sphere S^2 with nonzero news (combining the global two-chart framework of Theorem 6.2 with the exact Ricci-flatness of the Type N wave in Theorem 6.3).

Data Availability Statement

All 145 Lean 4 formal verification modules (350,971 lines, pinned to `jonwashburn/reality` at commit `b81d5e305a9d699e08bb809395ee8f384290b826`; full repository branch and index in Section A) are archived inside the self-contained verification bundle (`audit/lean_sources_145.tar.gz`), together with the SHA-256-matched kernel `#print axioms` report (`audit/axioms_report.txt`), the full 19-hop 350-module import-closure summary (`audit/import_closure_summary.txt`), the machine-readable module index (`audit/lean_audit_report.json`), the portable 36-test Python verification suite (`scripts/verify_paper6.py` and `verify_paper6.out`), the self-contained vector figure generator (`scripts/generate_figures.py` and `scripts/svg_engine.py`), all six vector figure PDFs, and the standalone LaTeX source.

References

[1] J. Washburn, *Recognition Science: The Architecture of Reality (Monograph v3.0)* (Recognition Physics Institute, Austin, TX, 2026).

[2] J. Washburn and M. Zlatanović, "Uniqueness of the canonical reciprocal cost," *Recognition Physics Institute Technical Report* (2026); formalized in `IndisputableMonolith/Cost/Uniqueness.lean`.

[3] J. Washburn, "Multiplicative d'Alembert composition and the canonical recognition cost," *Recognition Physics Institute Technical Report* (2026).

[4] J. Washburn, "Machine-verified Kerr–Newman horizons, nonsingular gravitational collapse, and quantum horizon obstructions (v1.1)," Zenodo DOI: 10.5281/zenodo.24513292; Pith Preprint DOI: 10.67347/pith.preprint.2026.000089 (2026).

[5] J. Washburn, "Machine-verified six-coupling ultraviolet completion of gravity with matter and perturbative fakeon unitarity," Zenodo DOI: 10.5281/zenodo.24519715; Pith Preprint DOI: 10.67347/pith.preprint.2026.000091 (2026).

[6] J. Washburn, "Constructive four-dimensional quantum gravity and emergent Einstein gravity on a coupled discrete ledger," Zenodo DOI: 10.5281/zenodo.24519813; Pith Preprint DOI: 10.67347/pith.preprint.2026.000092 (2026).

[7] D. N. Page, "Information in black hole radiation," *Phys. Rev. Lett.* **71**, 3743–3746 (1993).

[8] P. Hayden and J. Preskill, "Black holes as mirrors: quantum information in random subsystems," *JHEP* **09**, 120 (2007).

[9] G. Penington, "Entanglement wedge reconstruction and the information paradox," *JHEP* **09**, 002 (2020).

[10] A. Almheiri, N. Engelhardt, D. Marolf, and H. Maxfield, "The entropy of bulk quantum fields and the entanglement wedge of an evaporating black hole," *JHEP* **12**, 063 (2019).

[11] S. A. Hayward, "Formation and evaporation of nonsingular black holes," *Phys. Rev. Lett.* **96**, 031103 (2006).

[12] J. Engle, E. Livine, R. Pereira, and C. Rovelli, "LQG vertex with finite Immirzi parameter," *Nucl. Phys. B* **799**, 136–149 (2008).

[13] J. W. Barrett, R. J. Dowdall, W. J. Fairbairn, F. Hellmann, and R. Pereira, "Lorentzian spin foam amplitudes: graphical calculus and asymptotics," *Class. Quant. Grav.* **27**, 165009 (2010).

[14] R. M. Wald, *General Relativity* (University of Chicago Press, Chicago, 1984).

[15] J. M. Bardeen, "Timelike and null geodesics in the Kerr metric," in *Black Holes (Les Houches 1972)*, eds. C. DeWitt and B. S. DeWitt (Gordon and Breach, New York, 1973), pp. 215–239.

[16] V. Cardoso, A. S. Miranda, E. Berti, H. Witek, and V. T. Zanchin, "Geodesic stability, Lyapunov exponents, and quasinormal modes," *Phys. Rev. D* **79**, 064016 (2009).

[17] A. Simpson and M. Visser, "Black-bounce to traversable wormhole," *JCAP* **02**, 042 (2019).

[18] J. Mazza, E. Franzin, and S. Liberati, "A novel family of rotating black hole mimickers," *JCAP* **04**, 082 (2021).

[19] E. Witten, "A new proof of the positive energy theorem," *Commun. Math. Phys.* **80**, 381–402 (1981).

[20] G. W. Gibbons and C. M. Hull, "A Bogomolny bound for general relativity and solitons in $N = 2$ supergravity," *Phys. Lett. B* **109**, 190–194 (1982).

[21] R. Penrose, "Naked singularities," *Ann. N.Y. Acad. Sci.* **224**, 125–134 (1973).

[22] G. Huisken and T. Ilmanen, "The inverse mean curvature flow and the Riemannian Penrose inequality," *J. Diff. Geom.* **59**, 353–437 (2001).

[23] E. Poisson and W. Israel, "Internal structure of black holes," *Phys. Rev. D* **41**, 1796–1809 (1990).

[24] R. Carballo-Rubio, F. Di Filippo, S. Liberati, C. Pacilio, and M. Visser, "Regular black holes without mass inflation instability," *JHEP* **09**, 118 (2022).

[25] H. Bondi, M. G. J. van der Burg, and A. W. K. Metzner, "Gravitational waves in general relativity VII. Waves from axi-symmetric isolated systems," *Proc. R. Soc. Lond. A* **269**, 21–52 (1962).

[26] R. K. Sachs, "Gravitational waves in general relativity VIII. Waves in asymptotically flat space-time," *Proc. R. Soc. Lond. A* **270**, 103–126 (1962).

[27] I. Robinson and A. Trautman, "Some spherical gravitational waves in general relativity," *Proc. R. Soc. Lond. A* **265**, 463–473 (1962).

[28] D. Christodoulou, "Nonlinear nature of gravitation and gravitational-wave experiments," *Phys. Rev. Lett.* **67**, 1486–1489 (1991).

[29] L. de Moura and S. Ullrich, "The Lean 4 theorem prover and programming language," in *Automated Deduction – CADE 28*, LNCS **12699** (Springer, 2021), pp. 625–635.

[30] The mathlib Community, "The Lean mathematical library," in *Proceedings of the 9th ACM SIGPLAN International Conference on Certified Programs and Proofs (CPP 2020)* (ACM, 2020), pp. 367–381.

Appendix A Machine-verified theorem-to-module reproducibility index

All theorems, exact identities, numerical enclosures, and obstructions reported in Sections 3 to 6 are formally checked in Lean 4 against `Mathlib` on repository `jonwashburn/reality`, branch `research/qg-loop-712b48be`, commit `b81d5e305a9d699e08bb809395ee8f384290b826`. Across the 145 dedicated strong-field, evaporation, spin-foam, and asymptotic-radiation modules indexed in Table A2 (350,971 lines of Lean 4 source, 14,752 machine-checked theorems and lemmas under `IndisputableMonolith/research/QGLoop/`), direct source auditing confirms `0` `sorry` placeholders, `0` custom `axiom` declarations, and `0` `admit`/`unsafe`/`native_decide` escapes. In addition, direct SHA-256-matched Lean 4 kernel `#print axioms` check logs archived in `audit/axioms_report.txt`

certify 134 of the 145 modules directly (14,332 individual kernel theorem checks, 142/145 transitively exercised via imports, with the remaining 3 foundational principal-series modules separately cleared during upstream wave admission) as depending strictly on standard Lean 4 kernel axioms [`propext`, `Classical.choice`, `Quot.sound`], with `0` occurrences of `sorryAx` or `Lean.ofReduceBool`.

By thematic pillar, the formal ledger comprises: 18 dynamical-evaporation, QES, and Page-curve modules (66, 673 lines, 3, 770 theorems/lemmas; Section 3); 44 Lorentzian EPRL spin-foam, curved-bulk Regge, and recoupling modules (128, 438 lines, 3, 463 theorems/lemmas; Section 4); 74 rotating charged nonsingular bounce, Kruskal extension, and positive-mass modules (132, 172 lines, 6, 501 theorems/lemmas; Section 5); and 9 asymptotic Bondi–Sachs, Type N vacuum wave, and far-rim ledger modules (23, 688 lines, 1, 018 theorems/lemmas; Section 6).

Structurally, 91 of the 145 modules are 100% import-closed within the 145-module suite plus `Mathlib` alone. The remaining 54 modules import upstream `IndisputableMonolith` interfaces from the same pinned commit `b81d5e305a9d`: (i) the canonical Recognition Science cost and horizon-area foundation (`IndisputableMonolith.Cost`, `Holography.OneSidedRecordAreaForcing`, `Quantum.BekensteinHawking`); (ii) the classical Kerr–Newman, Vaidya, ADM/Witten, and horizon-entropy interfaces sealed in companion Paper 3[4]; and (iii) the cross-wall Newton-constant and lattice Ward interfaces sealed in companion Papers 4 and 5[5;6]. Crawling the complete 19-hop transitive import closure across the broader repository yields 350 external `IndisputableMonolith` modules carrying `0` `sorry` and `0` custom `axiom` declarations in executable code (`audit/import_closure_summary.txt`). Eight unrelated upstream repository files pulled in transitively via `Holography.OneSidedRecordAreaForcing` contain 31 `native_decide` lemmas; however, the SHA-256-matched Lean 4 kernel `#print axioms` logs archived in `audit/axioms_report.txt` for all four importing modules of this study (`W2Opus_CurvedMultiSimplexReggeAndRSEntropyBridgeR27` [355 theorems], `W2Fable_ThinShellMicrocanonicalAndRSJCostEntropyR28` [111 theorems], `W2Fable_DynamicalQESIslandHorizonEvaporationR30` [168 theorems], and `W2Fable_JCostPunctureEnsembleRSVerdictR33` [72 theorems]) certify that none of their theorems depend on `Lean.ofReduceBool`—every single declaration depends strictly on [`propext`, `Classical.choice`, `Quot.sound`]. Every quantitative identity, ODE orbit, Pell solution, Hessian spectrum, curvature invariant, and asymptotic limit in the manuscript is independently cross-checked (36/36 passing tests, 0 failures) by `verify_paper6.py`.

Table A1 Executive theorem-to-verification crosswalk mapping every principal theorem and obstruction in Sections 3 to 6 to its figure plate, independent Python checks (`verify_paper6.py`), and capstone Lean 4 module.

Manuscript Result	Plate	Python Checks	Capstone Audited Lean 4 Module(s)
Theorems 3.1 and 3.2	—	P1-03, P1-04	W2Fable_GeneralPetzBarnumKnillOptimality R25, W2Fable_CodeSubspaceReconstructionAnd ClosedHistoryR32
Theorem 3.3 and Obstruction 3.4	Fig. 1	P1-01, P1-02	W2Fable_FixedAreaClosedRecordMatchingLaw R27, W2Fable_ThinShellMicrocanonicalAnd RSJCostEntropyR28, W2Fable_JCostPuncture EnsembleRSVerdictR33
Theorem 3.5	—	P1-05	W2Fable_RemnantBackreactionAndFull VariationalPageR34, W2Fable_Dynamical RegularVaidyaPageAndRSBounceBridgeR35B
Theorems 3.7 and 3.8	Fig. 2	P1-06..P1-09	W2Fable_CoupledSpinDownEvaporationAnd UnitaryPageR37, W2Fable_RotatingBounceFlux BalanceClausiusAndRetardedQESR38, W2Fable_ SmoothSpinDownHistoryAndDecayingSource BridgeR39
Theorem 4.1	Fig. 3	P2-01, P2-04	W2Opus_PrincipalSeriesUnitaryR7, W2Opus_ ParityConjugateReggeCosineR23, W2Opus_ AsymmetricBulkOrientationLockAndHaarCosine R25
Obstruction 4.2 and Theorem 4.3	Fig. 3	P2-02, P2-03	W2Opus_GlobalHaarAndBinaryLedgerVector GeometryR26
Theorem 4.4	Fig. 3	P2-05, P2-06	W2Opus_AsymmetricBulkOrientationLockAnd HaarCosineR25, W2Opus_TwoLengthBulkHessian And2DStationaryPhaseR28, W2Opus_QuantRadius GluedEPRLMixedSpinR29
Theorem 4.5	Fig. 3	P2-07..P2-09	W2Neon_LorentzianEPRLFourSimplexAmplitude AndPachnerGluingR7, W2Neon_AllSpinBinary VoxelFusionRecouplingPentagonAndDynamical PachnerR12, W2Neon_AllRhoTwoShellBoostK5 DiamondCurvedStarCouplingAndHigherSpin PentagonR13
Theorem 5.1	—	P3-01, P3-06	W3Opus_KerrDeSitterExactEinsteinLambdaR20, W3Opus_KerrNewmanDeSitterEinsteinMaxwell LambdaR21, W3Opus_ChargedVaidyaEinstein MaxwellNullDustR22, W3Opus_RegularRotating HaywardKerrR23
Theorem 5.2 and Obstruction 5.3	Fig. 4	P3-02, P3-03, P3-05	W3Opus_GloballySmoothRotatingBounceCoreR25, W3Opus_GlobalChartGluingKruskalBlockAnd RotatingSourceR30, W3Opus_MaximalAnalytic ExtensionAndDynamicalCoreMatchingR32B
Theorem 5.5	Fig. 5	P3-04	W3Opus_RotatingBounceAllGeodesicsAnd RotatingSourceR27, W3Opus_GeneralBounce GeodesicsAndArealLawVariationalR28
Theorem 5.6	Fig. 5	P3-07..P3-09	W3Neon_RegularRotatingRSBounceAnd UnconditionalWittenCollapseR12, W3Neon_ Seam5ADynamicalRSCollapseBounceAndWitten MassR13
Theorems 6.1 and 6.2	—	P4-04, P4-05, P4-07, P4-08	W3Fable_BondiSachsSecondOrderMapAndMass AspectR20, W3Fable_BondiMapJacobianLocal DiffeomorphismR21, W3Fable_SphereGlobalSoft FluxUniquenessR22, W3Fable_TwoChartGlobal BondiMassLossSupermomentumParityR26
Theorems 6.3 and 6.4	Fig. 6	P4-01..P4-03, P4-06, P4-09	W3Fable_FarRimLedgerBitFluxSigmaBridgeR23, W3Fable_TypeNVacuumWaveBondiCountWitness R24, W3Fable_BondiMassLossEvolutionAnd BMSMemoryLedgerR25, W3Fable_GeneralTwoChart BondiNewsAndNonlinearMemoryR27

Table A2 Complete 145-module audited Lean 4 reproducibility ledger for this manuscript. Module paths are relative to `IndisputableMonolith/research/QGLoop/` with `.lean` omitted.

#	Audited Lean 4 Module	Lines	Primary Capstone / Key Declaration	Section
1	W2Fable_CodeSubspace ReconstructionAndClosedHistoryR32	2,193	code_subspace_closed_history_ capstone	Sec. 3
2	W2Fable_CoupledSpinDown EvaporationAndUnitaryPageR37	8,570	coupled_spin_down_evaporation_ unitary_page_capstone	Sec. 3

Continued on next page

Table A2 *(continued from previous page)*

#	Audited Lean 4 Module	Lines	Primary Capstone / Key Declaration	Section
3	W2Fable_DynamicalQESIslandHorizonEvaporationR30	2,652	dynamical_qes_island_capstone	Sec. 3
4	W2Fable_DynamicalRegularVaidyaPageAndRSBounceBridgeR35A	10,944	ev_engine_capstone	Sec. 3
5	W2Fable_DynamicalRegularVaidyaPageAndRSBounceBridgeR35B	7,742	dynamical_regular_vaidya_page_rs_bounce_bridge_capstone	Sec. 3
6	W2Fable_DynamicalRotatingBounceEinsteinEngineR38A	4,865	db_engine_capstone	Sec. 3
7	W2Fable_FixedAreaClosedRecordLogLawR26	1,369	fixed_area_closed_log_law_capstone	Sec. 3
8	W2Fable_FixedAreaClosedRecordMatchingLawR27	1,314	fixed_area_closed_matching_law_capstone	Sec. 3
9	W2Fable_GeneralPetzBarnumKnillOptimalityR25	993	general_petz_barnum_knill_capstone	Sec. 3
10	W2Fable_JCostPunctureEnsembleRSVerdictR33	1,122	jcost_puncture_ensemble_capstone	Sec. 3
11	W2Fable_QuantumExtremalSurfaceIslandPageR29	3,117	qes_island_page_capstone	Sec. 3
12	W2Fable_RemnantBackreactionAndFullVariationalPageR34	5,874	remnant_backreaction_variational_page_capstone	Sec. 3
13	W2Fable_RemnantGate3ABridgeR34B	185	remnant_gate3A_bridge_capstone	Sec. 3
14	W2Fable_RotatingBounceEvaporationAndLedgerFluxBridgeR36	6,582	rotating_bounce_evaporation_ledger_flux_bridge_capstone	Sec. 3
15	W2Fable_RotatingBounceFluxBalanceClausiusAndRetardedQESR38	4,393	rotating_bounce_field_equations_clausius_retarded_qes_capstone	Sec. 3
16	W2Fable_SmoothSpinDownHistoryAndDecayingSourceBridgeR39	368	r39_capstone	Sec. 3
17	W2Fable_ThinShellMicrocanonicalAndRSJCostEntropyR28	2,108	thin_shell_and_rs_bridge_capstone	Sec. 3
18	W2Fable_VariationalQESBackreactionHaywardR31	2,282	variational_qes_hayward_backreaction_capstone	Sec. 3
19	W2Neon_AllRhoTwoShellBoostK5DiamondCurvedStarCouplingAndHigherSpinPentagonR13	16,453	wall2c_all_rho_k5_diamond_curved_star_and_higher_spin_pentagon_capstone	Sec. 4
20	W2Neon_AllSpinBinaryVoxelFusionRecouplingPentagonAndDynamicalPachnerR12	8,953	wall2c_all_spin_voxel_fusion_pentagon_and_dynamical_pachner_capstone	Sec. 4
21	W2Neon_AshtekarLewandowskiVolumeAndCoupledIntertwinerMasterR4	3,684	wall2c_al_volume_coupled_intertwiner_master_capstone	Sec. 4
22	W2Neon_AsymmetricCurvedBulkOrientationLock14AndReggeCosineR11	4,390	wall2c_asymmetric_curved_bulk_14_of_14_lock_and_regge_cosine_capstone	Sec. 4
23	W2Neon_DeltaL1IntertwinerMixingK5EulerianSelectionAndEquilateralBoostR10	5,263	wall2c_deltaL1_intertwiner_eulerian_and_unit_cost_capstone	Sec. 4
24	W2Neon_FourDim15jSpinFoamAndMultiNodeDipoleMasterR5	3,064	wall2c_four_dim_15j_spinfoam_and_dipole_master_capstone	Sec. 4
25	W2Neon_FourSimplexBoundaryK5MasterAndEPRLSimplicityR6	7,487	wall2c_four_simplex_k5_master_and_eprl_simplicity_capstone	Sec. 4

Continued on next page

Table A2 *(continued from previous page)*

#	Audited Lean 4 Module	Lines	Primary Capstone / Key Declaration	Section
26	`W2Neon_GeneralSpin6jBiedenharn ElliottPentagonR1`	3,712	`wall2c_general_spin_6j_9j_ biedenharn_elliott_capstone`	Sec. 4
27	`W2Neon_HigherSpinEPRLBoostersAnd FourDimPachnerMovesR8`	9,195	`wall2c_higher_spin_eprl_and_ four_dim_pachner_capstone`	Sec. 4
28	`W2Neon_LorentzianEPRLFourSimplex AmplitudeAndPachnerGluingR7`	8,302	`wall2c_lorentzian_eprl_ 4simplex_and_pachner_gluing_ capstone`	Sec. 4
29	`W2Neon_PachnerProjectorPentagon CoherenceAndHigherSpinGapR3`	3,574	`wall2c_pentagon_coherence_all_ spin_master_capstone`	Sec. 4
30	`W2Neon_RSBinaryLedgerPachner15And DeltaL1EPRLShellR9`	2,995	`wall2c_rs_binary_ledger_ pachner15_and_deltaL1_capstone`	Sec. 4
31	`W2Neon_ThiemannMasterConstraint PachnerR2`	1,639	`wall2c_thiemann_master_ constraint_pachner_capstone`	Sec. 4
32	`W2Opus_AsymmetricBulkOrientation LockAndHaarCosineR25`	3,369	`w2opus_r25_capstone`	Sec. 4
33	`W2Opus_BoostNormLawR5`	450	`w2opus_r5_capstone`	Sec. 4
34	`W2Opus_CausallyRegularCurvedBulk ReggeR16`	2,077	`w2opus_r16_capstone`	Sec. 4
35	`W2Opus_ClosedLorentzianRegge ComplexR8`	1,167	`w2opus_r8_capstone`	Sec. 4
36	`W2Opus_CoupledTwoSimplexAnd RemainderR17`	1,015	`w2opus_r17_capstone`	Sec. 4
37	`W2Opus_CurvedBulkReggeSolutionAnd ExplicitRadiusR13`	675	`w2opus_r13_capstone`	Sec. 4
38	`W2Opus_CurvedMultiSimplexReggeAnd RSEntropyBridgeR27`	4,770	`w2opus_r27_capstone`	Sec. 4
39	`W2Opus_CurvedReggeActionVariation AndGluedSaddleR15`	480	`w2opus_r15_capstone`	Sec. 4
40	`W2Opus_EPRLHessianAndUniqueness R19`	3,583	`w2opus_r19_capstone`	Sec. 4
41	`W2Opus_EPRLReggeChainR6`	198	`wall2_eprl_regge_chain`	Sec. 4
42	`W2Opus_EPRLSpinFoamActionCritical PointR18`	1,900	`w2opus_r18_capstone`	Sec. 4
43	`W2Opus_EPRLStationaryPhase AsymptoticsR21`	5,001	`w2opus_r21_capstone`	Sec. 4
44	`W2Opus_EPRLTransverseHessian DeterminantR20`	1,951	`w2opus_r20_capstone`	Sec. 4
45	`W2Opus_GlobalHaarAndBinaryLedger VectorGeometryR26`	3,720	`w2opus_r26_capstone`	Sec. 4
46	`W2Opus_GluedTwoSimplexLorentzian SaddleR15B`	784	`w2opus_r15b_capstone`	Sec. 4
47	`W2Opus_InteriorEdgeBulkRegge EquationsR10`	1,245	`w2opus_r10_capstone`	Sec. 4
48	`W2Opus_InteriorHingeBulkGluing OrientationLockR24`	1,083	`w2opus_r24_capstone`	Sec. 4
49	`W2Opus_LorentzianEPRLSimplicity Coherent4SimplexR1`	944	`w2opus_r1_capstone`	Sec. 4
50	`W2Opus_LorentzianSchlafliReggeR3`	383	`w2opus_r3_capstone`	Sec. 4
51	`W2Opus_MorseLemmaAndReggeCritical PointR12`	1,276	`w2opus_r12_capstone`	Sec. 4

Continued on next page

Table A2 *(continued from previous page)*

#	Audited Lean 4 Module	Lines	Primary Capstone / Key Declaration	Section
52	W2Opus_MultiDimMorseStationaryPhaseR11	1,149	w2opus_r11_capstone	Sec. 4
53	W2Opus_NonlinearReggeStationaryPhaseR14	1,029	w2opus_r14_capstone	Sec. 4
54	W2Opus_ParityConjugateReggeCosineR23	3,002	w2opus_r23_capstone	Sec. 4
55	W2Opus_PrincipalSeriesEPRLR4	765	w2opus_r4_capstone	Sec. 4
56	W2Opus_PrincipalSeriesUnitaryR7	495	ps_unitary	Sec. 4
57	W2Opus_QuantRadiusGluedEPRLMixedSpinR29	795	w2opus_r29_capstone	Sec. 4
58	W2Opus_ReggeOffSaddleLocalizationR14B	585	w2opus_r14b_capstone	Sec. 4
59	W2Opus_ReggeStationaryPhaseR2	718	w2opus_r2_capstone	Sec. 4
60	W2Opus_StationaryPhase4SimplexAsymptoticsR9	508	w2opus_r9_capstone	Sec. 4
61	W2Opus_TwoLengthBulkHessianAnd2DStationaryPhaseR28	3,959	w2opus_r28_capstone	Sec. 4
62	W2Opus_TwoSimplexLorentzianEPRLGluingR22	651	w2opus_r22_capstone	Sec. 4
63	W3Neon_DynamicalRotatingChargedRSBounceCollapseVaidyaAndLedgerCoarseGrainingR14	13,462	dynamical_rotating_charged_rs_bounce_collapse_vaidya_and_ledger_coarse_graining_master	Sec. 5
64	W3Neon_RegularRotatingRSBounceAndUnconditionalWittenCollapseR12	10,407	regular_rotating_rs_bounce_and_unconditional_witten_collapse_r12_capstone	Sec. 5
65	W3Neon_Seam5ADynamicalRSCollapseBounceAndWittenMassR13	4,503	seam5a_dynamical_rs_collapse_bounce_and_witten_mass_r13_capstone	Sec. 5
66	W3Opus_ChargedVaidyaEinsteinMaxwellNullDustR22	172	cv_charged_vaidya_capstone	Sec. 5
67	W3Opus_ChargedVaidyaEinsteinMaxwellNullDustR22A	5,877	cv_regular_point_exists	Sec. 5
68	W3Opus_ChargedVaidyaEinsteinMaxwellNullDustR22B	4,576	cv_nonvacuous	Sec. 5
69	W3Opus_ChargedVaidyaEinsteinMaxwellNullDustR22C	6,645	cv_kretschmann_psi2	Sec. 5
70	W3Opus_ChargedVaidyaEinsteinMaxwellNullDustR22D	1,410	cv_witness	Sec. 5
71	W3Opus_GeneralBounceGeodesicsAndArealLawVariationalR28	44	rr28_round12_capstone	Sec. 5
72	W3Opus_GeneralBounceGeodesicsAndArealLawVariationalR28A	649	rgp_capstone	Sec. 5
73	W3Opus_GeneralBounceGeodesicsAndArealLawVariationalR28B	875	rgo_capstone	Sec. 5
74	W3Opus_GeneralBounceGeodesicsAndArealLawVariationalR28C	1,588	rax_capstone	Sec. 5
75	W3Opus_GeneralBounceGeodesicsAndArealLawVariationalR28D	1,003	rlaw_capstone	Sec. 5
76	W3Opus_GeneralBounceGeodesicsAndArealLawVariationalR28E	523	rgu_capstone	Sec. 5

Continued on next page

Table A2 *(continued from previous page)*

#	Audited Lean 4 Module	Lines	Primary Capstone / Key Declaration	Section
77	W3Opus_GlobalChartGluingKruskal BlockAndRotatingSourceR30	552	rr30_round14_capstone	Sec. 5
78	W3Opus_GlobalChartGluingKruskal BlockAndRotatingSourceR30A	1,307	rtd_capstone	Sec. 5
79	W3Opus_GlobalChartGluingKruskal BlockAndRotatingSourceR30B	1,064	rcc_capstone	Sec. 5
80	W3Opus_GlobalChartGluingKruskal BlockAndRotatingSourceR30C	2,081	rst_capstone	Sec. 5
81	W3Opus_GlobalChartGluingKruskal BlockAndRotatingSourceR30D	1,713	rkb_capstone	Sec. 5
82	W3Opus_GlobalMultiHorizonKruskal AndSmoothTetradR31A	185	r31a_capstone	Sec. 5
83	W3Opus_GlobalMultiHorizonKruskal AndSmoothTetradR31B	275	r31b_capstone	Sec. 5
84	W3Opus_GlobalMultiHorizonKruskal AndSmoothTetradR31D	149	r31d_capstone	Sec. 5
85	W3Opus_GloballySmoothRotating BounceCoreR25	182	rrbb_nec_capstone	Sec. 5
86	W3Opus_GloballySmoothRotating BounceCoreR25A	257	svKretschCF_l_zero	Sec. 5
87	W3Opus_GloballySmoothRotating BounceCoreR25B	3,302	bb_pd_chrisF	Sec. 5
88	W3Opus_GloballySmoothRotating BounceCoreR25C	2,049	bb_id_einsteinF	Sec. 5
89	W3Opus_GloballySmoothRotating BounceCoreR25D	3,457	bbT3P_eq	Sec. 5
90	W3Opus_GloballySmoothRotating BounceCoreR25E	1,256	bb_kretschmann_kerr_crosscheck	Sec. 5
91	W3Opus_GloballySmoothRotating BounceCoreR25F	643	sv_witness	Sec. 5
92	W3Opus_GloballySmoothRotating BounceCoreR25G	725	svh_phase_capstone	Sec. 5
93	W3Opus_GloballySmoothRotating BounceCoreR25H	531	svj_bridge_capstone	Sec. 5
94	W3Opus_GloballySmoothRotating BounceCoreR25I	125	sv_scalarF_reflect	Sec. 5
95	W3Opus_HorizonCrossingGeodesics UniquenessAndConformalRatioR29	51	rr29_round13_capstone	Sec. 5
96	W3Opus_HorizonCrossingGeodesics UniquenessAndConformalRatioR29A	608	rhc_capstone	Sec. 5
97	W3Opus_HorizonCrossingGeodesics UniquenessAndConformalRatioR29B	1,218	rpu_capstone	Sec. 5
98	W3Opus_HorizonCrossingGeodesics UniquenessAndConformalRatioR29C	1,067	rfr_capstone	Sec. 5
99	W3Opus_HorizonCrossingGeodesics UniquenessAndConformalRatioR29D	550	rcr_capstone	Sec. 5
100	W3Opus_KerrDeSitterExactEinstein LambdaR20	244	kds_capstone_carter	Sec. 5
101	W3Opus_KerrDeSitterExactEinstein LambdaR20A	2,326	chrisKD_eq	Sec. 5

Continued on next page

Table A2 *(continued from previous page)*

#	Audited Lean 4 Module	Lines	Primary Capstone / Key Declaration	Section
102	W3Opus_KerrDeSitterExactEinsteinLambdaR20B	2,425	kdsField_Lambda_zero	Sec. 5
103	W3Opus_KerrDeSitterExactEinsteinLambdaR20C	6,975	kds_kretschmann_equator	Sec. 5
104	W3Opus_KerrDeSitterExactEinsteinLambdaR20D	3,206	kds_kretschmann_psi2	Sec. 5
105	W3Opus_KerrDeSitterExactEinsteinLambdaR20E	1,016	kds_three_horizons_kappa	Sec. 5
106	W3Opus_KerrDeSitterExactEinsteinLambdaR20F	503	kds_three_horizons_region_witness	Sec. 5
107	W3Opus_KerrDeSitterExactEinsteinLambdaR20G	2,387	kds_hj_separates	Sec. 5
108	W3Opus_KerrDeSitterExactEinsteinLambdaR20H	207	kds_circular_carter_constant	Sec. 5
109	W3Opus_KerrNewmanDeSitterEinsteinMaxwellLambdaR21	286	knds_capstone_signature_area_charge	Sec. 5
110	W3Opus_KerrNewmanDeSitterEinsteinMaxwellLambdaR21A	2,395	chrisKQ_eq	Sec. 5
111	W3Opus_KerrNewmanDeSitterEinsteinMaxwellLambdaR21B	4,917	traceKQ_cf	Sec. 5
112	W3Opus_KerrNewmanDeSitterEinsteinMaxwellLambdaR21C	644	kndsPot_Lambda_zero	Sec. 5
113	W3Opus_KerrNewmanDeSitterEinsteinMaxwellLambdaR21D	6,998	knds_kretschmann_equator	Sec. 5
114	W3Opus_KerrNewmanDeSitterEinsteinMaxwellLambdaR21E	1,186	knds_lukewarm_witness	Sec. 5
115	W3Opus_KerrNewmanDeSitterEinsteinMaxwellLambdaR21F	317	knds_lukewarm_horizons	Sec. 5
116	W3Opus_MaximalAnalyticExtensionAndDynamicalCoreMatchingR32B	189	r32b_capstone	Sec. 5
117	W3Opus_RegularRotatingHaywardKerrR23	176	rrbh_curvature_capstone	Sec. 5
118	W3Opus_RegularRotatingHaywardKerrR23A	201	gg_const_eig	Sec. 5
119	W3Opus_RegularRotatingHaywardKerrR23B	3,560	gg_regular_point_exists	Sec. 5
120	W3Opus_RegularRotatingHaywardKerrR23C	1,712	gg_fluid_entries	Sec. 5
121	W3Opus_RegularRotatingHaywardKerrR23D	3,457	ggT3P_eq	Sec. 5
122	W3Opus_RegularRotatingHaywardKerrR23E	1,002	hke_capstone	Sec. 5
123	W3Opus_RegularRotatingHaywardKerrR23F	925	hay_horizon_capstone	Sec. 5
124	W3Opus_RegularRotatingHaywardKerrR23G	1,249	gg_kretschmann_kerr_crosscheck	Sec. 5
125	W3Opus_RegularRotatingHaywardKerrR23H	433	gg_DEC_iff	Sec. 5
126	W3Opus_RegularRotatingHaywardKerrR23I	286	gg_horizon_generator_capstone	Sec. 5

Continued on next page

Table A2 *(continued from previous page)*

#	Audited Lean 4 Module	Lines	Primary Capstone / Key Declaration	Section
127	W3Opus_RegularRotatingHaywardKerr R23J	351	hay_blackhole_point	Sec. 5
128	W3Opus_RotatingBounceAllGeodesics AndRotatingSourceR27	163	rr27_round11_capstone	Sec. 5
129	W3Opus_RotatingBounceAllGeodesics AndRotatingSourceR27A	1,392	rsrc_capstone	Sec. 5
130	W3Opus_RotatingBounceAllGeodesics AndRotatingSourceR27B	1,347	rcar_capstone	Sec. 5
131	W3Opus_RotatingBounceAllGeodesics AndRotatingSourceR27C	707	rsh_capstone	Sec. 5
132	W3Opus_RotatingBounceAllGeodesics AndRotatingSourceR27D	938	rarl_capstone	Sec. 5
133	W3Opus_RotatingBounceGeodesic KillingAndRSActionR26	162	rbgk_round10_capstone	Sec. 5
134	W3Opus_RotatingBounceGeodesic KillingAndRSActionR26A	802	rbk_killing_axis_capstone	Sec. 5
135	W3Opus_RotatingBounceGeodesic KillingAndRSActionR26B	1,118	rbgk_geodesic_capstone	Sec. 5
136	W3Opus_RotatingBounceGeodesic KillingAndRSActionR26C	889	rbgk_action_capstone	Sec. 5
137	W3Fable_AsymptoticBondiGaugeAnd RSLedgerRadiationR19	2,052	bondi_gauge_ledger_capstone	Sec. 6
138	W3Fable_BondiMapJacobianLocal DiffeomorphismR21	846	bondi_map_local_diffeo_ capstone	Sec. 6
139	W3Fable_BondiMassLossEvolutionAnd BMSMemoryLedgerR25	3,884	bondi_mass_loss_memory_ledger_ capstone	Sec. 6
140	W3Fable_BondiSachsSecondOrderMap AndMassAspectR20	2,648	bondi_second_order_capstone	Sec. 6
141	W3Fable_FarRimLedgerBitFluxSigma BridgeR23	1,039	ledger_bit_flux_sigma_bridge_ capstone	Sec. 6
142	W3Fable_GeneralTwoChartBondiNews AndNonlinearMemoryR27	5,236	two_chart_general_news_memory_ vacuum_capstone	Sec. 6
143	W3Fable_SphereGlobalSoftFlux UniquenessR22	2,468	sphere_soft_flux_capstone	Sec. 6
144	W3Fable_TwoChartGlobalBondiMass LossSupermomentumParityR26	5,139	two_chart_bondi_mass_loss_ supermomentum_parity_capstone	Sec. 6
145	W3Fable_TypeNVacuumWaveBondiCount WitnessR24	376	typeN_bondiCount_capstone	Sec. 6